UNIVERSITY OF COPENHAGEN
FACULTY OF SCIENCE

Optical Magnetometry
for Magnetic Resonance Imaging

PhD Thesis

By
Hans Stærkind

Niels Bohr Institute &
Danish Research Centre for Magnetic Resonance

Under the supervision of
Prof. Eugene S. Polzik
Assoc. Prof. Esben T. Petersen
Research Fellow Vincent O. Boer

This thesis has been submitted to the PhD School of The Faculty of Science,
University of Copenhagen

October 2023

List of Abbreviations

AR	Antireflection
DRCMR	Danish Research Centre for Magnetic Resonance
ecc	Eddy current compensation
ECDL	External cavity diode laser
EOM	Electro-optic modulator
EPI	Echo-planar imaging
EXAAQ	Extreme angular-momentum absorption-spectroscopy quantum
FID	Free induction decay
FM	Frequency modulation
HCCM	Hydrogen-constant-core-model
LPF	Low pass filter
MJF	Multi Jet Fusion
MM	Multimode
MR	Magnetic resonance
MRI	Magnetic resonance imaging
NBI	Niels Bohr Institute
NMR	Nuclear magnetic resonance
PBS	Polarizing beam splitter
PCB	Printed circuit board
PM	Polarization maintaining
ppm	Parts-per-million
PSD	Power spectral density
rf	Radio frequency
RS	Russell-Saunders
SLA	Stereolithographic
VCO	Voltage controlled oscillator

Abstract

This thesis presents a novel optical magnetometer for high magnetic fields along with the first explorations of its applications in MRI.

The magnetometer works by continuously tracking a magnetic-field-dependent optical resonance in atomic cesium. The technique employs a combination of well-established methods comprising sideband spectroscopy, saturated absorption spectroscopy, and FM spectroscopy. A large focus of this work has been on engineering a robust solution that could be operated in a hospital environment. This has resulted in a novel — but still mature — technology, with specifications that compare favorably to conventional and commercially available methods for high-field magnetometry.

In order to calibrate the magnetometer, the magnetic-field-dependence of the relevant optical cesium resonance has been characterized. NMR magnetometry on pure water has been used as the absolute reference. This has resulted in accurate measurements of two universal cesium coefficients, describing the field dependence, such that magnetometry can now be performed using this technique with an accuracy in the ppm-range.

The magnetometer has been used to map out two MRI sequences in a 7 T scanner, and to detect temporal instabilities and spatial non-linearities in the gradients. This work establishes the field of optical magnetometry for MRI, with future possibilities including image corrections in e.g. error-prone sequences or gradient coil systems with relaxed technical requirements.

Resumé

Denne afhandling præsenterer et nyt optisk magnetometer til høje magnetfelter, sammen med de første undersøgelser af dets anvendelser inden for MR billeddannelse.

Magnetometeret fungerer ved kontinuerligt at følge en magnetfeltsafhængig optisk resonans i atomar cæsium. Teknikken anvender en kombination af velkendte metoder, herunder sidebåndsspektroskopi, mættet absorptionsspektroskopi og FM spektroskopi. En stor del af dette arbejde har fokuseret på at udvikle en robust løsning, der kan anvendes i et hospitalsmiljø. Dette har resulteret i en ny, men stadig moden teknologi, med specifikationer, der ser lovende ud sammenlignet med konventionelle og kommercielt tilgængelige metoder til højfeltsmagnetometri.

For at kalibrere magnetometeret er magnetfeltafhængigheden af den relevante optiske cæsiumresonans blevet karakteriseret. NMR-magnetometri på rent vand er blevet brugt som absolut reference. Dette har resulteret i nøjagtige målinger af to universelle cæsiumkoefficienter, der beskriver feltafhængigheden, hvilket betyder, at magnetometri med denne teknik nu kan levere en nøjagtighed på få milliontedele.

Magnetometeret er blevet brugt til at kortlægge to MR-sekvenser i en 7 T scanner og til at detektere tidsmæssige ustabiliteter og rumlige ikkelineariteter i gradienterne. Dette arbejde etablerer optisk magnetometri inden for MR som et nyt forskningsfelt, med fremtidige muligheder for f.eks. billedkorrektioner i problematiske sekvenser eller gradientspolesystemer med slækkede tekniske specifikationer.

Contents

1 Introduction

1.1 Background

Around 2016 Assoc. Prof. Esben T. Petersen and Research Fellow Vincent O. Boer from DRCMR, were following the progress on magnetic-field monitoring in MRI: It had been shown that by tracking the magnetic-field gradients using NMR probes during an MRI sequence, the image quality could in some cases be improved. After testing out the commercially available Skope field-monitoring system in their 7 T MRI scanner, they decided that there were just too many technical challenges associated with the introduction of metallic probes and cables in the MRI scanner. Esben got the idea to employ optical probes instead of NMR probes, since such magnetometers could be made without metallic or electronic components, and hence be completely MRI compatible. They reached out to Prof. Eugene S. Polzik and Asst. Prof. Kasper Jensen from NBI, to hear about the possibility of using optical magnetometers in a high-field MRI scanner. Eugene and Kasper told them that optical magnetometers do not work at high fields. But this was not the end of the conversation — rather it was the beginning of an ambitious project to develop a new kind of optical magnetometer that *would* work at high fields. A project that I was fortunate enough to get to carry out.

This work has been described in two papers, which are included in this thesis, and also referred to as Refs. [1, 2]. All data and calculations supporting these papers are openly available in Refs. [3, 4]. In addition to the two papers, which describe the main results, this thesis also provides further (historical) context and describes necessary technical accomplishments.

1.2 Basics of MRI

When studying MRI, the importance of accurate magnetic field information quickly becomes clear. To motivate and introduce the work carried out during this PhD we here present a brief review of the basics of MRI, based on Refs. [5–7].

In MRI a person is placed in a high magnetic field B, typically of several teslas generated by a superconducting coil. The hydrogen nuclei, i.e. protons, in the body align to a small degree with the magnetic field. The field direction is typically called the z-direction. Using an rf transmit coil, the proton magnetic moments can be resonantly excited into the plane orthogonal to the magnetic field, i.e. the (x, y)-plane. The resonance frequency ν_{p} of the protons is given by

$$\nu_{\mathrm{p}} = \gamma_{\mathrm{p}} B, \tag{1.1}$$

where γ_{p}, the gyromagnetic ratio of protons, is about 42.58 MHz/T [7]. After excitation, the magnetic moments will precess around the magnetic field, radiating a weak rf signal, that is picked up inductively by an rf receive coil. If during excitation, a magnetic field gradient, e.g. in the z-direction, is played on top of the high magnetic field, using a (normally conductive) gradient coil, the nuclear excitation can be made to only happen in a certain slice, perpendicular to the z-direction, where the resonance condition Eq. (1.1) applies. Next, a series of gradients in the x- and y-direction is played, during the inductive rf data acquisition. The *time integral* of these gradients defines a trajectory though k-space, where the acquired rf data are placed in pixels one-by-one during the rf readout. When the desired area of k-space is covered, the data acquisition is over. In Fig. 1.1 is shown a simple illustration of this principle. Performing a 2D Fourier transform of the k-space image then creates a 2D image of the excited slice, revealing the inside anatomy of the person in the MRI scanner. A 3D image can be created by successive excitations of different slices next to each other. The particular trajectory through k-space sketched in Fig. 1.1 is that of an EPI sequence. Starting in the center, a negative x- and y-gradient takes us to the lower left corner of

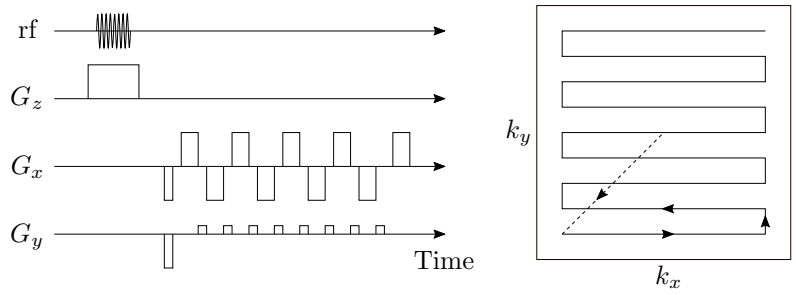

Figure 1.1: Basic principles of MRI. To the left are shown rf excitation and gradients $\{G_x, G_y, G_z\}$ on separate axes as a function of time. The rf excitation along with the G_z-gradient defines the slice selection. The time integral of gradients G_x and G_y defines the trajectory through k-space (k_x, k_y), as shown to the right. Arrows on the trajectory corresponds to the first three G_x-lobes, and the first two G_y-lobes.

the k-space area where data acquisition then starts. Strong x-gradients trace out horizontal lines, and small y-gradients take the acquisition to the next line. The acquisition is finished when the trajectory has reached the opposite corner of the k-space area.

Perfect step changes in magnetic field cannot be realized in practice, and hence practical traversals of k-space are not straight lines of constant velocity. But everything can still be made to work well, as long as the magnetic-field gradients are known. Problems *will* however occur when the gradients are not well known throughout the data acquisition. In this case errors will be introduced in the k-space image, which will give corresponding errors in the real image. This need for accurate magnetic field control has led to an impressive evolution in both MRI hardware and software, during the last couple of decades [7]. Active shielding of the gradient coils reduces eddy currents in e.g. the structure of the cryostat [8], and preemphasis of the programmed gradients is used to suppress known deviations from the desired gradient field [9, 10]. However, imperfections in MRI gradients still exist and can cause problems in the reconstruction.

1.3 Field monitoring using NMR probes

Instead of working to further perfect gradient coil systems or limit oneself to sequences that minimize eddy currents "a conceptually different approach is to allow and assess rather than suppress residual field imperfections" (from Ref. [11]). The work carried out by Prof. Klaas P. Prüssmann's research group established a new approach to dealing with field imperfections. Using NMR probes to monitor the magnetic field during rf data acquisition, they were able to directly map out the k-space trajectory, through magnetic-field measurements [11].

NMR probes work by resonant excitation of an NMR-active sample, followed by rf readout of the FID. Through Eq. (1.1) the magnetic field B can be determined from the precession frequency ν_{p}. For the highly specialized NMR probes, first introduced in Ref. [12], a lot of effort has been put into optimizing the homogeneity of the field across the active sample, by susceptibility matching of components in the probe, and by making the active sample small. This is to ensure a long lifetime of the FID signal, so that field measurements can be performed for up to about 200 ms at a time. For an NMR measurement on a magnetic field assumed to be static, or very slowly varying, one would typically measure the average frequency of the FID, to make a single magnetic field measurement per excitation. For fast field tracking in MRI, however, the phase of the FID is extracted, unwrapped and differentiated, to give the magnetic-field value at all sampling times during the measured FID [12].

The first probes that Prof. Prüssmann's group made were using hydrogen nuclei, i.e. protons, in water and cyclohexane for the NMR-active sample [12], but later they switched to fluorine nuclei in hexafluorobenzene, to avoid interference with the MRI scanner [13]. The gyromagnetic ratio of fluorine is different by about 6% of that of protons, i.e. 40.05 MHz/T [14], so the probes and the MRI scanner operate at sufficiently different frequencies that rf crosstalk is not a problem.

This line of research resulted in the establishment of the company *Skope Magnetic Resonance Technologies* in 2011, which has commercialized NMR probes for use in MRI. Skope was acquired by *Canon Medical*

Systems Corporation in 2019 [15].

Prof. Prüssmann's group does MRI research, so using NMR probes was an easy choice for them, since the fundamental principles of such probes and MRI scanners are the same. Also, other technologies for measuring high fields did not seem like good candidates, having too low sensitivity, as discussed in Ref. [12].

Making the acquisition more robust, providing a direct way of mitigating encoding errors of all origins, and clearly demonstrating improved image quality [11, 16–18], NMR probes have proved very interesting for the future of MRI. However, while interference between the probes and the MRI scanner has been somewhat mitigated by using a different nuclear species, NMR probes still suffer from some inconvenient drawbacks: Cables and probes in the scanner can still cause problems, even when carrying signals at a different frequency from what is used in the scanner [18]. The measurements are pulsed rather than continuous, so careful planning of the measurement pulses relative to the MRI sequence is needed. And shortened FIDs, i.e. reduced measurement times, due to strong gradients in the sequence must be accounted for in the planning.

Because of these limitations of NMR probes, and the lack of existing alternative methods, it seems worthwhile to investigate a completely new optical magnetometry technique for use in MRI.

1.4 High-field optical alkali magnetometry

The discovery of the splitting of the sodium D lines in a magnetic field by Nobel laureate Prof. Pieter Zeeman, in 1897, was an important breakthrough in the development of modern atomic physics and quantum mechanics [19, 20]. Even earlier, in 1870, such splittings were observed in sunspots. With Zeeman's discovery, this contributed to the understanding of magnetic fields on the sun [21]. So, the idea of using the Zeeman shift of optical absorption lines in alkali atoms to detect or measure magnetic fields, is more than 100 years old.

The Zeeman effect in alkali atoms has, since its discovery, been in-

vestigated and explained extensively through modern quantum mechanics [20, 22–24]. However, the idea of directly measuring a magnetic field through a shift in the absorption lines, has actually not been explored much beyond sunspot magnetometry. Prior to the work presented here, was only a few endeavours. In Refs. [25–28] measurements are performed on pulsed fields up to 500 T. Highly sensitive measurements were not a goal in any of these experiments. Rather, the goal was to do remote detection, on very short timescales, near explosions or high-energy-density plasmas. These methods use detection of free-space emitted light and does not involve an actual magnetic-field probe. Measurement accuracies are about 1 T. In Refs. [29–31] actual magnetic-field sensors are constructed, and tested up to 1.5 T. Effort is here put into modelling of the atomic spectra, and good agreements with experimental results are found. Measurement accuracies of about 1 mT are achieved, and the method of Refs. [29, 31] also allows for the calculation of the magnetic-field direction. Fast measurements are not a concern. In Refs. [32, 33] a fiber-coupled optical probe was constructed, and tested up to 58 T, but rather than providing a dynamic optical field measurement, it provided information about *when* a pulsed field reached a certain value. Theoretical considerations in Ref. [33] suggest that an accuracy in the ppm-range could be reached, and also the need for a better determination of the excited state g-factor is pointed out. An attempt at verifying the presence of the diamagnetic shift is unsuccessful in Ref. [33].

On this background there was ample room for exploring and improving on the concept of measuring magnetic fields using frequency shifts of alkali D lines. None of the explored approaches are anywhere near the specifications required for applications in MRI. These include: several fiber-coupled probes, dynamic measurement, high sampling rate, and an accuracy in the ppm-range.

1.5 Introducing the EXAAQ magnetometer

With a clearly defined application in mind, access to the incredibly advanced magnetic-field generating system of a 7 T MRI scanner, and a sizeable budget for equipment, we have managed to significantly advance this field: We have determined the excited state g-factor for the cesium D_2 line with an accuracy more than two orders of magnitude better than previously. We have managed to clearly verify the presence of the diamagnetic shift of the D_2 line and measure it with an accuracy better than 1%. We have constructed a highly robust and compact magnetometer system with four fiber-coupled probes, sampling rate of tens of kilohertz, and a measurement accuracy of a few ppm. Finally, we have used this magnetometer to perform measurements in a 7 T MRI scanner playing imaging sequences and shown that the device is sensitive enough to detect imperfections in the gradient coil system.

The work is presented in two scientific papers. The first, Ref. [1], "Precision Measurement of the Excited State Landé g-factor and Diamagnetic Shift of the Cesium D_2 Line", describes the fundamental physics. I.e., that the frequency shift $\Delta\nu_+$, of the cesium D_2 transition between the extreme angular-momentum states depends on the magnetic field B, as

$$\Delta\nu_+ = \gamma_1 B + \gamma_2 B^2, \tag{1.2}$$

where $\gamma_1 = 13.994\,301(11)$ GHz/T and $\gamma_2 = 0.4644(35)$ MHz/T^2.

The second paper, Ref. [2], "High-Field Optical Cesium Magnetometer for Magnetic Resonance Imaging", presents the complete magnetometer system. The performance is benchmarked, measurements of two MRI sequences are shown, and the ability to clearly resolve imperfections in the coil system is demonstrated. The term EXAAQ (EXtreme Angular-momentum Absorption-spectroscopy Quantum) magnetometry is proposed to describe the technology, and clearly distinguish it from high-field magnetometers based on magneto-optical Faraday rotation, and low-field optically pumped magnetometers also based on alkali atoms.

The EXAAQ magnetometer prototype has four probes, which realizes saturated absorption spectroscopy inside the 7 T MRI scanner, and one reference probe which realizes saturated absorption spectroscopy in a magnetic shield, i.e. at 0 T. The frequency shift between the extreme transition at 0 T and at 7 T is determined by sideband spectroscopy, and the magnetic field is calculated through Eq. (1.2). This is the basic idea of the technique.

In the following we will first review the energy-level structure of cesium, and show how the spectrum can be calculated, from low to high field. This constitutes the scientific background and provides some technical details on calculations. Next, we go through the optical probe design, and show how we generate strong sidebands of high order, with modulation frequencies up to 20 GHz. These two important technical accomplishments are followed by the two papers [1, 2]. We then show how the modular 19-inch rack integration of the prototype has been realized, and a short chapter discusses the use of the magnetometer for fields below 1 T. The thesis is concluded by summarizing the main results and discussing future opportunities and challenges.

2 Energy Levels of Cesium (and Protons)

Comparing Eq. (1.1) and Eq. (1.2) we see some resemblance between proton NMR magnetometry and EXAAQ magnetometry. Indeed, both are quantum sensing methods, that make use of the Zeeman shift of energy levels when quantum systems are exposed to a magnetic field. The main difference between the methods is that in NMR the *resonance frequency* depends on the magnetic field, whereas in EXAAQ magnetometry it is the *resonance frequency shift* that depends on the magnetic field. This means that NMR operates at rf frequencies — typically tens or hundreds of megahertz — whereas EXAAQ operates at optical frequencies — hundreds of terahertz. The energies of the two spin states of a proton in a magnetic field, as relevant for NMR, are shown in Fig. 2.1. This

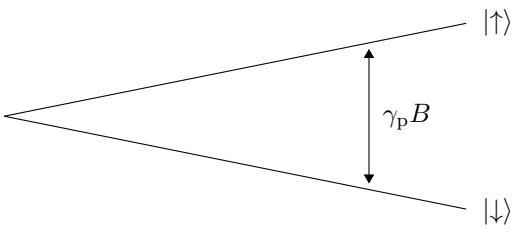

Figure 2.1: The energy splitting of the spin-up and spin-down states of a proton in a magnetic field B. The difference is expressed in units of frequency.

is a very simple energy-level diagram compared to the relevant equivalent for the cesium atom, which is shown in Fig. 2.2, for the case of a low magnetic field. To introduce the physics, we briefly review the

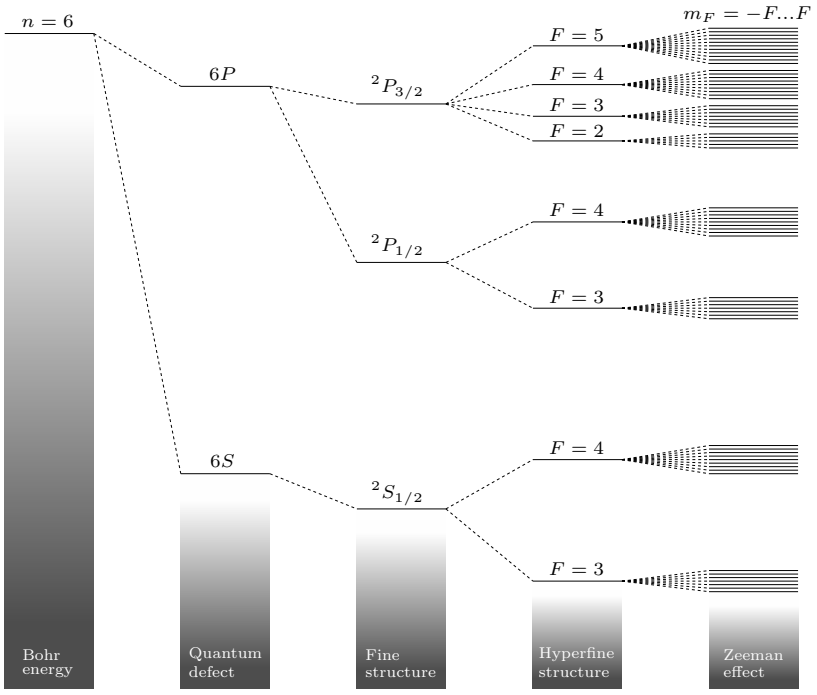

Figure 2.2: The various mechanisms responsible for the energy level structure of cesium at low magnetic fields. The contributions range from the strongest effects on the left, to the weakest effects on the right.

mechanisms behind this structure [20, 34]. The single valence electron in cesium-133 has the principal quantum number $n = 6$, which gives an equivalent *Bohr energy*. The electron can be in the ground state, with orbital angular-momentum quantum number $L = 0$, called the S state, or in the excited state, with an angular-momentum quantum number of $L = 1$, called the P state. In a non-relativistic model of a hydrogen-like atom these two states will be degenerate. However, in the case of an alkali atom, which has an inner core of electrons, the different spatial distributions of the S- and the P-state wavefunctions lead to different nuclear-charge screenings, and hence vastly different energies for the two states. This is commonly described by a reduced effective principal quantum number $n^* = n - \delta_L$, where δ_L is called the *quantum defect*. The relativistic *fine structure* perturbs and splits these energies

— most importantly the magnetic moment associated with the electron orbital angular momentum L, interacts with the magnetic moment associated with the electron spin $S = 1/2$. When they align to give a total electronic angular momentum $J = L + S = 3/2$, the energy is increased, and when they are opposite, $J = L - S = 1/2$, the energy is decreased. This gives two different excited states. The fine-structure states are label in "spectroscopic notation" as ${}^{2S+1}L_J$ [20]. The transition between the ground state ${}^2S_{1/2}$, and the least energetic excited state ${}^2P_{1/2}$, is called the D_1 line and has a wavelength of 894 nm. The transition between the ground state and the most energetic excited state ${}^2P_{3/2}$, is called the D_2 line and has a wavelength of 852 nm [34]. These two lines, and associated energy levels furthermore contains splittings known as the *hyperfine structure*: The nuclear magnetic moment, due to the nuclear spin $I = 7/2$, interacts with the magnetic moment of the electron. This gives states with different total angular momentum F, and similarly different energies. The states with different projected total angular-momentum quantum number m_F are degenerate. When exposed to a low magnetic field the m_F states are perturbed and split up to have different energies. This is the *Zeeman effect*.

The case of a low magnetic field is typically called the *Zeeman regime*. When the Zeeman splitting becomes larger than the hyperfine splitting, it is no longer valid to treat the Zeeman effect as a perturbation to the hyperfine structure. Instead, the hyperfine structure acts as a perturbation to the Zeeman levels, as shown in Fig. 2.3. This is called the *hyperfine Paschen-Back regime*. The Zeeman effect splits up the energy according to the electronic projected angular-momentum quantum number m_J, and the hyperfine interaction further splits up the states into different energies according to their nuclear projected angular-momentum quantum number m_I. For magnetic fields of several thousands of teslas, the Zeeman effect even becomes larger than the fine structure, introducing what is called the *fine Paschen-Back regime*. Fields of thousands of teslas cannot be created in stable forms with current magnet technology.

In Ref. [1] it is shown that the physical constant describing the magni-

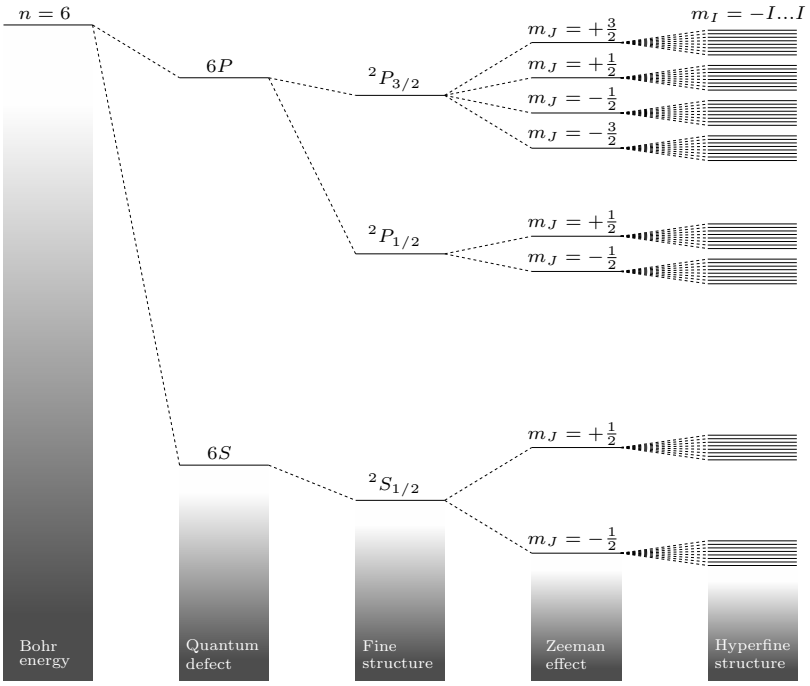

Figure 2.3: The various mechanisms responsible for the energy level structure of cesium at high magnetic fields. Notice how the hyperfine splitting is now considered a perturbation to the Zeeman effect, instead of the other way around as in Fig. 2.2.

tude of the magnetic-field dependence of the valence electron is the Bohr magneton, divided by the Planck constant, $\mu_B/h \approx 14\,\mathrm{GHz/T}$. This is similar for the magnetic-field dependence of a free electron spin-state. It is interesting to compare this number to the magnetic-field dependence of the proton spin-state $\gamma_p/2 = 21.29\,\mathrm{MHz/T}$. For a point-like proton we would expect the ratio between these two numbers to be equal to the proton-to-electron mass ratio, i.e. about 1836. The fact that the ratio is about 2.8 times lower than this, was historically the first evidence of an inner structure of the proton [20].

To find the field dependence of the energy levels in arbitrary magnetic fields, ranging from the Zeeman regime to the hyperfine Paschen-Back regime, we must numerically diagonalize the total Hamiltonian. The

Hamiltonian for the hyperfine structure is

$$H_{\mathrm{HFS}} = \frac{1}{2} A \left(F(F+1) - I(I+1) - J(J+1) \right), \tag{2.1}$$

where A is the hyperfine coupling constant [34]. The matrix elements of this Hamiltonian, in the $|F, m_F\rangle$ basis, are

$$H^{ij}_{\mathrm{HFS}} = \langle F^i, m^i_F | H_{\mathrm{HFS}} | F^j, m^j_F \rangle. \tag{2.2}$$

This Hamiltonian is diagonal, since the $|F, m_F\rangle$ states are eigenstates of the F, I, and J operators. The Hamiltonian for the Zeeman interaction is

$$H_{\mathrm{Z}} = g_J m_J \mu_{\mathrm{B}} B, \tag{2.3}$$

when the small nuclear Zeeman interaction is ignored. Here, g_J is the Landé g-factor. The matrix elements of this Hamiltonian are

$$H^{ij}_{\mathrm{Z}} = \langle F^i, m^i_F | H_{\mathrm{Z}} | F^j, m^j_F \rangle. \tag{2.4}$$

This Hamiltonian is *not* diagonal, since the $|F, m_F\rangle$ states are *not* eigenstates of the m_J operator. The $|F, m_F\rangle$ states can be expanded in the $|m_J, m_I\rangle$ states as

$$|F, m_F\rangle = \sum_{m_J, m_I} \langle m_J, m_I | F, m_F \rangle | m_J, m_I \rangle, \tag{2.5}$$

where the factors $\langle m_J, m_I | F, m_F \rangle$ are the Clebsch–Gordan coefficients [24]. Now the matrix elements can be calculated in the $|F, m_F\rangle$ basis as

$$H^{ij}_{\mathrm{Z}} = g_J \mu_{\mathrm{B}} B \sum_{m_J, m_I} m_J \langle F^i, m^i_F | m_J, m_I \rangle \langle m_J, m_I | F^j, m^j_F \rangle, \tag{2.6}$$

where we have used that $\langle m_J, m_I | m_J | m_J, m_I \rangle = m_J$ [1, 20, 34].

The total matrix with elements $H^{ij}_{\mathrm{HFS}} + H^{ij}_{\mathrm{Z}}$ is then calculated for a given magnetic field B and diagonalized numerically in Matlab, to give the possible eigenenergies. Doing this for a series of magnetic-field values gives a magnetic-field-depended spectrum of energies as seen in Fig. 2.4, for the ground state. There is no guaranteed order in the returned eigenenergies that Matlab produces, as is seen here. To link the energies

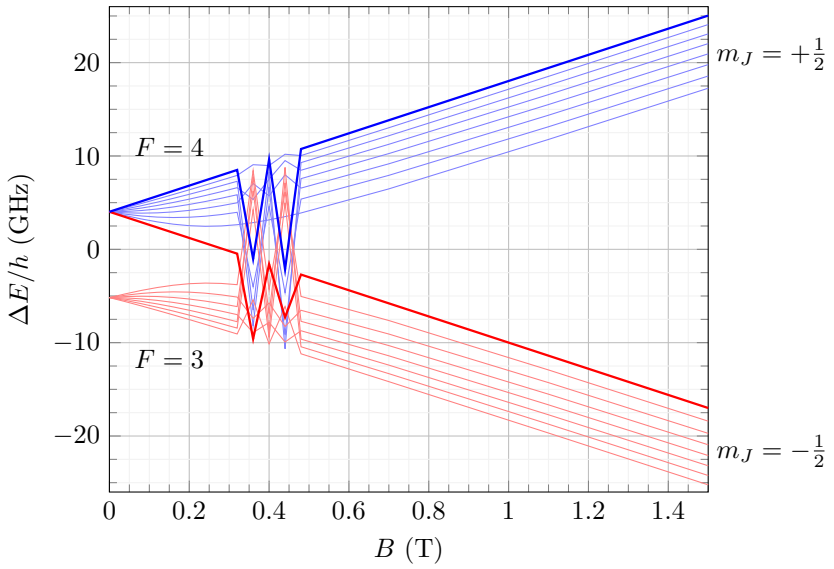

Figure 2.4: Eigenenergies of the $^2S_{1/2}$ ground state, as they are returned by Matlab, prior to sorting.

at different magnetic field values, so that meaningful interpolations can be performed, a descending sorting of the energies can be employed, prior to plotting, to arrive at Fig. 1(a) in Ref. [1] (page 56 in this thesis).

For the $^2P_{3/2}$ excited state, where lines are crossing each other, sorting is not enough, as seen in Fig. 2.5. To fix this, an algorithm has been developed that swaps the order of the eigenenergies, for each magnetic field value, to minimize the second derivative of the lines. The effect of employing this algorithm is seen in Fig. 2.6. The Matlab script that calculates the eigenenergies of the excited state, and properly connects the lines, is available in Ref. [3]. The corrected version of Fig. 2.5 is presented as Fig. 1(b) in Ref. [1] (page 56 in this thesis), along with the derivation of Eq. (1.2).

For the ground state an analytical solution for the intermediate regime also exists — the Breit-Rabi formula [34]. For the excited state no analytical solution exists, and a numerical diagonalization is necessary, leaving the problem of connecting the energies unavoidable. With all the energies connected properly, the allowed transitions in the Paschen-Back

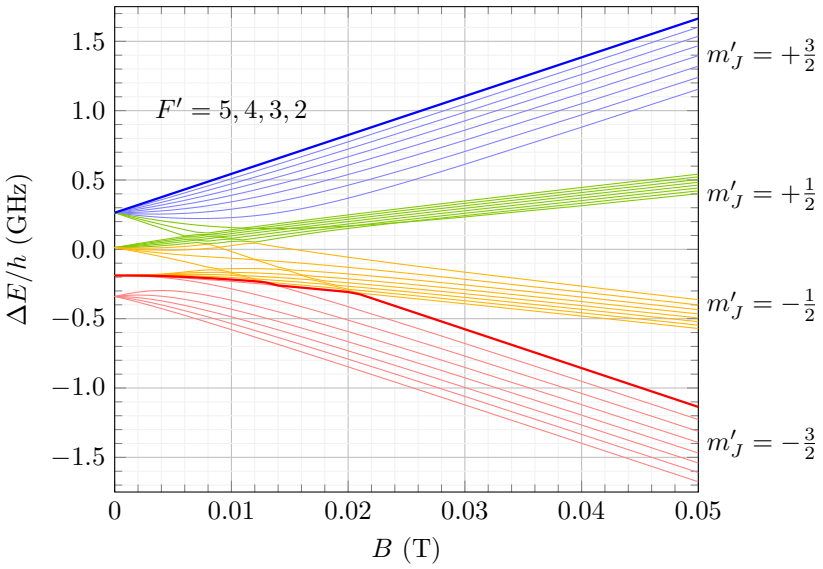

Figure 2.5: Eigenenergies of the $^2P_{3/2}$ excited state, sorted in a descending order prior to plotting. This sorting prohibits line crossings, and hence does not connect the energies correctly.

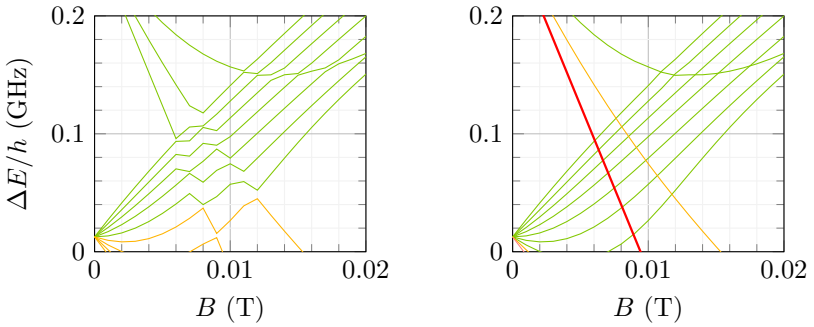

Figure 2.6: To the left are shown the eigenenergies sorted in a descending order prior to plotting. To the right are shown the eigenenergies after running the algorithm that minimizes the second derivative.

regime, and their extensions into the Zeeman regime, can be calculated. The verification of the calculated pattern is shown as Fig. 18 in Ref. [1] (page 70 in this thesis). While not strictly necessary for the main results of Ref. [1], this verification is a result in its own right. It is the most comprehensive investigation ever made for cesium. Ranging from 0–

1.5 T in steps of 0.1 T, it fully resolves the transition from the Zeeman regime to the hyperfine Paschen-Back regime.

Measured values for hyperfine coupling constants and g-factors determine the splittings and magnetic-field dependencies of states [23, 34]. The excited state g-factor, which is of particular interest to this work was last measured by Abele et al. in 1975 by an optical double-resonance experiment [35]. This was partly motivated by the need for a better g-factor determination to interpret results from level-crossing experiments, used to determine hyperfine coupling constants [22, 35, 36]. While determinations of hyperfine coupling constants are an ongoing field of research [37], not much has happened in g-factor measurements since the 70s, perhaps in part due to the fact that level-crossing experiments are no longer a preferred method for measuring hyperfine coupling constants [37].

3 Development of MRI-Compatible Probes

The development of an array of MRI-compatible fiber-coupled probes with all the optics necessary for performing saturated absorption spectroscopy [20,38], has been a major milestone in this work. In the following we discuss the thoughts going into the design, describe the process of assembly, show how the optical heating works, discuss optimal temperature and probe power, and finally look into the determination of the magnetic susceptibilities of the probe components.

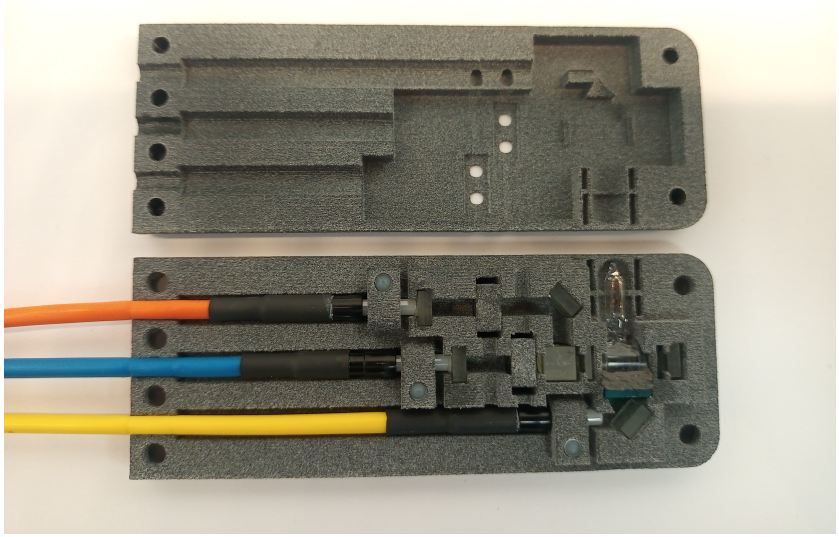

Figure 3.1: Picture of a probe. The cover is removed to show the optics inside.

3.1 Optical design

The optics inside the probe is shown as Figs. 3 and 11 in Ref. [1] (pages 58 and 64 in this thesis). A picture of the opened probe is shown in Fig. 3.1. The probe is realized as a small $90 \times 33 \times 10\text{mm}^3$ nylon assembly: a holder with clamps for the ceramic fiber ferrules and slots for the optics, and a protective cover that fits on top of it. Nine M3 nylon bolts are used: three for the fiber-ferrule clamps, and six for assembling the holder and the cover. In the following we go through the different optical elements.

The probing laser beam enters through the blue PM fiber. The fiber is pushed against a transparent window with index-matching gel between the fiber and the window. The side of the window facing away from the fiber is AR coated. This reduces reflections from the fiber surface which cause cavity fringes in the spectrum. Probe transmissions, with and without index-matching gel, are shown in Fig. 3.2. The window also

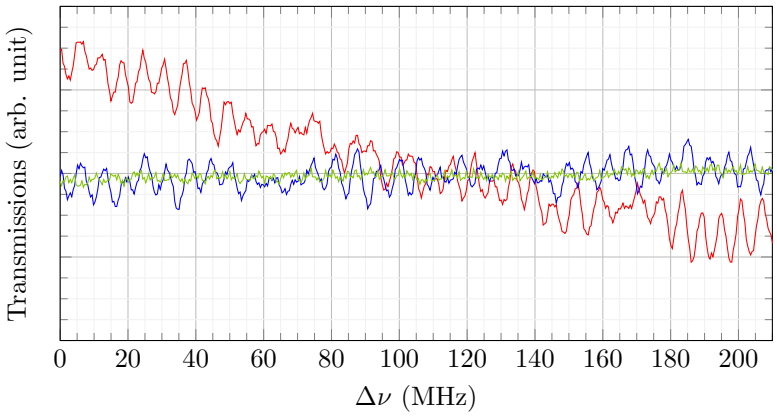

Figure 3.2: Probe transmission without index-matching gel (red), with index-matching gel on the output fiber (blue), and with index-matching gel on both input and output fiber (green). The measurement with gel on both fibers shows a clear reduction in cavity fringes. When no index-matching gel is applied, a fringe with a free spectral range of much more than 200 MHz is also visible. This is probably due to a cavity formed between the two fiber endfaces. Calibration of the laser frequency scan is done by a prior scan of the hyperfine structure.

serves the purpose of clearly marking where the fiber endface should be positioned, relative to the collimating lens. The laser beam expands from the fiber aperture with an angle measured to be $\theta = 0.086$ radians. Theoretically the angle should be

$$\theta = \frac{\lambda}{\pi w_0}, \tag{3.1}$$

where $w_0 = 2.65 \pm 0.5$ µm is the beam waist inside the fiber (the datasheet specifies this at $\lambda = 850$ nm) [39]. From this we expect the beam divergence angle to be in the range from 0.086 to 0.126 radians. This is only just in agreement with the measurement.

The beam is collimated by a lens with focal length $f = 10$ mm. This gives a collimated beam waist of

$$\begin{aligned} w_c &= f \cdot \tan\theta \\ &= 0.86 \text{ mm}. \end{aligned} \tag{3.2}$$

Next, the beam is transmitted through a PBS. A maximum transmission of 90% is measured, consistent with the datasheet specification of $T_\mathrm{P} > 90\%$. After passing through the PBS, a high-quality linear polarization is achieved. According to the PBS datasheet the transmission extinction ratio is $T_\mathrm{P}/T_\mathrm{S} > 1000 : 1$.

The beam is then passed through a quarter-wave plate, changing the polarization from linear to circular. This is a zero-order quarter-wave plate, making it fairly insensitive to temperature changes.

Next, the circularly polarized beam passes through the vapor cell. The beam here serves the purpose of pump beam, saturating the atomic transition to a high degree for the resonant velocity class of the thermal distribution.

After passing the cell, the beam is clipped by an aperture of diameter $d = 2$ mm. The aperture is built into the 3D printed nylon structure. The transmission through the aperture is given by $1 - e^{-d^2/2w_c^2} = 93\%$ [39].

After this, the beam passes through an optical filter with a transmission of 40%, hits a mirror with a 98% reflectance, and is passed through

the filter again. The beam now travels back through the cell, this time acting as a weak probe beam, sensitive to the holes burnt in the velocity distribution by the counterpropagating pump beam. The aperture ensures a good overlap between the pump and probe beam, as well as removing the low intensity part of the beam, which would not cause any saturation, hence not contributing any signal.

When the beam passes the quarter-wave plate for the second time, the circular polarization is changed back into linear polarization, rotated 90° compared to the initial linear polarization. It is then reflected off the PBS, which is specified to have a reflectance $R_S > 99.5\%$.

The beam is finally reflected by a mirror with reflectance of 98%, and focused by another lens, with $f = 10$ mm, into a MM fiber, also connected to an AR coated window with index-matching gel. The MM fiber has a core diameter of 0.4 mm, making it possible to couple into it with a high efficiency.

Surfaces on lenses, PBS, wave plate, and filter are all AR coated and have reflectance less than 0.3%. The vapor cell AR coating is a little worse, having a transmission (off-resonant) of about 98%, for all four surfaces combined. The transmissions for the most significant components are summarized in Tab. 3.1, with the accumulated transmission

Component	Transmission (%)	Total (%)
PBS	90	90
Cell	98	88
Aperture	93	82
Filter	40	33
Mirror	98	32
Filter (2^{nd} pass)	40	13
Cell (2^{nd} pass)	98	12
Mirror	98	12

Table 3.1: Transmission through the optics of the probes. The transmissions through the individual components are listed in the second column, and the accumulated transmissions of the components are listed in the third column.

tabulated as well. We see that a total transmission of about 12% corresponds to optimal output-fiber coupling.

In order to increase the atomic density, and hence the signal, the cell must be heated. An 808 nm heating laser enters through the yellow MM fiber, with 0.4 mm core diameter. It is reflected off a mirror, with a reflectance of 98%, and absorbed in a 98.8% absorbing filter. The filter is in good thermal contact with the cell though a heat-conductive paste, such that the optical power deposited as heat in the filter is transferred to the cell. The filling stem of the cell is pointing away from the point of heating, such that the coldest spot in the cell is the bottom of the stem. Over time the solid or liquid cesium will all gather in this point by evaporation and condensation, hence keeping the cell windows clean, such that transmission is maximized. The cell slot is made such that the holder has as little physical contact with the cell as possible, and insulating holes are made around the cell stem, to keep the cell as warm as possible.

3.2 Assembling the probes

The nylon assembly is 3D printed in PA12 nylon on a HP MJF printer. This technology was chosen for the following reasons:

- Reasonable tolerances of ± 0.2 mm, showing fairly reproducible results. This is clearly not good compared to machined parts. However, short delivery times and practically no design limitations, made the development fast and agile.
- A good M3 thread can be cut into the structure, with a tap. The interior of the structure is completely free from air.
- Optics can be glued into the slots with epoxy.
- Ability to withstand heat without releasing toxic fumes or catching fire. Even when exposed to fire, it does not continue to burn on its own.

- The material is black all through the structure, meaning that non-absorbed heating laser light will not escape as an eye hazard.

When ordering 3D prints it was requested that parts were printed at the same 45° angle, each time on the same printer, and post-processed in the same way. The probe design was developed through iterations of 23 different versions, using different printing technologies, materials, and service providers. In parallel with the last iterations an optimal procedure for assembling the probes was developed:

1. After receipt of the 3D printed parts, it is verified that all optical elements fit into the slots of the 3D print. Lens-to-windows distance and lens-holder-slot widths are measured with a caliper and noted.

2. The parts are prepared by clearing the thread holes with a 2.5 mm drill, after which 3 mm threads are cut. Three nylon bolts are screwed into the fiber-ferrule clamps. Clamp holes for fiber ferrules are cleared with a long 2.5 mm drill and the aperture is cleared with a long 2.0 mm drill. Nylon dust is blown away with compressed air.

3. All three fibers are mounted with clamps, and fibers are collected with 14 pieces of heat shrink, one for every meter, starting about 10 cm from the probe. The heating fiber and output fiber are removed again, and their ferrules are covered with caps.

4. The holder for the input-collimating lens is sanded down equally on both sides. When it is about 0.08 mm bigger than the corresponding lens-holder slot a tight fit is achieved.

5. The input-collimating lens is glued into the holder. The input-fiber window is glued into its slot, and the input fiber is pushed against it while the epoxy hardens.

6. The probe laser is turned on, and the input-collimating lens is adjusted roughly to align the beam with the groove. Pushing with a tweezer is sufficient.

7. The wave plate is inserted, without epoxy. A small hole from the bottom can be used to push it out again, if it needs to be rotated. Then the PBS and the mirror behind the vapor cell are glued into their slots. Pushing with a toothpick during hardening, it is ensured that the beam is reflected from the PBS well aligned with the groove. This step is shown in Fig. 3.3.

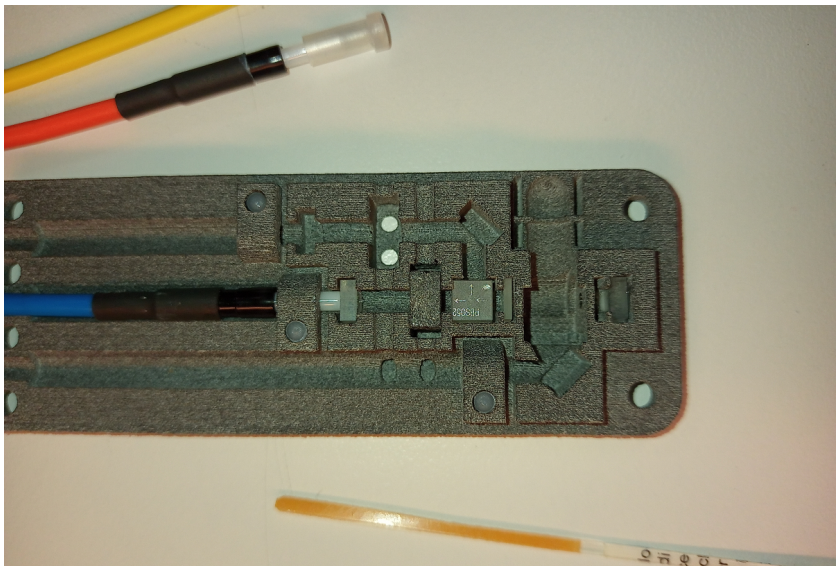

Figure 3.3: Probe assembly step 7. The input window, input-collimating lens, PBS, wave plate, and one mirror is in place. The thin infrared laser viewing card is used during beam alignment.

8. The two 45° mirrors are glued into their slots. Again, pushing with a toothpick, it is ensured that the probe beam is nicely aligned with the groove — the heating-laser beam-path alignment is not so important.

9. The output-focusing lens holder is sanded down equally on both sides like the first lens holder. If the beam collimation is poor, or the output lens-to-window distance (measured in step 1) is significantly off compared to the design, an asymmetric sanding can be used to compensate, according to a ray-tracing calculation [39].

10. The output fiber and heating fiber are inserted. The output-focusing lens is glued into the holder. The output-fiber window is glued into its slot, and the output fiber is pushed against it while the epoxy hardens. This step is shown in Fig. 3.4.

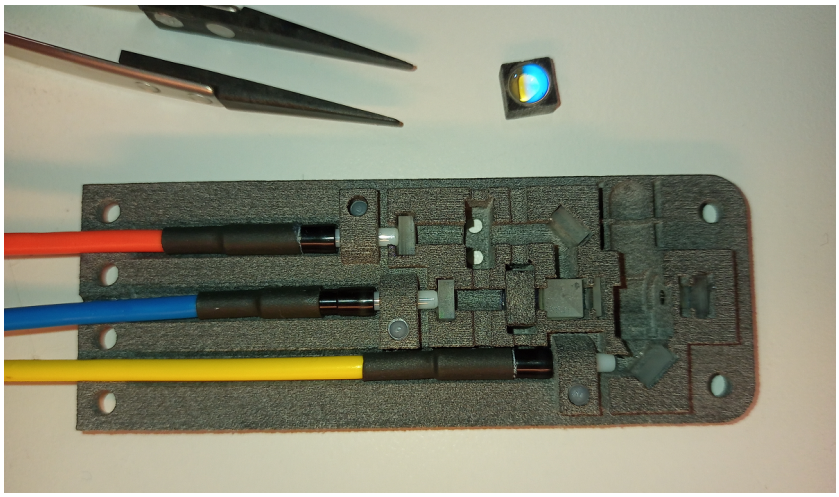

Figure 3.4: Probe assembly step 10. All beam-steering optical elements, except for the output-focusing lens, are in place.

11. The vapor cell is inserted, without epoxy. A little heat-conductive paste is applied near the bottom of the cell. The heating filter is inserted, without epoxy. More heat-conductive paste is applied between the filter and the cell.

12. The cover is fastened with six M3 nylon bolts from below. With four of the bolts near the fibers, this provides a solid strain relief for the fibers, such that the fragile non-metallic fiber connectors are not damaged during probe handling.

13. The output-focusing lens is adjusted for maximum transmission, using a specialized tool developed for this, shown in Fig. 3.5.

14. Index-matching gel is applied between the fiber endfaces and the windows. The laser frequency is scanned while rotating the input fiber. Polarization of the input light should be horizontal for

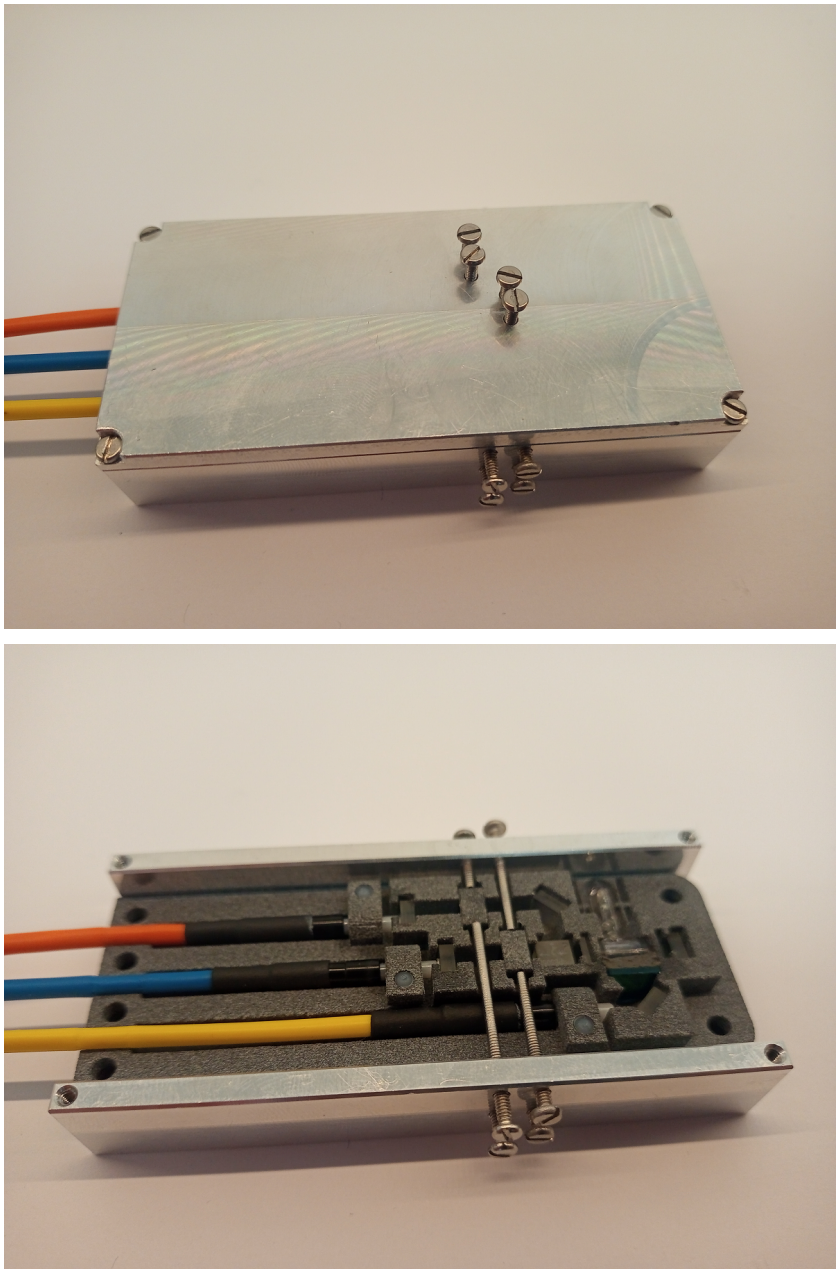

Figure 3.5: Tool for alignment of lenses. In the upper photo is shown the tool during use. In the lower photo is shown the tool without the top, and the probe without cover, for illustrative purpose.

optimal PBS transmission. Large deviations will give very little transmission. Small deviations will give a frequency (and temperature) dependent transmission, likely due to imperfect polarization transmission in the PM fiber. By scanning the frequency while rotating, optimal alignment can be found by reducing the frequency dependent oscillations. Finally, the probe filter between the cell and the mirror is inserted.

Measurements of output powers are about 12% of input powers, showing that near 100% output-fiber couplings are achieved, cf. Tab. 3.1.

3.3 Optical heating

With an optical path length of 5 mm in the vapor cell we do not see very much absorption signal at room temperature. This is even worse at high magnetic fields where there are 16 ground states, so only about 1/16 of the atoms populate the extreme angular momentum state of interest. To increase the absorption signal, the density of atoms needs to be increased. This is achieved by heating the vapor cell with a high-power laser beam.

In order to determine the temperature change of the vapor cell, when heated with a certain optical power, we take out the probe filter, and turn the probe power down, to minimize saturation of the transitions. Following Ref. [20], the laser-light intensity $I(L)$ after passing through the vapor is

$$I(L) = I(0)e^{-\rho\sigma(\nu)L}, \tag{3.3}$$

where $I(0)$ is the laser-light intensity before entering the vapor cell, ρ is the atomic density in the vapor, and L is optical path length in the vapor cell — i.e. twice the inner length of the cell, since the beam passes it twice. The optical absorption cross-section $\sigma(\nu)$ is

$$\sigma(\nu) = s \cdot \frac{c^2}{8\pi\nu_0^2} A_{21} g_{\mathrm{H}}(\nu), \tag{3.4}$$

where c is the speed of light, ν_0 is the resonance frequency, A_{21} is the decay rate of the excited state [34], and $g_{\mathrm{H}}(\nu)$ is the normalized Lorentzian

line shape function. The pre-factor s is a number in the range from 0–3, that depends on state degeneracies and light polarization. In the 0 T spectrum it should be 2, and in the 7 T spectrum it should be 3, according to the models presented in Ref. [20]. Here we keep it as an adjustable parameter, and determine it in the case of no heating and a known temperature, i.e. a known density. This way it also describes a possible small deviation in L from the design of $2 \times 5\,\mathrm{mm}$, and inaccuracies in estimated laser frequency scans.

3.3.1 Reference heating

For the reference probe at 0 T we scan the laser frequency across the hyperfine structure of the D_2 line, to record the absorption spectrum. This is shown in the case of no heating in Fig. 3.6. From Eqs. (3.3)

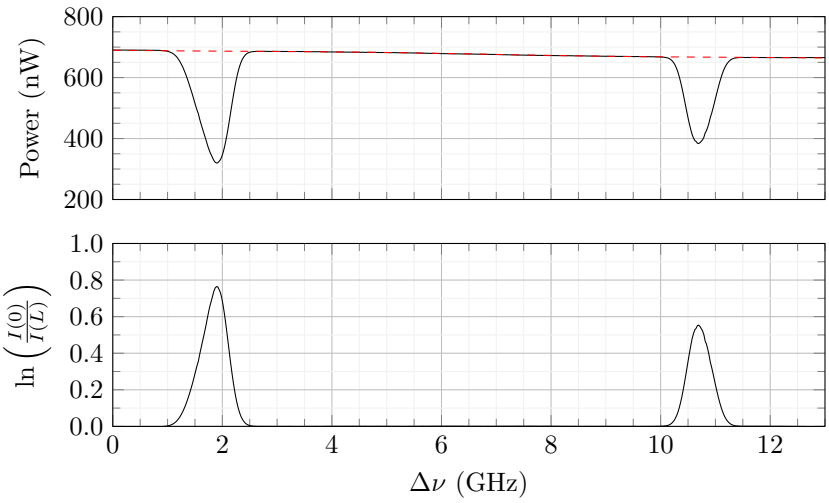

Figure 3.6: Density estimation with no heating. The upper plot shows the absorption spectrum (black curve), and the estimated laser power in the absence of atoms (red curve). The lower plot shows the logarithm of the fraction of those two quantities.

and (3.4) we find

$$\begin{aligned}\rho &= \ln\left(\frac{I(0)}{I(L)}\right)\frac{1}{\sigma(\nu)L} \\ &= \int_{-\infty}^{+\infty} \ln\left(\frac{I(0)}{I(L)}\right) d\nu \cdot \frac{1}{s \cdot \frac{c^2}{8\pi\nu_0^2} A_{21} L}.\end{aligned} \tag{3.5}$$

The optical power, in the absence of any atoms, is estimated by fitting an arbitrary function to the regions without absorption. The ratio of the powers without and with atoms must equal the ratio of the corresponding intensities $I(0)/I(L)$. The logarithm of this quantity is calculated and shown in Fig. 3.6. It is then integrated, and the density ρ is found. To account for the small saturation effects that remain despite the low probing power, four different probe powers are used, and the density is then extrapolated to zero, to give the best estimate of the true density. This is shown in Fig. 3.7. From the density ρ we can find the temper-

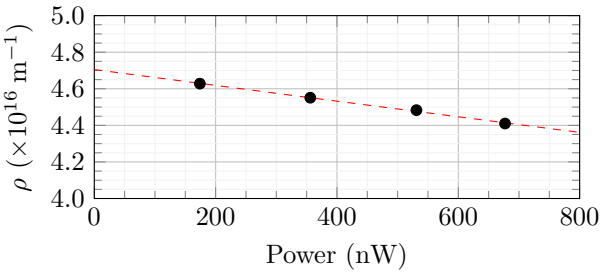

Figure 3.7: Density estimation with four different probe powers in black. Fitted extrapolation to zero in red. The value at zero power is considered to be without any saturation effect.

ature through the ideal gas law [40] and the vapor pressure model [34]. The pre-factor s is adjusted from 2 to 1.78 to give the density expected for the actual temperature measured with a thermometer next to the reference probe at 0 T. In Fig. 3.8 are shown spectra with six different heating powers and associated six different determined temperature changes relative to the surroundings.

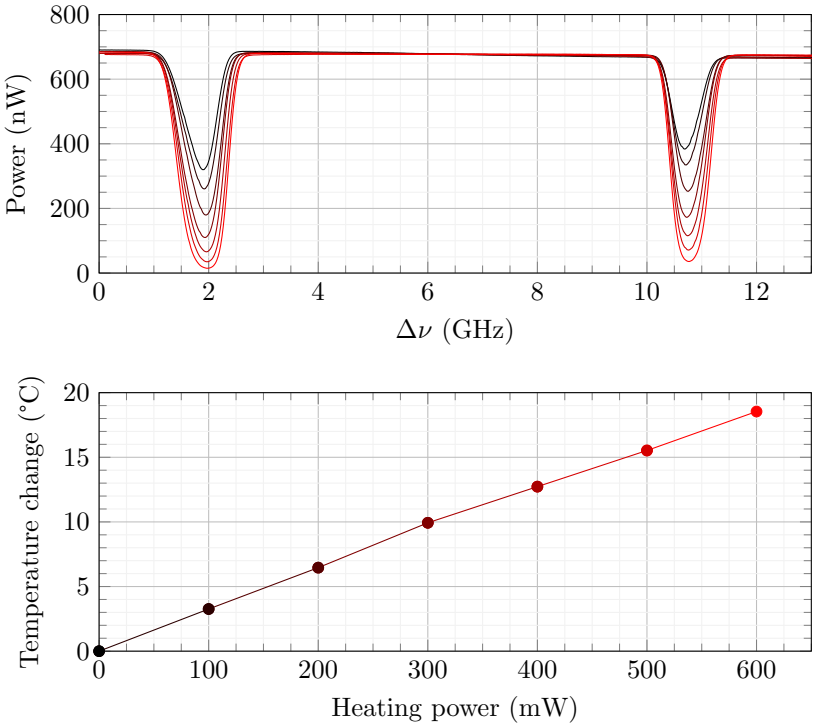

Figure 3.8: Optical heating of the reference probe. The upper plot shows spectra with heating of 0–600 mW of optical power. The lower plot shows calculated temperature changes for the corresponding heating powers.

3.3.2 Probe heating

A similar characterization is done for the probes when positioned inside the MRI scanner. A small difference is that only the eight ground states with $m_J = +\frac{1}{2}$ are probed. The population P_+ of the states with $m_J = +\frac{1}{2}$ will be lower than the population P_- of the states with $m_J = -\frac{1}{2}$, due to the energy difference of $E_+ - E_- = \mu_\mathrm{B} \cdot 2 \cdot 7\ \mathrm{T}$ [40]. We have

$$\frac{P_+}{P_-} = e^{-(E_+ - E_-)/kT}, \tag{3.6}$$

where k is the Boltzmann constant, so that at 50 °C we probe

$$P_+ = \left(e^{(E_+ - E_-)/kT} + 1\right)^{-1} = 49.3\%, \tag{3.7}$$

of the total population. We note that this is still very close to an equal distribution among the different m_J states. The expression in Eq. (3.5) is multiplied by $1/P_+$ to give the total density including the P_- population. Procedures similar to those shown in Figs. 3.6 and 3.7, and comparison with a temperature measurement inside the MRI scanner gives an adjustment of the pre-factor s from 3 to 2.75. In Fig. 3.9 are shown spectra with six different heating powers and associated six different determined temperature changes relative to the surroundings. Notice that more heating power is necessary in the MRI scanner, because of the higher heat dissipation compared to inside the magnetic shield where the reference probe is located. Also, higher temperatures are of interest because of the lower signal at 7 T. This is why up to double the heating power is explored for the probes in the scanner.

3.3.3 Non-equilibrium considerations

It is worth noting that upon receipt of the vapor cells, the cesium is distributed randomly over the inner surface. Over time, the localized optical heating of the cell will move the solid cesium towards the bottom of the stem, through evaporation and condensation. This process can take many days — if not weeks — of continuous heating. To speed things up, an initial procedure can be employed: The cell is mounted with the bottom of the stem in cold water, and a heat gun is used to heat the cell to a very high temperature. In a couple of minutes, the cesium can be moved very close to the bottom of the stem. After this the cell is mounted in the probe and heated optically until a density stable over several hours is reached.

When the optical heating is turned on, we see that it takes about an hour for the density to stabilize. We understand this as the time it takes for the probe to reach a stable thermal equilibrium, where the bottom

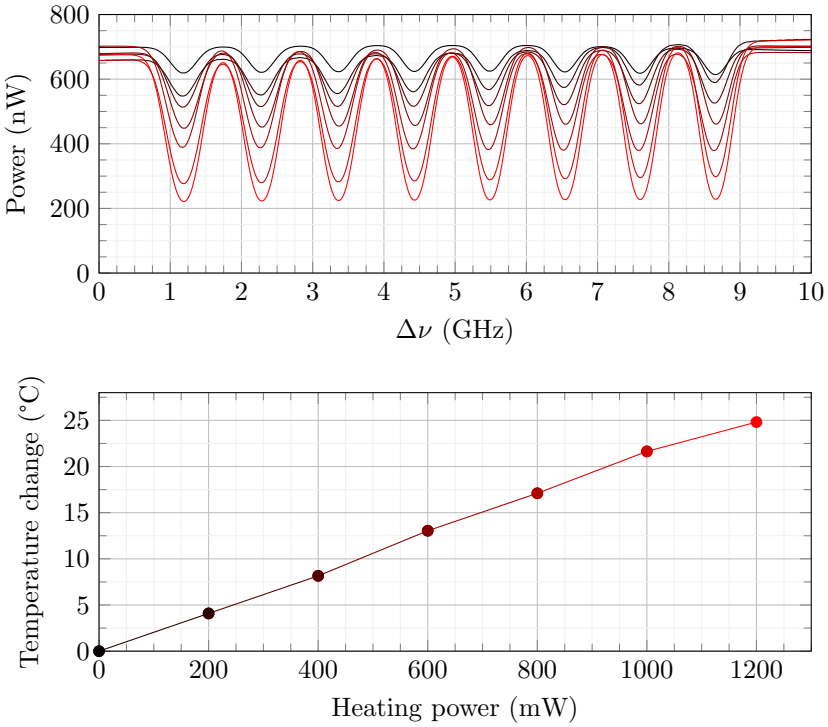

Figure 3.9: Optical heating of a probe in the MRI scanner. The upper plot shows spectra with heating of 0–1200 mW of optical power. The lower plot shows calculated temperature changes for the corresponding heating powers. For the calibration of the frequency axis, we use that the first and the last resonance are separated by 7.47 GHz. This value is both measured with sideband spectroscopy and confirmed by numerical diagonalization of the Hamiltonian.

of the stem is fully heated. Interestingly, during the first 10 minutes of heating, two peaks in the density are measured, as shown in Fig. 3.10. It seems that these peaks are higher when the probe has not been in use for longer times. An explanation is that, when the probe is not in use, cesium slowly distributes throughout the cell, through evaporation and condensation. The longer the probe rests, the more the cesium spreads. Once heating is turned on, the part of the cell in close thermal contact with the heating filter quickly heats up, and all atoms on this surface are released into the vapor. This is the first peak. When all atoms are released, and are condensed on the inner surface elsewhere, the density

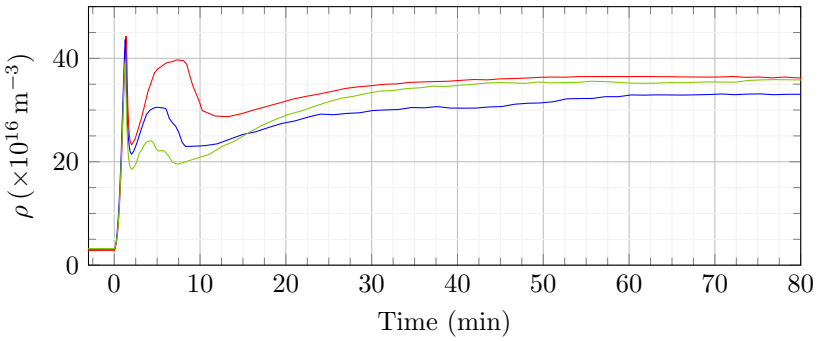

Figure 3.10: Laser heating of a probe vapor cell inside the MRI scanner, with 1200 mW of optical power. The red curve shows heating after a resting period of 3 months, the blue curve is for a resting period of 4 days, and the green curve is for a resting period of 1 day.

drops again. Next, the main volume of the cell heats up, producing the second peak, until this is similarly free of cesium atoms. Finally, the heat slowly propagates to the bottom of the stem, and a slow convergence towards equilibrium is seen. This idea is summarized in Fig. 3.11.

Measurements are performed during stable thermal equilibrium of the probes, for all the reported calculations. The temperatures at the bottom of the stem, where the solid or liquid cesium is located, are the ones that are calculated.

3.4 Signal optimization

A relevant question to ask is: What is the optimal temperature? Too much heating will make the vapor so dense that almost all the light is absorbed. Too little heating will mean that almost all light is passed through. A related question is then: What is the optimal probing power? Too high probing power will broaden the Doppler-free resonance too much. Too low probing power will give too little saturation.

In general, more heating should go together with more probing power, and the problem should be treated as a two-dimensional optimization problem. To investigate this problem, 6 different heating powers are

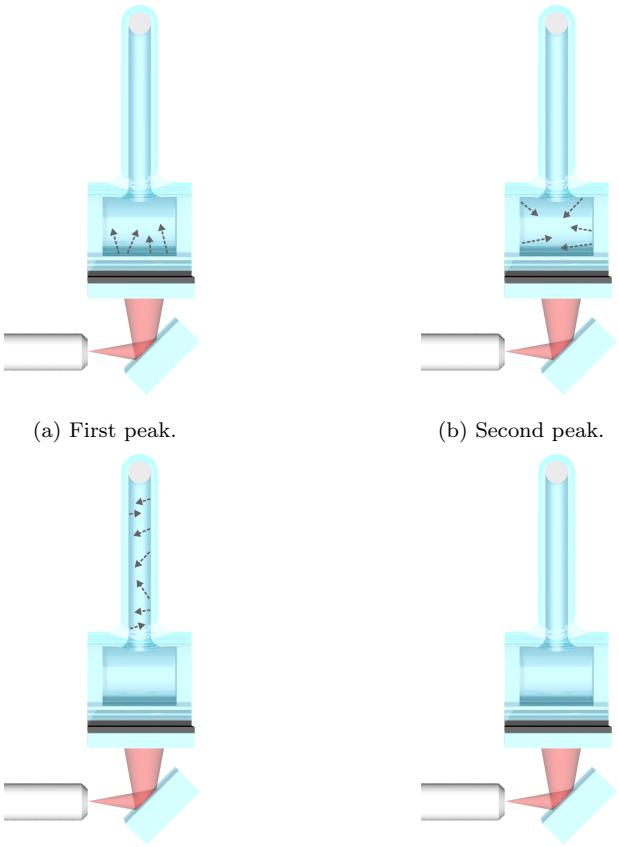

(a) First peak.

(b) Second peak.

(c) Converging.

(d) Equilibrium.

Figure 3.11: Optical heating of a vapor cell. (a) The rapid heating of the cell wall, in close contact with the heating filter, quickly releases cesium atoms producing the first sharp peak. (b) The subsequent heating of the main volume of the cell releases all atoms, producing the second peak. (c) The stem slowly heats up, and the bottom of the stem approaches the final temperature. (d) A thermal equilibrium is reached.

each tested with 10 different probing powers and the second derivative of the saturation peak, in the normalized transmission spectrum, is determined for each combination. The second derivative is a good measure of how "sharp" the peak is. For the reference this parameter exploration is shown in Fig. 3.12. It is seen that an optimum is found with a temperature around 34 °C and an (off-resonant) probing output power around

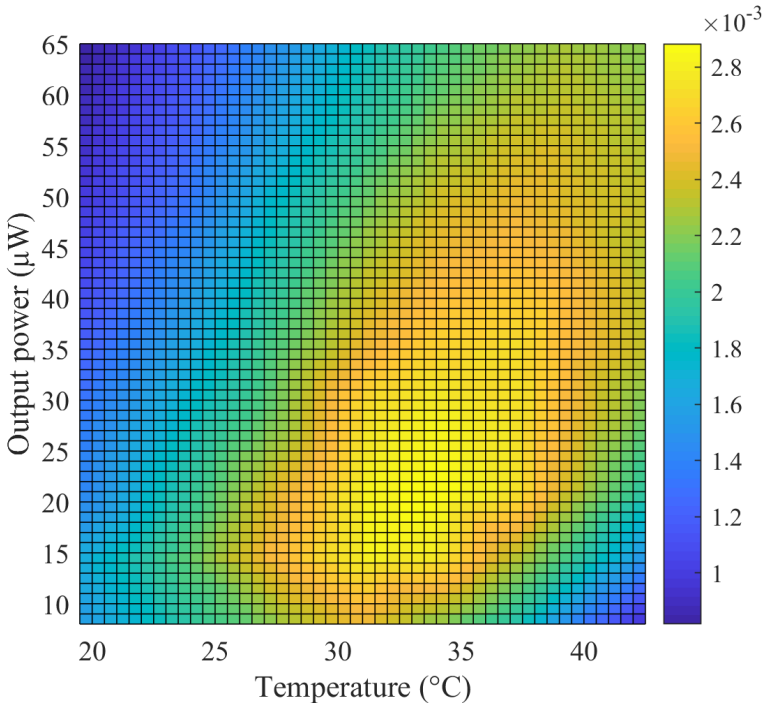

Figure 3.12: Optimization of the reference signal. Different temperatures and probing powers are tested, and an interpolation is made to increase the resolution of the plot. The color axis shows the second derivative of the saturation peak. Optimal signal is found with a temperature around 34 °C and a probing output power around 21 µW.

21 µW.

For the probes, where the hyperfine structure is larger than the Doppler broadening, more heating can be used, without approaching total absorption. Since the transition is a closed two-level system, a less sharp peak is seen compared to the reference transition. For the reference, the excited state has other decay channels, so what is seen is actually not saturation, but population depletion. The parameter exploration of a probe is seen in Fig. 3.13. It seems like the optimal temperature is not covered here. Higher heating powers have been tried, but associated thermal deformations of the probes made the transmission very unstable and rendered experiments practically impossible. For the

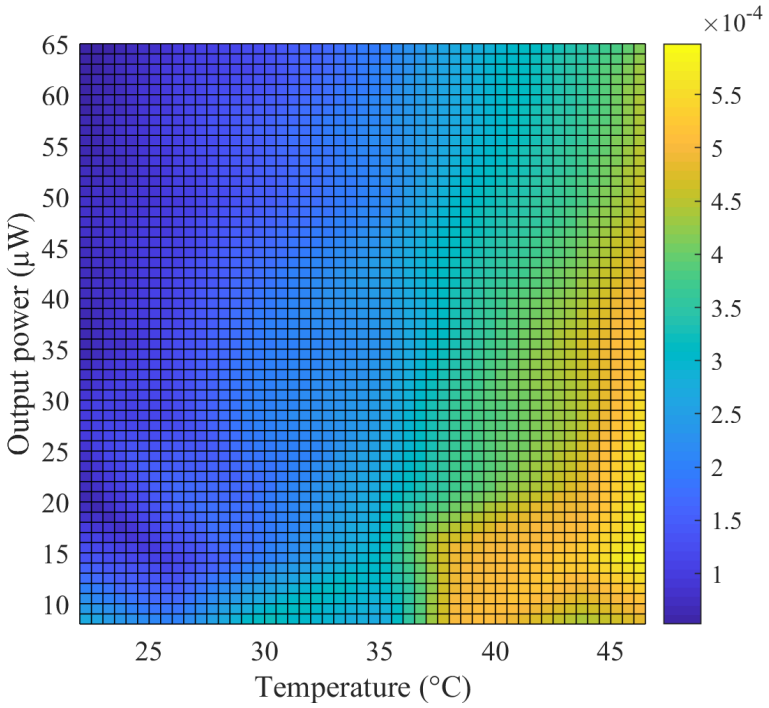

Figure 3.13: Optimization of the probe signal. Different temperatures and probing powers are tested, and an interpolation is made to increase the resolution of the plot. The color axis shows the second derivative of the saturation peak. It seems like the optimum is found outside the explored temperature range.

measurements in Ref. [1] the temperature was further lowered, compared to the maximum explored here. This was because the configuration with the four probes strapped together made the transmission even more unstable, as heat dissipation was much more inefficient. Notice also that lower heating powers were necessary in this configuration, compared to a single probe with the same temperature.

3.5 Susceptibility measurements

When probing a magnetic field, one has to be aware that the probe itself may affect the magnetic field. In fact, when measuring anything, one has

to consider the fact that the system is disturbed by the measurement. In the case of a magnetometer, the magnetic susceptibility of the probe has to be considered. Para- and diamagnetic components in the probe will become magnetised and contribute an induced magnetic field, which will add to the unprobed field. Since the induced field is typically in the ppm-range, the further magnetization of components due to the susceptibility-induced field will be vanishing, and the problem can be determined in a single step.

When introducing a magnetometer in an MRI scanner, two things should be considered: First, the probe will alter the magnetic field in its close proximity, i.e. introduce field inhomogeneities. This could impact imaging if the probe is positioned close to the imaged object. Second, the magnetic-field-sensitive volume, in this case the overlap of the cesium vapor and the probe-laser beam, will measure a field, shifted from what it was before the probe was introduced. To determine the field, as it would have been without a probe, this effect must be quantified and compensated. To do this, we must first determine the magnetic susceptibilities of the probe components.

All components of the probes are isolated and prepared for individual testing, as shown in Fig. 3.14. Where possible, the material has been shaped into a cylinder, as this makes modeling easy, and rotations of the sample can be ignored. Some of the components have been glued together to increase the volume and make the analysis less vulnerable to inaccuracies in geometrical measurements. The highly paramagnetic filters have been tested in two different geometries, to verify that results were similar despite some MR-signal loss due to high local field inhomogeneity.

The procedure for measuring the magnetic susceptibility of a sample is as follows: A sphere of water is placed in the MRI scanner, an MRI sequence for magnetic-field mapping is played, and the field is shimmed based on this map. The sphere of water is replaced with a sphere of water containing the sample, mounted on a thread close to the center of the sphere. The field-mapping sequence is played again, this time capturing

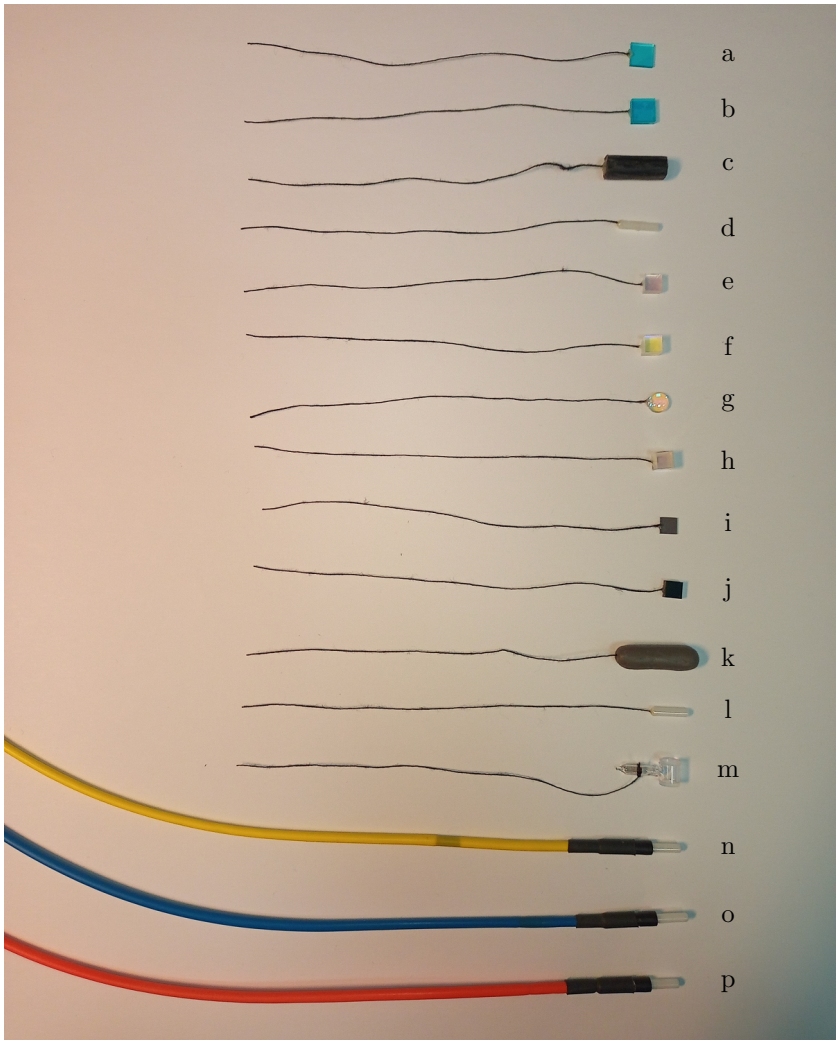

Figure 3.14: Samples prepared for susceptibility measurements. a: Heating filter (unknown material). b: Two heating filters glued together (unknown material). c: 3D print shaped into a cylinder (MJF Nylon PA12). d: Nylon bolt shaped into a cylinder (Nylon 66 UL94V-2). e: PBS (Schott N-SF1). f: Two mirrors glued together (Schott Borofloat 33). g: Lens (Schott N-BK7). h: Three quarter-wave plates glued together (quartz). i: Probe filter, 0.7 mm (Schott NG4). j: Probe filter, 2.5 mm (Schott NG4). k: Heat conductor shaped into a cylinder with rounded edges (silicone, RS 174-5694). l: Fiber ferrule (zirconia). m: Cell (fused silica). n: Heating fiber. o: Input fiber. p: Output fiber.

the field distortions induced by the sample. The field distortions are proportional to the difference between the water magnetic susceptibility and the sample magnetic susceptibility. Furthermore, the distortion depends on the geometrical shape of the sample, and the orientation relative to the magnetic field. In Fig. 3.15 we show a zirconia sample, i.e. a fiber ferrule, positioned in a sphere of water for measurement, along with an MR image of the construct. The field-mapping sequence produces both a

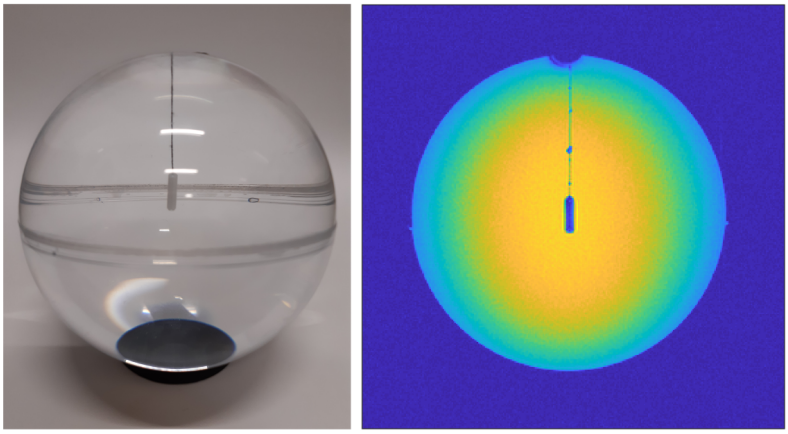

Figure 3.15: To the left is shown the zirconia sample, i.e. a fiber ferrule, submerged in ultrapure water in a spherical container. To the left is shown a central vertical slice of the MR image of the setup. The MRI sequence used here returns a 3D image of both the signal strength and the field shift. The signal strength image, shown here, is used to locate the sample.

3D image of the signal strength, and an image of the measured field shift. The signal-strength image can conveniently be used to locate the sample, as it shows up dark, since it does not contain any water. Locating a 2D slice through the center of the sample, and the surrounding water, the corresponding field-shift map is used to determine the magnetic susceptibility. This is done by constructing a 3D model of the sample, calculating the field shift assuming a magnetic susceptibility of 1 ppm, and then fitting the central 2D slice of this model to the measured field-shift map, by allowing it to be displaced and scaled. This is shown for

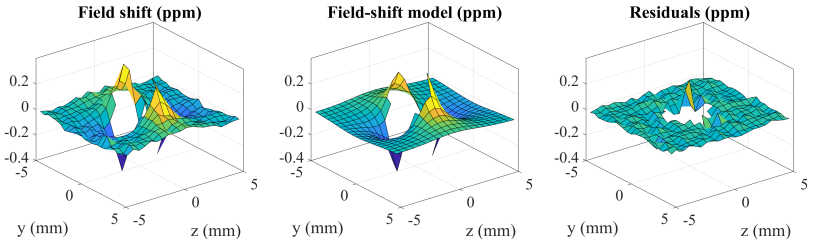

Figure 3.16: To the left is shown a horizontal slice through the MR image of the field-shift, in the area around the zirconia sample. The field-shift values are shown on the vertical axis. In the center is shown the field-shift model, scaled to best fit the MR image. To the right are displayed the residuals between the image and the scaled model, showing good agreement.

the zirconia sample in Fig. 3.16. The scaling of the model that produces the best fit, is the difference in water and sample magnetic susceptibility. All measurements and the calculated compensation factor are presented in Ref. [1]. All models, fits, and analyses are included in Ref. [3].

This method is largely the one described in Refs. [41]. A minor difference is that the field-shift models used here, are made with the fast Fourier-based method described in Refs. [42,43], instead of the slow finite element method. Also, since machining of glass components into simple shapes seemed troublesome, models of more complicated shapes, such as a lens, have here been implemented successfully. This demonstrates that the method is in fact very versatile.

4 Generating Sidebands by Electro-Optic Modulation

The ability to generate sidebands, shifted by a well-known amount from the carrier, has been a crucial part of this work. Here we review the basics of optical phase modulation, verify that the theoretical predictions work well, and investigate future possibilities for exploring fields beyond 7 T. The focus will be on the generation of strong fifth sidebands shifted $\pm 5 \times 19.5\,\mathrm{GHz}$ from the carrier frequency, as this is a quite non-standard task.

An electromagnetic field with amplitude E_0, frequency ν, and the phase modulated by $\phi(t)$, can be written as

$$E(t) = E_0 \cos\big(2\pi\nu t + \phi(t)\big). \tag{4.1}$$

The field is evaluated at the time t. When the modulation is a sinusoid of amplitude ϕ_0 and frequency ν_m,

$$\phi(t) = \phi_0 \sin(2\pi\nu_m t), \tag{4.2}$$

then the field can be expressed as

$$E(t) = E_0 \sum_{n=-\infty}^{\infty} J_n(\phi_0) \cos\big(2\pi(\nu + n\nu_m)t\big), \tag{4.3}$$

as shown in Ref. [44]. Here $J_n(\phi_0)$ are Bessel functions of the first kind, of order n, evaluated at ϕ_0. We see that the carrier frequency ν, is accompanied by sideband frequencies of $\nu \pm n\nu_m$. The relative powers are given by $\big(J_n(\phi_0)\big)^2$. The Bessel functions of order 0–10 are shown

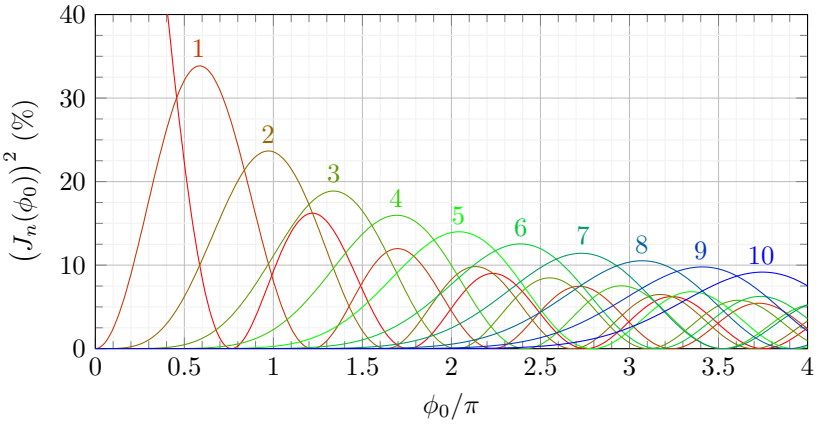

Figure 4.1: The Bessel functions of order 0–10, labelled at their peak value. We see that to optimize power for the fifth sidebands a modulation depth ϕ_0/π of 2.05 is required.

in Fig. 4.1, plotted against the modulation depth ϕ_0/π. The actually realized modulation depth in an EOM is

$$\frac{\phi_0}{\pi} = \frac{V}{V_\pi}, \tag{4.4}$$

where V is the applied voltage, and V_π is the half-wave voltage of the EOM. The high-power EOM used for this task has $V_\pi = 3.3\,\mathrm{V}$, so to drive the EOM to a modulation depth of 2.05, for maximum optical power in the fifth sidebands, we need a voltage of amplitude $V = 6.77\,\mathrm{V}$. In a $50\,\Omega$ system this corresponds to 26.6 dBm (0.46 W) of electrical rf power. This is just short of what the most powerful amplifier from iXblue (the supplier of all EOMs used in this work) can supply [45], so a 36 dBm (4 W) amplifier has been acquired elsewhere, to address this need.

To be able to tune the rf power to the point of maximum fifth sideband power, an rf mixer is inserted between the synthesizer and the amplifier, as shown in Fig. 4.2. The mixer is used as a variable attenuator by driving the intermediate-frequency input with a DC current controlled by two potentiometers. Along with a fixed attenuator of 6 dB, and about 5 dB attenuation from cables and connectors, we have a to-

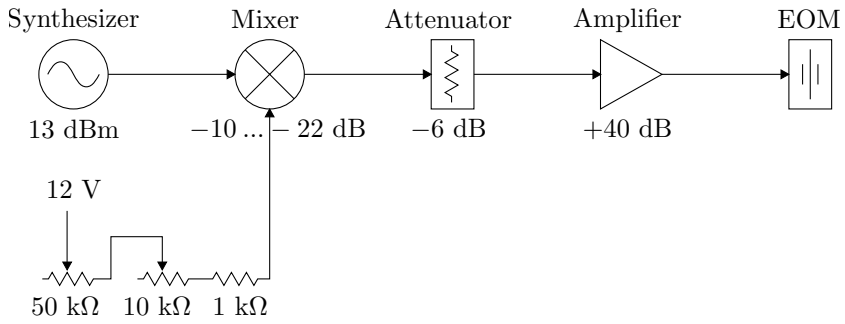

Figure 4.2: The rf chain amplifying the signal from the synthesizer for deep electro-optic modulation. Two potentiometers are used for course- and fine-tuning of the variable attenuation implemented by the mixer. Including an additional 5 dB attenuation from cables and connectors, we have an EOM drive power in the range 20–32 dBm.

tal tunable power of about 20–32 dBm (0.1–1.6 W) reaching the EOM. This corresponds to a modulation-depth range of about 1.0–3.8. Scanning the laser frequency such that the fifth lower sideband is probing the 0 T transition, we can clearly find the point of maximum fifth sideband power, and also the second local maximum around $\phi_0/\pi = 3.35$.

According to Fig. 4.1 about 14% of the power should be available in either of the fifth sidebands, when maximized. To verify that this is the case, we heat a probe at 0 T with 1.2 W of optical power and record the transmission during the first brief high-density peak, cf. Fig. 3.10, while scanning the laser frequency such that the lower fifth sideband is probing the transition. This is shown in Fig. 4.3. Comparing to Fig. 3.8 we expect to see practically 100% absorption of resonant light, in this situation. Indeed, we see about 14% absorption here, confirming that this is the total amount of power in the lower fifth sideband. So, the electro-optic modulation nicely performs according to theory.

The calculations presented here indicate that the EXAAQ magnetometer could readily be used up to 14 T, by using the 10^{th} sideband for reference locking. Similarly, the γ_1 and γ_2 determinations could be performed with much better accuracy, with the current hardware and

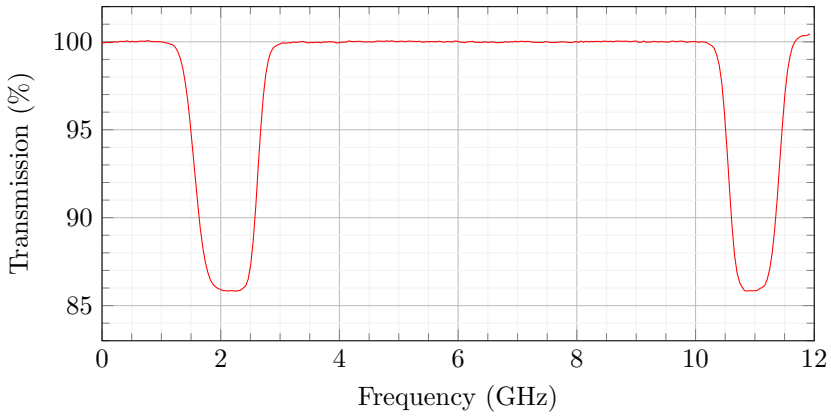

Figure 4.3: Total absorption of the fifth lower sideband by the 0 T transition. The data has been processed to take detector offset and frequency-scanning power variations into account. The frequency scan is determined by the peak separation.

access to a 14 T MRI scanner. It should be noted that only 9.2% of the power will be available in the 10^{th} sideband, which will impact the signal-to-noise ratio negatively, and also that the full range up to 14 T is not available, since the amplifier bandwidth is limited to 17.5–21.5 GHz. An alternative to using higher-order sidebands to access higher fields, is to use higher modulation frequencies. Care should, however, be taken in the system design, since V_π also tend to increase slightly with higher EOM bandwidth. Bandwidths beyond 20 GHz are not standard but may be supplied upon request. In general, the involved components are non-standard and expensive, but the field is rapidly progressing, so a setup that is pushing the technological limits today, may become cheaper or better in the near future. A picture of the rf chain is shown in Fig. 4.4.

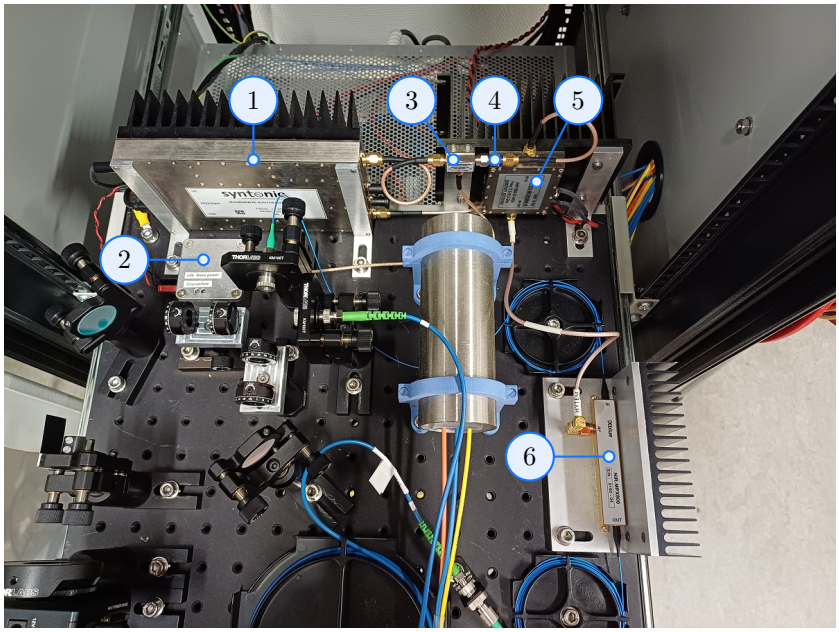

Figure 4.4: Photo of the rf chain sketched in Fig. 4.2. 1: Synthesizer. 2: Potentiometers. 3: Mixer. 4: Fixed attenuator. 5: Amplifier. 6: High-power EOM. Significant amounts of heat are generated and dissipated by the components, so rather large heatsinks are employed. The components are mounted on a breadboard along with the free-space beam-splitting optics, and the custom-made two-layer magnetic shield with the reference probe. The breadboard is seen with a transparent blue dust cover on in Fig. 5 of Ref. [2] (page 80 in this thesis). Holes are cut such that the heatsinks are outside the cover.

5 First Paper: "Precision Measurement of the Excited State Landé g-factor and Diamagnetic Shift of the Cesium D_2 Line"

This paper was published in Physics Review X on June 20 2023, with the accompanying popular summary:

"Despite the success of optical magnetic-field sensors in many different applications, most work only for relatively low magnetic fields. Optical magnetometers for high magnetic fields function by tracking an optical atomic resonance – a particular frequency of light that can be absorbed by an atomic gas — that depends on magnetic fields. A big obstacle for optical high-magnetic-field sensing is that the exact magnetic-field dependence of such resonances, characterized by two atomic coefficients, is quite poorly known. Here, we report high precision measurements of those coefficients for the cesium atom, such that magnetic fields now can be inferred optically with parts-per-million accuracy.

We achieve this precision by taking advantage of the very stable and homogeneous field inside a magnetic resonance imaging scanner. We first measure the field with a traditional nuclear magnetic resonance method,

and then put the cesium gas in the field and measure the optical frequency shift of the atomic resonance. With this approach, we determine the two coefficients several hundred times better than ever before.

Our result paves the way for realizing a fully functioning optical magnetometer for high magnetic fields, which will be explored in the next stage of our experiment together with its further applications."

Precision Measurement of the Excited State Landé g-factor and Diamagnetic Shift of the Cesium D_2 Line

Hans Stærkind,[1,2,*] Kasper Jensen,[1,3] Jörg H. Müller,[1] Vincent O. Boer,[2] Esben T. Petersen,[2,4] and Eugene S. Polzik[1]

[1]*Niels Bohr Institute, University of Copenhagen, Blegdamsvej 17, 2100 Copenhagen, Denmark*
[2]*Danish Research Centre for Magnetic Resonance, Centre for Functional and Diagnostic Imaging and Research, Copenhagen University Hospital—Amager and Hvidovre, Kettegård Allé 30, 2650 Hvidovre, Denmark*
[3]*School of Physics and Astronomy, University of Nottingham, University Park, Nottingham NG7 2RD, United Kingdom*
[4]*Section for Magnetic Resonance, DTU-Health Tech, Technical University of Denmark, Oersteds Plads, Building 349, 1st floor, 2800 Kgs Lyngby, Denmark*

(Received 2 August 2022; accepted 24 February 2023; published 20 June 2023)

Transitions between the extreme angular-momentum states of alkali D lines hold the potential for enabling accurate high-field optical magnetometry because of their very simple magnetic field dependence described only by a linear and a quadratic term, characterized by the two coefficients γ_1 and γ_2. Here, we present very accurate measurements of these coefficients, for the cesium D_2 line, thereby overcoming a major obstacle for the realization of this future technology. By means of saturated absorption spectroscopy on a cesium gas, in 3 T and 7 T magnetic fields, we measure the linear magnetic frequency shift of the transition to be $\gamma_1 = 13.994\,301(11)$ GHz/T. This measurement corresponds to an optical magnetic field determination of better than 1 ppm accuracy. From this value, we can calculate the fine-structure Landé g-factor $g_J(6^2P_{3/2}) = 1.334\,087\,49(52)$. This result is consistent with the previous best measurement, and it improves the accuracy by more than 2 orders of magnitude. We also measure, for the first time, the quadratic diamagnetic shift as $\gamma_2 = 0.4644(35)$ MHz/T^2. Our work opens up the field of accurate high-field optical magnetometry using atomic cesium, with possible applications in, e.g., medical MRI, fusion reactors, and particle accelerators. These high-accuracy measurements also allow for testing of advanced atomic structure models, as our results are incompatible with the Russel-Saunders coupling value and the hydrogen-constant-core-model value by 31 and 7 standard deviations, respectively.

DOI: 10.1103/PhysRevX.13.021036 Subject Areas: Atomic and Molecular Physics, Optics

I. INTRODUCTION

The field of optical magnetometry has undergone rapid development during the last couple of decades [1]. While devices for measuring tiny magnetic fields have matured to the point of emerging practical applications, e.g., magnetocardiography and magnetoencephalography [2–5], optical magnetometers for high magnetic fields are still at a less advanced level.

Low-field optical magnetometry typically works by optical detection of the Larmor precession of optically pumped atomic spins [1]. High-field optical magnetometers, on the other hand, usually rely on measuring the Zeeman shift of the optical absorption lines. Much of the work is focused on the D lines of alkali vapors [6–9]. In other work, not directly aimed at magnetometry applications, (nonlinear) spectroscopy and optical pumping of alkali atoms in high magnetic fields have been studied [10–15].

Currently, accurate measurements of magnetic fields in the tesla range are typically performed using nuclear magnetic resonance (NMR) spectroscopy on protons in water [16]. NMR measurements are highly sensitive but require the application and detection of radio frequency (rf) magnetic pulses. Optical magnetometry provides a completely different way of measuring high magnetic fields, with advantages such as continuous and fast readout without rf, electronic, or metallic components in the field probe. Optical magnetometry also allows for remote detection, e.g., measurements on exploding wires [17–20] and sunspots [21]. Indeed, the observation of sodium line splitting in sunspots dates all the way back to 1870 [22].

*hans.staerkind@nbi.ku.dk

On Earth, high magnetic fields are found in magnetic resonance imaging (MRI) scanners, NMR spectrometers, particle accelerators, fusion reactors, and a range of advanced physics experiments [23].

A major roadblock for the practical use of optical magnetometry for high fields is currently the accuracy with which the excited state g-factors of the alkali D lines are known [7,23]. In order to enable accurate high-field optical magnetometry, we here present an improved measurement of the excited state Landé g-factor for the cesium D_2 line, along with the first-ever measurement of the diamagnetic shift of this line. By using a 3 T and a 7 T MRI scanner, we have very stable and homogeneous high magnetic fields and, at the same time, all the hardware needed to accurately determine these fields using NMR spectroscopy. To determine optical frequency shifts in these fields, we realize saturated absorption spectroscopy inside the MRI scanners. By combining NMR and optical measurements, more than 2 orders-of-magnitude improvement in accuracy is achieved for the excited state g-factor, compared to previous work.

The data presented here also surpass the accuracy of published theoretical values from atomic structure calculations. Hence, as a spin-off, our data can be used to test advanced atomic structure models.

II. SPLITTING OF THE D_2 LINE

We consider the transition from the cesium-133 ground state $6^2S_{1/2}$ to the excited state $6^2P_{3/2}$, known as the D_2 line. With saturated absorption spectroscopy, the limitation of Doppler broadening is surpassed, and the hyperfine splitting of this line can readily be resolved [24]. In the following, we review how the line splitting depends on an applied magnetic field in the tesla range. We consider the Zeeman interaction in detail and simply take the hyperfine shift to be

$$\Delta E_{\mathrm{HFS}} = \frac{1}{2}A\big(F(F+1) - I(I+1) - J(J+1)\big). \quad (1)$$

Here, F, I, and J are the atomic, nuclear, and electronic total angular-momentum quantum numbers, respectively. The magnetic dipole hyperfine coupling constant A is $h\times 2.298\,157\,942\,5\,\mathrm{GHz}$ for the ground state [25,26], and $h\times 50.288\,27(23)\,\mathrm{MHz}$ for the excited state [26,27], where h is the Planck constant [28]. For a more detailed treatment of the hyperfine structure including electric quadrupole and magnetic octupole interactions, which are not relevant to the results in this work, see Refs. [25–27,29].

A. Zeeman shift

As described in Refs. [25,26,29], the Zeeman shift of a state can be written as

$$\Delta E_{\mathrm{Z}} = (g_S m_S + g_L m_L + g_I m_I)\mu_{\mathrm{B}} B. \quad (2)$$

Here, g_S and g_L are the electron spin and orbital g-factors, respectively, and g_I is the nuclear g-factor. Additionally, m_S, m_L, and m_I are the electron spin, electron orbital, and nuclear projected angular-momentum quantum numbers, respectively; μ_{B} is the Bohr magneton [28]; and B is the magnitude of the magnetic field whose direction defines the quantization axis. In the following, B is referred to simply as the magnetic field. We include a finite nuclear mass correction for the orbital g-factor, $g_L = m_{\mathrm{N}}/(m_{\mathrm{N}} + m_{\mathrm{e}}) \approx 1 - m_{\mathrm{e}}/m_{\mathrm{N}}$ [26,29,30]. Here, m_{e} is the electron mass, and m_{N} is the nuclear mass. Equation (2) is the appropriate equation to use in the case of kilotesla fields, i.e., in the fine Paschen-Back regime, where the Zeeman shift is large compared to the fine structure. For a Zeeman shift that is small compared to the fine structure but large compared to the hyperfine structure, i.e., in the hyperfine Paschen-Back regime, where our two MRI scanners operate, we can write the shift as

$$\Delta E_{\mathrm{Z}} = (g_J m_J + g_I m_I)\mu_{\mathrm{B}} B, \quad (3)$$

with the Landé g-factor g_J approximately given by the Russell-Saunders (RS) coupling value [26,29,30]

$$g_J = g_L \frac{J(J+1) - S(S+1) + L(L+1)}{2J(J+1)} + g_S \frac{J(J+1) + S(S+1) - L(L+1)}{2J(J+1)}. \quad (4)$$

Here, S and L are the total electronic spin and orbital angular-momentum quantum numbers, respectively. When the Zeeman shift is small compared to the hyperfine structure, i.e., in the Zeeman regime, we can write the shift as

$$\Delta E_{\mathrm{Z}} = g_F m_F \mu_{\mathrm{B}} B, \quad (5)$$

with the Landé g-factor g_F as given in Ref. [26] and m_F being the atomic projected angular-momentum quantum number.

Numerically diagonalizing the total Hamiltonian composed of the hyperfine Hamiltonian, equivalent to Eq. (1), and the Zeeman Hamiltonian, equivalent to Eq. (3), and ignoring the small nuclear Zeeman interaction $g_I m_I \mu_{\mathrm{B}} B$, we can visually inspect the magnetic field dependence of the states as we transition from the Zeeman regime into the hyperfine Paschen-Back regime. This magnetic field dependence is shown for the ground and excited states in Figs. 1(a) and 1(b), respectively. Groups of states are labeled with quantum numbers; primes are used for excited state quantum numbers. Notice how the Zeeman interaction acts as a perturbation to the hyperfine splitting at low fields, breaking the degeneracy of the different m_F states. At high

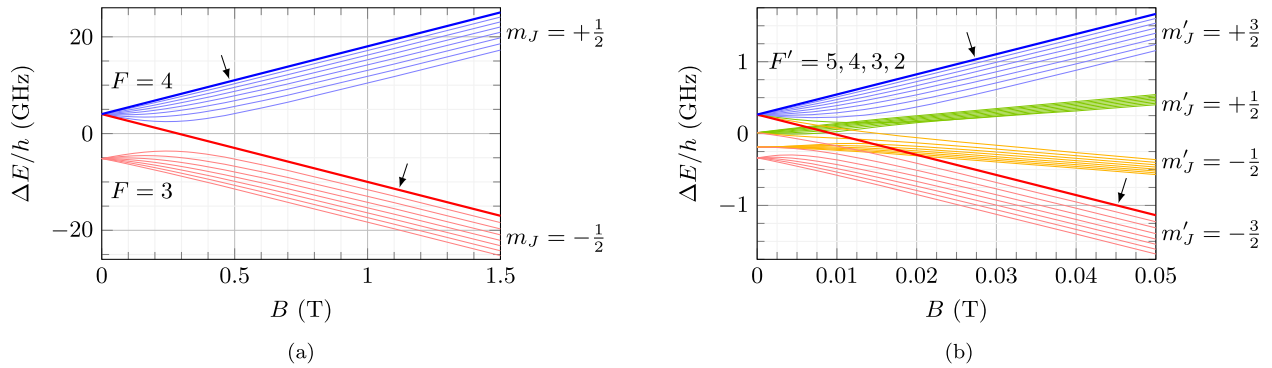

FIG. 1. Energy splitting for the ground and excited states, as a function of applied magnetic field. The two different magnetic field axes are chosen to highlight the evolution from the Zeeman regime to the hyperfine Paschen-Back regime for the two states. (a) Ground state, $6^2S_{1/2}$, energy splitting. The bold blue line is the $|F, m_F\rangle = |4, 4\rangle$ state, and the bold red line is the $|4, -4\rangle$ state. Both are marked with arrows. (b) Excited state, $6^2P_{3/2}$, energy splitting. The bold blue line is the $|F', m'_F\rangle = |5, 5\rangle$ state, and the bold red line is the $|5, -5\rangle$ state. Both are marked with arrows.

fields, the hyperfine interaction acts as a perturbation to the Zeeman splitting breaking the degeneracy of the eight m_I states, $-\frac{7}{2}$ to $+\frac{7}{2}$. The hyperfine Paschen-Back regime occurs at different magnetic fields due to the different hyperfine coupling constants of the ground and excited states, and it continues well beyond the 7 T relevant for this study.

B. Extreme angular-momentum states

Now, we turn our attention to the σ_+ transition between the extreme angular-momentum states, i.e., the transition between the ground state with maximum total and projected angular momenta, $|F, m_F\rangle = |4, 4\rangle$, and the excited state with maximum total and projected angular momenta, $|F', m'_F\rangle = |5, 5\rangle$. We call this the extreme σ_+ transition. The two states of this transition do not mix with any of the other angular-momentum states when we transition from the Zeeman regime to the hyperfine Paschen-Back regime and ultimately into the fine Paschen-Back regime. The labeling of the two states in the different regimes is summarized in Table I. Notice that, for both states, the projected angular-momentum quantum numbers are equal to the corresponding total angular-momentum quantum numbers, and the sums of all the projected angular-momentum quantum numbers are the same in all regimes. The frequency shifts of these states are linearly dependent on the magnetic field in all regimes and also in the intermediate regimes. Hence, the extreme σ_+ transition is also linearly dependent on the magnetic field.

In Fig. 2, $\sigma_\pm$ transitions in the hyperfine Paschen-Back regime are shown, along with their extensions into the Zeeman regime. The electric-dipole-allowed strong $\sigma_\pm$ transitions are those obeying the selection rules $\Delta m_J = \pm 1$ [31] and, by conservation of angular momentum, $\Delta m_I = 0$. The extreme σ_+ transition is highlighted in bold blue. The weaker transitions with $\Delta m_I = \pm 1$, forbidden in the high-field limit, are also shown.

Highlighted in bold red in Fig. 2 is the extreme σ_- transition $|4, -4\rangle \leftrightarrow |5, -5\rangle$, i.e., the transition between the

TABLE I. Labeling of the extreme angular-momentum states in the three regimes.

	Zeeman	Hyperfine Paschen-Back	Fine Paschen-Back
	$\lvert F, m_F\rangle$	$\lvert J, m_J, I, m_I\rangle$	$\lvert L, m_L, S, m_S, I, m_I\rangle$
Ground state	$\lvert 4, 4\rangle$	$\lvert \frac{1}{2}, \frac{1}{2}, \frac{7}{2}, \frac{7}{2}\rangle$	$\lvert 0, 0, \frac{1}{2}, \frac{1}{2}, \frac{7}{2}, \frac{7}{2}\rangle$
Excited state	$\lvert 5, 5\rangle$	$\lvert \frac{3}{2}, \frac{3}{2}, \frac{7}{2}, \frac{7}{2}\rangle$	$\lvert 1, 1, \frac{1}{2}, \frac{1}{2}, \frac{7}{2}, \frac{7}{2}\rangle$

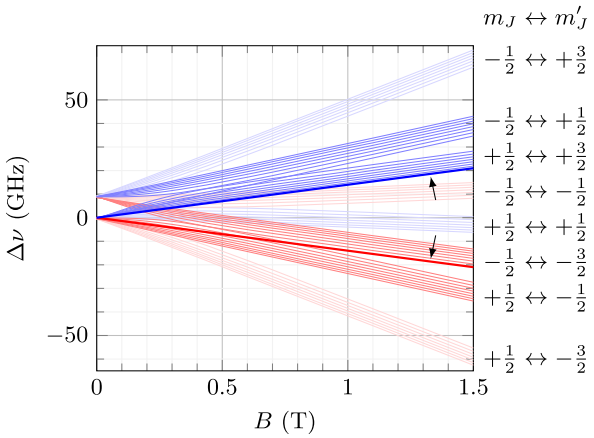

FIG. 2. Splitting of the D_2 line in a magnetic field. The blue lines correspond to σ_+ transitions; the red lines correspond to σ_- transitions. The bold blue line is the extreme σ_+ transition. The bold red line is the extreme σ_- transition. Both lines are marked with arrows. Light-colored lines correspond to the weak transitions with $\Delta m_I = \pm 1$. The shifts $\Delta\nu$ are relative to the extreme $\sigma_\pm$ transitions at 0 T. To the right of the figure, we give the ground state m_J and excited state m'_J for the transitions.

negative extreme angular-momentum states, which is similarly linearly dependent on the magnetic field (but with the opposite sign) and has the same transition frequency at 0 T.

An experimental overview confirming the splitting pattern in Fig. 2, from 0 T to 1.5 T, is presented in Appendix H. This range of magnetic fields highlights the evolution from the Zeeman regime to the hyperfine Paschen-Back regime.

By expanding the atomic Hamiltonian accounting for the momentum of the magnetic field, a term quadratic in the magnetic field appears [7,32–35]. This is the diamagnetism of the atom, and for non-Rydberg states, it is typically neglected since it is much smaller than the linear term. For our purpose, however, we cannot neglect it, and thus, the linear shift of the two extreme transitions is supplemented by a quadratic one [not shown in Figs. 1(a), 1(b), and 2]. The expected coefficient ξ^{dia} to the quadratic term, within the hydrogen-constant-core-model (HCCM), is given by

$$\xi^{\mathrm{dia}} = \frac{5e^2a_0^2}{8m_{\mathrm{e}}}\left(1+\frac{1-3L(L+1)}{5(n^*)^2}\right) \times \frac{L(L+1)+m_L^2-1}{(2L-1)(2L+3)}(n^*)^4, \tag{6}$$

following the conventions of Ref. [7]. Here, n^* is the effective principal quantum number [7,36], e is the electron charge, a_0 is the Bohr radius, and m_{e} is the electron mass [28]. Using the reduced electron mass, due to the finite nuclear mass, is not relevant for the first five digits. The quadratic dependence on m_L implies that this shift, including the sign, is the same for the two extreme transitions.

The resulting model constitutes a good operational description of the magnetic field dependence of the extreme transitions, making them highly useful for accurate magnetometry as described in the next section.

III. HIGH-FIELD MAGNETOMETRY WITH CESIUM

Using Eq. (3) and (6), the magnetic-field-dependent frequency shifts are, for the positive and negative extreme angular-momentum ground states,

$$\Delta\nu_{\mathrm{g}\pm} = \pm\left(g_J(6^2S_{1/2})\cdot 1/2 + g_I\cdot 7/2\right)\frac{\mu_{\mathrm{B}}}{h}B + \frac{\xi_{\mathrm{g}}^{\mathrm{dia}}}{h}B^2, \tag{7}$$

and for the positive and negative extreme angular-momentum excited states,

$$\Delta\nu_{\mathrm{e}\pm} = \pm\left(g_J(6^2P_{3/2})\cdot 3/2 + g_I\cdot 7/2\right)\frac{\mu_{\mathrm{B}}}{h}B + \frac{\xi_{\mathrm{e}}^{\mathrm{dia}}}{h}B^2. \tag{8}$$

Notice how the nuclear Zeeman shifts of the two states involved in each of the two extreme transitions are the same, so they do not contribute to the magnetic field dependence of the transitions,

$$\begin{aligned}\Delta\nu_{\pm} &= \Delta\nu_{\mathrm{e}\pm} - \Delta\nu_{\mathrm{g}\pm} \\ &= \pm\left(g_J(6^2P_{3/2})\cdot 3/2 - g_J(6^2S_{1/2})\cdot 1/2\right)\frac{\mu_{\mathrm{B}}}{h}B \\ &\quad + \frac{1}{h}\left(\xi_{\mathrm{e}}^{\mathrm{dia}} - \xi_{\mathrm{g}}^{\mathrm{dia}}\right)B^2.\end{aligned} \tag{9}$$

Defining, for simplicity,

$$\gamma_1 \equiv \frac{\mu_{\mathrm{B}}}{h}\left(g_J(6^2P_{3/2})\cdot 3/2 - g_J(6^2S_{1/2})\cdot 1/2\right), \tag{10}$$

$$\gamma_2 \equiv \frac{1}{h}\left(\xi_{\mathrm{e}}^{\mathrm{dia}} - \xi_{\mathrm{g}}^{\mathrm{dia}}\right), \tag{11}$$

we find

$$\Delta\nu_{\pm} = \pm\gamma_1 B + \gamma_2 B^2. \tag{12}$$

In practice, for fields in the tesla range, it is useful to modify this expression to

$$\Delta\nu_{\pm} = \gamma_0 \pm \gamma_1\zeta B + \gamma_2\zeta^2 B^2, \tag{13}$$

where γ_0 is an experimental offset in the frequency shift measurement, and ζ is a factor describing the magnetic field shift introduced by the magnetic susceptibility of the probe—that is, the structure containing the cesium vapor—such that B is defined as the magnetic field in the absence of the probe. Ideally, the offset γ_0 should be small compared to the linewidth of the transition, and the probe field shift ζ should deviate from 1 only by a few ppm.

Using this relation, accurate high-field magnetometry can be performed by measuring the optical frequency shifts $\Delta\nu_{\pm}$. However, knowledge of γ_1 is limited by the large uncertainty on the excited state Landé g-factor $g_J(6^2P_{3/2})$, and neither γ_2 nor its constituents have ever been measured before.

In order to enable accurate high-field magnetometry with cesium, we here present a highly improved measurement of γ_1, and therefore also of $g_J(6^2P_{3/2})$. We also present a first-ever measurement of γ_2.

IV. CURRENT BEST NUMBERS

The value for the cesium ground state Landé g-factor is, according to Ref. [25], determined from experimental data as 2.002 540 32(20). This calculation is based on accurate measurements of the free electron g-factor $g(e)$; the ratio

between the rubidium ground state and the free electron g-factors, $g_J(\mathrm{Rb})/g(e)$; and the ratio between the cesium and the rubidium ground state g-factors, $g_J(\mathrm{Cs})/g_J(\mathrm{Rb})$. As shown in Refs. [6,7] for rubidium, we recalculate with updated values for $g(e)$ [28] and $g_J(\mathrm{Rb})/g(e)$ [37] to arrive at

$$g_J(6^2S_{1/2}) = 2.002\,540\,261(27). \tag{14}$$

This result is an order-of-magnitude improvement in accuracy compared to the value in Ref. [25]. This value is the current best estimate of the ground state g-factor.

From Refs. [25,26], the best measurement of the excited state Landé g-factor is

$$g_J(6^2P_{3/2}) = 1.334\,00(30), \tag{15}$$

as measured by Abele *et al.* in 1975 [38].

A theoretical value for the Landé g-factor, $g_J(6^2P_{3/2})$, is given by the RS coupling value, Eq. (4). This can be evaluated using either the free electron g-factor for g_S or, as suggested in Ref. [7], the ground state g-factor $g_J(6^2S_{1/2})$ in Eq. (14) since, according to Eq. (4), the two should be identical.

$$g_J(6^2P_{3/2})_{g_S=g(e)} = 1.334\,103\,68, \tag{16}$$

$$g_J(6^2P_{3/2})_{g_S=g_J(6^2S_{1/2})} = 1.334\,177\,33. \tag{17}$$

It should be noted that Eq. (15) is consistent with both Eq. (16) and (17).

Using Eqs. (14) and (15) in Eq. (10), we find

$$\gamma_1 = 13.9925(63)\ \mathrm{GHz/T}, \tag{18}$$

which is the current best value for γ_1.

A theoretical value for the quadratic shift is given by the HCCM value in Eq. (6). Using the effective principal quantum numbers n^* of Ref. [36], we obtain a quadratic shift ξ^{dia}/h of 0.3202 $\mathrm{MHz/T^2}$ for the ground state and 0.7602 $\mathrm{MHz/T^2}$ for the excited state, resulting in an expected diamagnetic shift coefficient of

$$\gamma_2 = 0.4400\ \mathrm{MHz/T^2}. \tag{19}$$

V. METHOD

A. Realizing saturated absorption spectroscopy inside an MRI scanner

In order to perform saturated absorption spectroscopy inside an MRI scanner, we have developed a nonmetallic fiber-coupled probe containing all the necessary optics shown in Fig. 3. The probe light is delivered to the probe in a single-mode polarization maintaining (PM) fiber and returned for detection through a multimode (MM) fiber. To keep the probe and the probed volume small, the optical path length in the cesium vapor cell is only 5 mm, so in order to increase absorption, the cell is heated with a high-power laser beam, delivered through a MM fiber. The fibers are 19 m long.

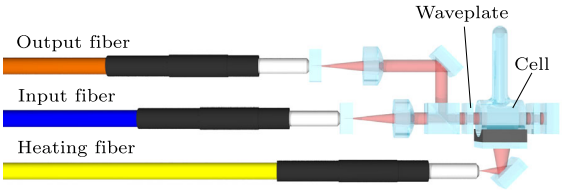

FIG. 3. Optics for performing saturated absorption spectroscopy. The probe light enters through the blue PM fiber and exits through the orange MM fiber. A high-power laser beam delivered through the yellow MM fiber heats the vapor cell. The angle of the quarter-wave plate defines the handedness of the circularly polarized probe light.

All optical elements of the probe are mounted in a $90 \times 33 \times 10\ \mathrm{mm^3}$ 3D printed nylon enclosure. A total of five probes have been assembled, as shown in Fig. 4. The quarter-wave plate can be turned 90° to shift the handedness of the circular polarization. For details on the probe design, see Appendix A.

The magnetic susceptibility of the components that make up the probes has been measured, and the associated magnetic field shift at the position of the probing laser beam inside the vapor cell is determined to be

$$\zeta = 1 + 0.92(50) \times 10^{-6}. \tag{20}$$

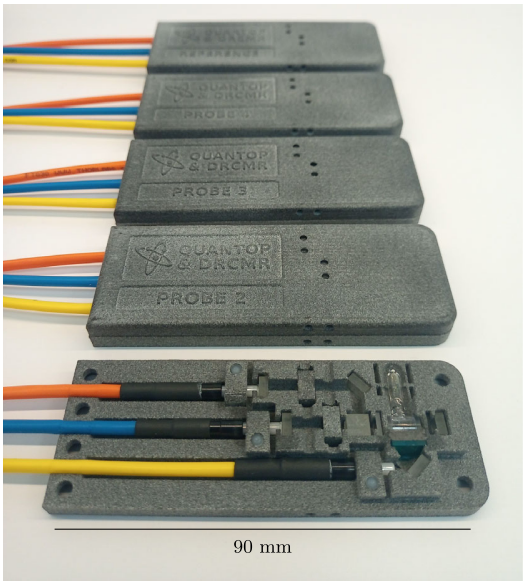

FIG. 4. Physical realization of the five probes. The cover is removed from probe 1 to show the optics inside.

For details on these measurements and calculations, see Appendix B.

B. Proton spectroscopy

We can accurately measure the magnetic field inside the MRI scanners (Philips Achieva 3 T and 7 T systems) by proton NMR spectroscopy. Using the hardware of the scanner, we excite hydrogen nuclei, in a spherical container of ultrapure water, with an rf pulse and read out the precession frequency ν_{p} inductively. The magnetic field can then be calculated as

$$B = \frac{\nu_{\mathrm{p}}}{\gamma'_{\mathrm{p}}(t)}, \tag{21}$$

where $\gamma'_{\mathrm{p}}(t)$ is the shielded proton gyromagnetic ratio corrected for a small dependence on the temperature t. For further details, see Appendix C. We find the field homogeneity to be on the level of 0.3 ppm over the relevant volume.

C. Sideband spectroscopy

Four of the probes are placed in the magnetic field in the center of the MRI scanner, and the fifth is placed in a magnetic shield far away from the MRI scanner. This zero-field reference probe is designed with the quarter-wave plate placed after (instead of before) the cell, such that the probe light polarization is linear. In this way, all the different $|4, m_F\rangle \leftrightarrow |5, m'_F\rangle$ transitions, which are degenerate at 0 T, contribute to the observed line, which will only broaden in a small residual magnetic field rather than shift. We call this line the 0 T transition, and it marks the frequency from where the shifts $\Delta\nu_{\pm}$ in Eq. (13) are measured. For the four probes inside the MRI scanner, the light is phase modulated by a high-power, high-frequency electro-optic modulator (EOM), generating multiple strong sidebands, below and above the carrier frequency. Two of the probes inside the magnetic field are configured with σ_+ polarization, and two are configured with σ_- polarization. Varying the EOM drive frequency, we can overlap saturated absorption resonances from carrier and sidebands when scanning the laser frequency and thus measure resonance frequency differences as multiples of the EOM drive frequency. The $\pm$5th sidebands are used at 7 T, and the $\pm$3rd sidebands are used at 3 T. This overlap method drastically reduces the sensitivity to nonlinearities of the laser frequency scan. In principle, only one σ_+ and one σ_- configured probe are needed inside the MRI scanner, but the redundancy with four probes enables powerful checks for systematic errors. We use a Toptica DL Pro, 852 nm external cavity diode laser (ECDL) as our probe light source; and a 20 GHz iXblue, high-power, lithium niobate phase modulator as our EOM. The setup is shown in Fig. 5. For further details on the resonance overlapping method, see Appendix D.

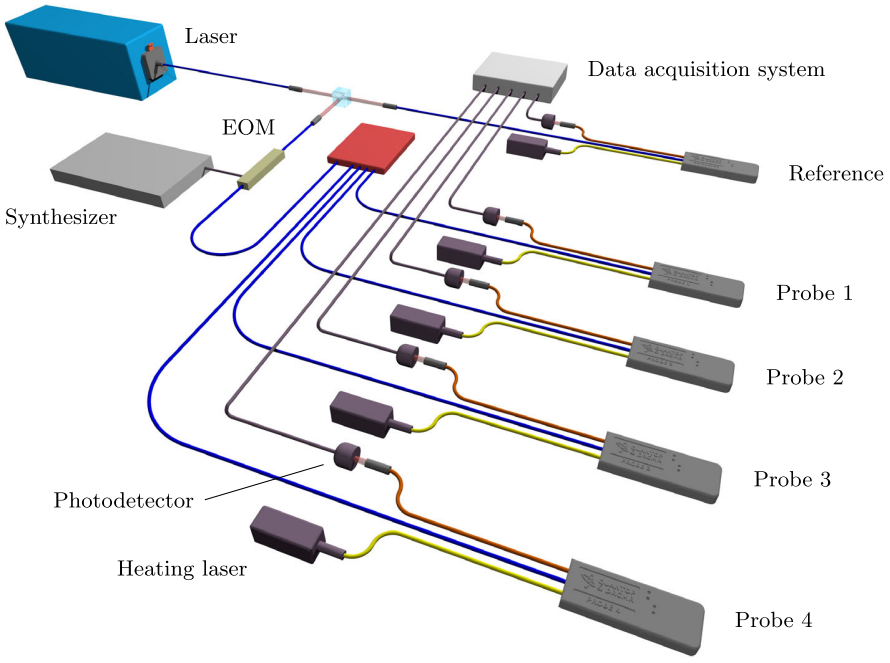

FIG. 5. Optical setup. A laser beam is split into two: One part is sent to the reference probe, which is put inside a magnetic shield. The other part is passed through an EOM, split into four, and sent to each of the four probes, which are located inside the MRI scanner.

D. Data acquisition procedure

A data series is acquired through the following steps:

(i) The water temperature t_a is noted, and proton NMR spectroscopy is performed on the spherical water sample to measure a precession frequency $\nu_{\mathrm{p},a}$.
(ii) The four probes are placed in the MRI scanner instead of the water sample.
(iii) The frequency difference between the extreme σ_+ transition and the extreme σ_- transition, $\Delta\nu_+ - \Delta\nu_-$, is measured by sideband spectroscopy.
(iv) The frequency difference between the extreme σ_+ transition and the 0 T transition, $\Delta\nu_+$, is measured.
(v) The frequency difference between the 0 T transition and the extreme σ_- transition, $-\Delta\nu_-$, is measured.
(vi) Finally, the water temperature t_b is noted, and the water sample is again placed in the MRI scanner, instead of the probes, to measure a precession frequency $\nu_{\mathrm{p},b}$.

The MRI scanner clock ν_c, which is also used as the reference clock for the synthesizer driving the EOM, is continuously monitored throughout the experiment and measured in absolute terms.

A full data acquisition run takes about 45 minutes. For details on how the probes are positioned inside the scanner, see Appendix A.

VI. RESULTS

With the probes positioned in the center of the 7 T MRI scanner, the reference at 0 T, and the EOM driven at $\nu_{\mathrm{EOM}} = 19\,592.24$ MHz, we see the three different spectra in Fig. 6. The 0 T spectrum, probed by the carrier frequency, shows the hyperfine structure of the D_2 line; and the two 7 T spectra, simultaneously probed by the ± 5th sidebands, with $\sigma_\pm$ polarization, show the eight transitions with ground state $m_J = \pm\frac{1}{2}$, excited state $m'_J = \pm\frac{3}{2}$, and $m_I = m'_I$ from $\pm\frac{7}{2}$ to $\mp\frac{7}{2}$, from left to right. The extreme $\sigma_\pm$ transitions are the leftmost ones, cf. Fig. 2. Notice how the extreme $\sigma_\pm$ transitions overlap well with this choice of ν_{EOM}, indicating that the difference $\Delta\nu_+ - \Delta\nu_-$ is about $10 \times \nu_{\mathrm{EOM}}$ since this is the frequency difference between the ± 5th sidebands. If no diamagnetic shift exists, these two transitions should also overlap with the 0 T transition probed by the carrier. This is clearly not the case, as they are seen to be about $0.44\ \mathrm{MHz/T^2} \times (7\ \mathrm{T})^2 = 22$ MHz higher, as predicted by Eq. (19). The laser frequency is scanned by varying the ECDL control parameters. The frequency axis is determined from knowledge of the 0 T D_2 line hyperfine structure, assuming a linear frequency scan.

To obtain an accurate, reproducible, unbiased measurement of the ν_{EOM} that best overlaps the resonances, and hence $\Delta\nu_+ - \Delta\nu_-$, ν_{EOM} is varied and line positions are fitted. The procedure, considered error sources, and associated uncertainty estimates are described in Appendixes D and E.

Six experimental runs are performed. The first two are performed at the 3 T scanner: First, probes 1 and 2 are configured with σ_- polarization, and probes 3 and 4 are configured with σ_+ polarization; second, the opposite configuration is used. Next, the same two configurations are used at the 7 T scanner. Finally, the vapor cells in probe 4 and the reference probe are interchanged, and the same two configurations are used again.

For each experimental run, a line of data is listed in Table II. The data, tabulated chronologically, are acquired from April 17 to May 22, 2022.

A. Calculating the linear magnetic frequency shift

By measuring the frequency difference $\Delta\nu_+ - \Delta\nu_-$, we can eliminate the measurement offset and the quadratic contribution in Eq. (13) to find

$$\Delta\nu_+ - \Delta\nu_- = 2\gamma_1\zeta B. \tag{22}$$

Isolating γ_1 and using Eq. (21), we find

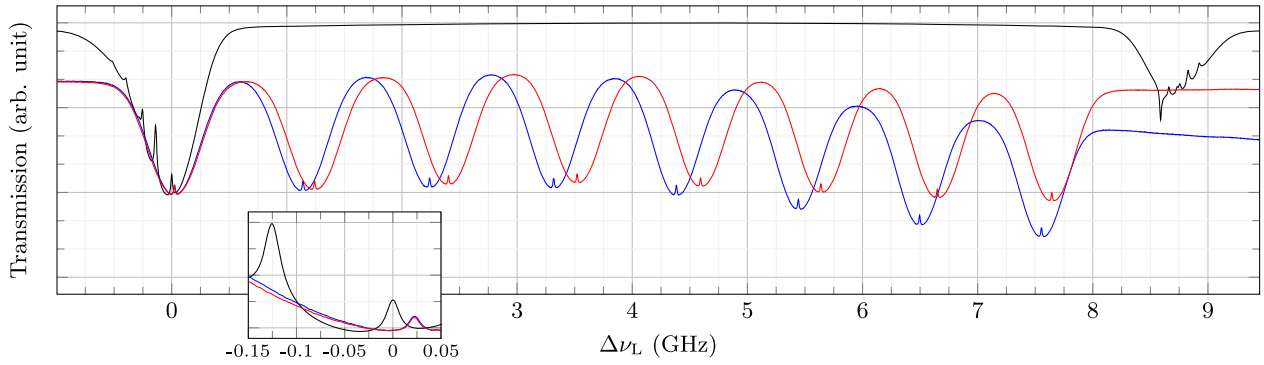

FIG. 6. Scan of the laser frequency over the 0 T spectrum (black line) and the two 7 T spectra as probed by the ± 5th sidebands for $\nu_{\mathrm{EOM}} = 19\,592.24$ MHz (the blue line is the σ_+ polarization, and the red line is the σ_- polarization). The laser frequency is shown as a difference $\Delta\nu_L$ from the 0 T transition. Narrow saturation peaks are seen on top of the Doppler broadened lines. The offset between the 0 T transition at 0 GHz and the overlapping extreme $\sigma_\pm$ transitions visible in the inset is due to a diamagnetic shift of about 22 MHz.

TABLE II. Data points underlying the analysis in this work. The configuration refers to the $\sigma_\pm$ polarization of probes 1, 2, 3, and 4, respectively. The asterisk indicates that the cells in probe 4 and the reference have been interchanged. The temperature t is measured next to the water sample just prior to the proton spectroscopy. The proton precession frequency ν_p is determined by NMR spectroscopy. Subscripts a and b refer to measurements before and after the optical measurements, respectively. The optical frequency differences are determined by the overlapping method described in Appendix D. The "10 MHz" MRI scanner clock frequency ν_c, also used as the reference clock for the synthesizer driving the EOM, is measured for each data series.

B	Configuration	t_a (°C)	t_b (°C)	$\nu_{p,a}$ (Hz)	$\nu_{p,b}$ (Hz)	$\Delta\nu_+ - \Delta\nu_-$ (MHz)	$\Delta\nu_+$ (MHz)	$-\Delta\nu_-$ (MHz)	ν_c (Hz)
3 T	$--++$	20.3(5)	20.5(5)	127 778 093(36)	127 778 102(38)	83 998.043(88)	42 003.342(88)	41 994.668(88)	9 999 991(5)
3 T	$++--$	20.0(5)	20.1(5)	127 777 873(32)	127 777 902(41)	83 997.954(88)	42 003.311(88)	41 994.620(88)	9 999 990(5)
7 T	$++--$	20.0(5)	20.0(5)	298 037 732(60)	298 037 734(61)	195 922.431(88)	97 984.127(88)	97 938.342(88)	9 999 992(2)
7 T	$--++$	20.0(5)	20.0(5)	298 037 724(42)	298 037 723(65)	195 922.346(88)	97 984.094(88)	97 938.225(88)	9 999 992(2)
7 T	$--++^*$	20.0(5)	19.9(5)	298 037 732(74)	298 037 732(72)	195 922.303(88)	97 984.058(88)	97 938.256(88)	9 999 992(2)
7 T	$++--^*$	19.4(5)	19.4(5)	298 037 716(62)	298 037 720(61)	195 922.427(88)	97 984.168(88)	97 938.313(88)	9 999 992(2)

$$\gamma_1 = \frac{\Delta\nu_+ - \Delta\nu_-}{2\zeta B} = \frac{(\Delta\nu_+ - \Delta\nu_-)\cdot\gamma_p'(t)}{2\zeta\nu_p}. \tag{23}$$

Notice that this expression contains the ratio of two frequency measurements: the proton precession frequency and the optical frequency difference. This means that it is not sensitive to the absolute accuracy of these frequencies, as long as a single common clock is used, as is the case for our experiment.

For each line in Table II, two values for γ_1 are calculated: one based on the single direct measurement of the optical frequency difference $\Delta\nu_+ - \Delta\nu_-$, and one based on the sum of the two measurements $\Delta\nu_+$ and $-\Delta\nu_-$. The proton precession frequency for each line is taken to be the average of the measurement before and after, with the uncertainty taken to be the difference, plus the two individual uncertainties, and similarly for the temperature, except that we only include the thermometer uncertainty of 0.5 °C once. The resulting values are displayed in Table III, along with the MRI scanner magnetic field and the probe polarization configuration. We find the mean of these values to be

$$\gamma_1 = 13.994\,301(11)\ \text{GHz/T}. \tag{24}$$

TABLE III. Different determinations of γ_1. The values in the third column are calculated using the single measurement $\Delta\nu_+ - \Delta\nu_-$. The values in the fourth column are calculated using the sum of the measurements $\Delta\nu_+$ and $-\Delta\nu_-$.

B	Configuration	γ_1 (GHz/T) (single)	γ_1 (GHz/T) (sum)
3 T	$--++$	13.994 299(19)	13.994 294(24)
3 T	$++--$	13.994 308(20)	13.994 304(25)
7 T	$++--$	13.994 304(11)	13.994 307(13)
7 T	$--++$	13.994 299(11)	13.994 297(12)
7 T	$--++^*$	13.994 295(12)	13.994 296(13)
7 T	$++--^*$	13.994 305(11)	13.994 309(13)

For the uncertainty, we simply take the lowest of the uncertainties from Table III, recognizing that part of the uncertainty comes from the probe field shift ζ and is common to all the measurements, and other systematic error sources might also be at work. The value in Eq. (24) represents an improvement in accuracy of more than 2 orders of magnitude compared to Eq. (18). The data in Table III are shown in Fig. 7. All reported uncertainties in this work should be interpreted as 1 standard deviation.

B. Calculating the Landé g-factor for the excited state

Isolating $g_J(6^2P_{3/2})$ in Eq. (10) and using the result in Eq. (24), we find

$$g_J(6^2P_{3/2}) = \gamma_1\cdot\frac{2h}{3\mu_B} + \frac{g_J(6^2S_{1/2})}{3} = 1.334\,087\,49(52), \tag{25}$$

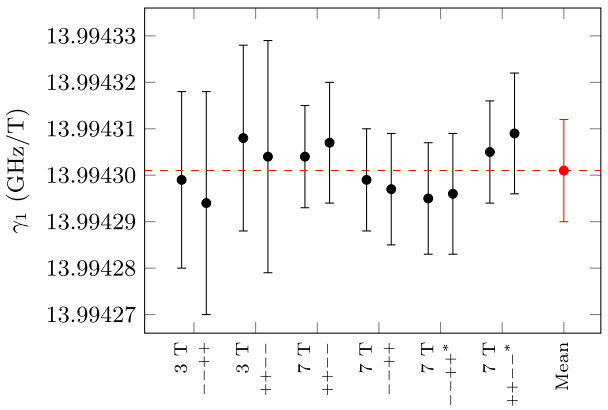

FIG. 7. Values for γ_1 from Table III (black), along with the mean value (red). Error bars, which include estimates of systematic errors, are obtained as described in the text and should be interpreted as 1 standard deviation.

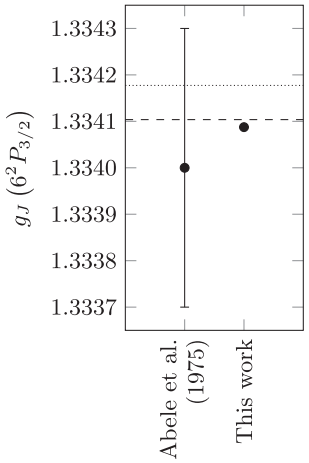

FIG. 8. Comparison of our result, Eq. (25), with the best previous measurement [38], and the two RS values. The dashed line represents the RS value calculated using the free electron g-factor as g_S, Eq. (16). The dotted line represents the RS value calculated using the ground state g-factor as g_S, Eq. (17). The uncertainty on our result is too small to be shown as an error bar in this plot. The error bar on the result from Ref. [38] is described as including "possible systematic errors as well as three times the standard deviation."

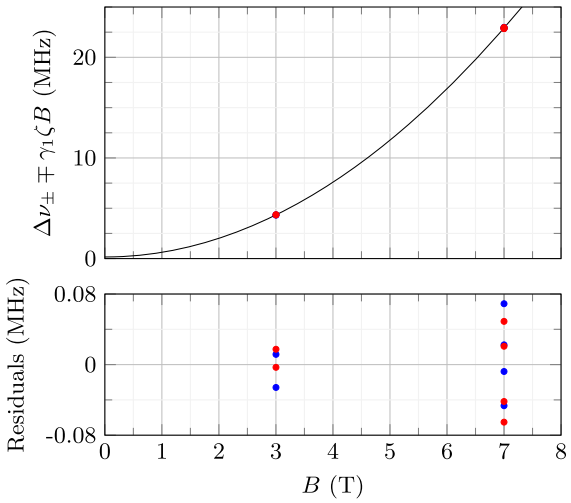

FIG. 9. Data $\Delta\nu_\pm \mp \gamma_1\zeta B$, fit $\gamma_0 + \gamma_2\zeta^2B^2$, and residuals. Blue data are from the σ_+ configured probes, and red data are from the σ_- configured probes. The least-squares fit produces the values $\gamma_0 = 0.159$ MHz and $\gamma_2 = 0.4644$ MHz/T^2. This method is only used to estimate γ_0 and not γ_2 since it does not provide a good estimate for the uncertainty.

which can be compared to the previous best value, Eq. (15), measured by Abele *et al.* (1975) [38], and the RS values, Eqs. (16) and (17), in Fig. 8. As with the γ_1 measurement, we see an improvement in accuracy of more than 2 orders of magnitude. The RS value calculated using the free electron g-factor as g_S, Eq. (16), is the prediction closest to our result. However, the discrepancy is 31 standard deviations and hence substantial.

C. Determining the frequency shift measurement offset

To determine the measurement offset γ_0, we reorganize Eq. (13) to read

$$\Delta\nu_\pm \mp \gamma_1\zeta B = \gamma_0 + \gamma_2\zeta^2B^2. \tag{26}$$

For each line in Table II, a magnetic field B is calculated using Eq. (21), and the left-hand side is calculated for the values $\Delta\nu_\pm$ using the result in Eq. (24) for γ_1. This data set is fitted, without taking uncertainties into account, with the quadratic right-hand side, as shown in Fig. 9, to produce the value

$$\gamma_0 = 0.159(159)\ \text{MHz}. \tag{27}$$

Since this number should be zero and we do not know exactly the cause of this deviation, we take the uncertainty to be 100%, even though the largest residual from the fit is 0.069 MHz. We note that this measurement offset is small compared to the linewidth of the transition, as expected. Here, the clock inaccuracy, listed in Table II as ν_c, is taken into account but is found to be negligible.

It should be stressed that γ_0 is an experimental offset that depends on the physical implementation of the measurement. We report it here since it gives a good estimate of the accuracy of the method and because we need it for the calculations in the next section.

D. Calculating the quadratic diamagnetic shift

By measuring, and adding, the optical frequency shifts $\Delta\nu_+$ and $\Delta\nu_-$, we can eliminate the linear part in Eq. (13) to obtain

$$\Delta\nu_+ + \Delta\nu_- = 2\gamma_0 + 2\gamma_2\zeta^2B^2. \tag{28}$$

Isolating γ_2 and using Eq. (21), we find

TABLE IV. Different determinations of γ_2. Also shown are the values γ_2^{d}, directly calculated without taking the measurement offset γ_0 into account.

B	Configuration	γ_2 (MHz/T^2)	γ_2^{d} (MHz/T^2)
3 T	$--++$	0.4639(190)	0.4815(69)
3 T	$++--$	0.4648(190)	0.4825(69)
7 T	$++--$	0.4639(35)	0.4672(13)
7 T	$--++$	0.4648(35)	0.4680(13)
7 T	$--++^*$	0.4641(35)	0.4674(13)
7 T	$++--^*$	0.4647(35)	0.4679(13)

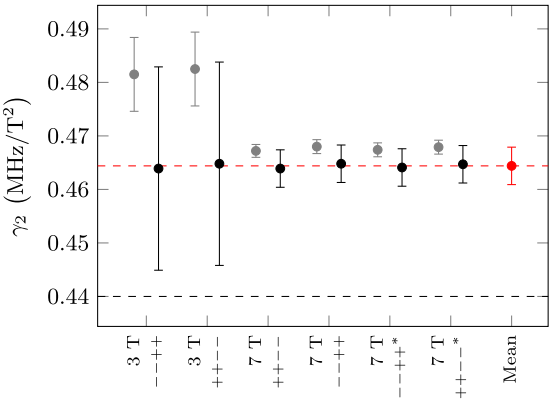

FIG. 10. Values for γ_2 from Table IV (black), along with the mean value (red). The direct calculations γ_2^{d}, not taking the experimental offset γ_0 into account, are shown in gray. The dashed black line shows the HCCM value from Eq. (19). Error bars, which include estimates of systematic errors, are obtained as described in the text and should be interpreted as 1 standard deviation.

$$\gamma_2 = \frac{\Delta\nu_+ + \Delta\nu_- - 2\gamma_0}{2\zeta^2 B^2} = \frac{(\Delta\nu_+ + \Delta\nu_- - 2\gamma_0)\cdot(\gamma_{\mathrm{p}}'(t))^2}{2\zeta^2\nu_{\mathrm{p}}^2}. \tag{29}$$

Notice that this expression *is* sensitive to the absolute accuracy of the clock, unlike Eq. (23). The (in this case, insignificant) frequency correction is made by multiplying the denominator by a factor $\nu_{\mathrm{c}} \times (10\ \mathrm{MHz})^{-1}$.

For each line in Table II, a value for γ_2 is calculated. The resulting values are displayed in Table IV, along with the MRI scanner magnetic field and the probe polarization configuration. We find the mean of these values to be

$$\gamma_2 = 0.4644(35)\ \mathrm{MHz/T^2}. \tag{30}$$

For the uncertainty, we simply take the lowest of the uncertainties from Table IV, as in Eq. (24). Also shown in Table IV are values γ_2^{d} directly calculated, without taking the measurement offset γ_0 into account. The data in Table IV are shown in Fig. 10. Since these are the first such measurements, we do not have any other experimental data to compare them to. We notice that the mean value in Eq. (30) is on the same order of magnitude as the HCCM value found in Eq. (19) (also shown in Fig. 10), however, with a significant discrepancy of 7 standard deviations.

VII. CONCLUSION

In this work, we have investigated the cesium D_2 transitions involving the extreme angular-momentum states. The magnetic field dependence of these transitions has been mapped with unprecedented accuracy compared to any other alkali optical transition, enabling accurate optical magnetometry at high magnetic fields.

It is very interesting to note that the excited state g-factor calculated in Eq. (25) is not in agreement with the RS coupling value of Eq. (16), as we find a discrepancy of -1.6×10^{-5}, significant to 31 standard deviations. According to Ref. [29], until now, all measurements on alkali non-S states have been in agreement with the RS value. For D states in cesium, discrepancies up to -5.5×10^{-5} are predicted theoretically using more advanced methods [39]. No theoretical predictions have been published yet for the P states.

It is also very interesting to note that the quadratic diamagnetic shift is not in agreement with the HCCM value. Most of the data presented in Ref. [35] show very good agreement with the HCCM value; only for potassium are discrepancies of up to 2.7 standard deviations reported. Here, we report a highly significant discrepancy of 7 standard deviations.

These results could motivate theoretical work on high-accuracy calculations beyond the RS coupling scheme and the HCCM assumption.

VIII. OUTLOOK

It should be noted that similar measurements can be made for other transitions and other alkali atoms. This could enable high-accuracy magnetometry with other laser wavelengths or other alkali atoms, and provide more data for testing of atomic structure models. In future studies, possibly involving many different magnetic fields, the possibility of the simple model described by Eq. (13) being insufficient should also be considered. This may become relevant for very accurate measurements or very high fields. For a discussion of possible future improvements to this kind of experiment, see Appendix F.

We are currently working to develop the system presented in this work into a fully functional high-speed magnetometer by implementing continuous tracking of the magnetic frequency shift $\Delta\nu_+$ in Eq. (13). Such a magnetometer could have applications in MRI, as described in Ref. [41], as well as other areas where high magnetic fields need to be stabilized or monitored. For a discussion on measurement strategies, see Appendix G.

The data sets and scripts for the analysis and calculations underlying this work are openly available from Ref. [40].

ACKNOWLEDGMENTS

We would like to thank Michael Zugenmaier for useful suggestions on the probe design, Axel Boisen for designing and building the heating lasers, Jan Ole Pedersen for assisting with the MRI systems, and Lars G. Hanson and Ennio Arimondo for helpful discussions. This project has received funding from the Danish Quantum Innovation

Center (Qubiz)/Innovation Fund Denmark, the European Union's Horizon 2020 research and innovation programme under Grant Agreements No. 820393 and No. 787520, and Villum Fonden under a Villum Investigator Grant, Grant No. 25880. The 7 T scanner was donated by the John and Birthe Meyer Foundation and The Danish Agency for Science, Technology and Innovation (Grant No. 0601-01370B).

APPENDIX A: PROBE DESIGN

The MRI-compatible fiber-coupled probe design is shown in Fig. 11. After the 852 nm probe light emerges from the blue PM fiber, with an angle of 4.9°, the beam is collimated by a lens, with a focal length $f = 10$ mm, to have a waist of 0.86 mm. After passing through the polarizing beam splitter (PBS), the quarter-wave plate, and the vapor cell, the beam is cut by an aperture of 2 mm diameter. This means that the measurement volume of the probe is bounded by a cylinder of 2 mm diameter and 5 mm length. The return beam intensity is attenuated to 16% by passing an optical filter twice to avoid excessive power broadening of the saturated absorption signal. Another $f = 10$ mm lens focuses the beam into a MM fiber with a core diameter of 0.4 mm. The 808 nm heating laser light is delivered through a similar MM fiber. The heating laser beam is absorbed in an optical filter, and a silicone heat conductor transfers the heat to the vapor cell, allowing for very localized heating. With the stem of the vapor cell pointing away from the point of heating, it is ensured that the coldest point of the cell is far away from the probing beam path, such that cesium does not condense on the windows and block the probe beam. The two probe-beam input and output fibers are terminated by windows with antireflection (AR) coating on the side facing away from the fibers to reduce spurious etalon fringes from the fibers in the spectrum. Index matching gel is applied at the interface between the fiber tips and the windows. The fibers are 19 m long. Mirrors, windows, and PBS are fastened with glue. The lenses are glued into cubic holders, which are mounted by a tight fit in their slots.

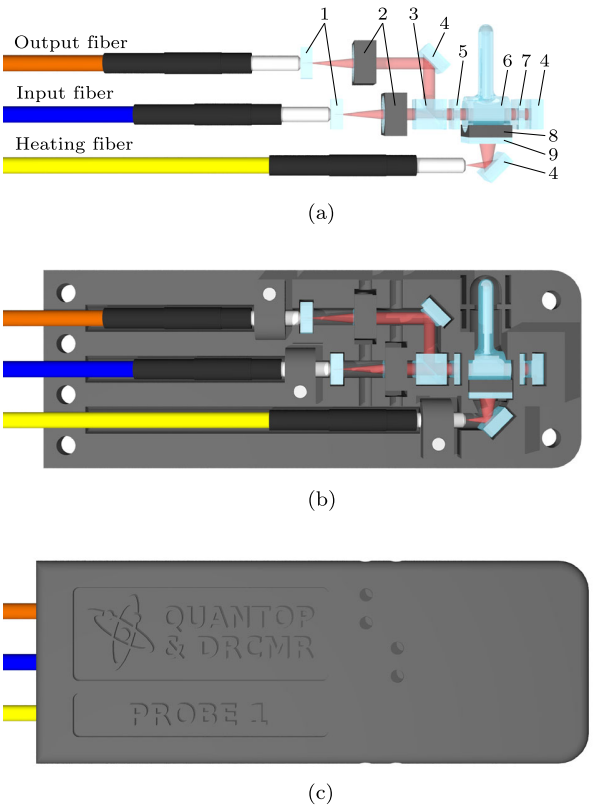

FIG. 11. Optical elements of the probe and how they are mounted inside the nylon holder. (a) 1: AR coated windows. 2: Lenses glued into cubic nylon holders. 3: PBS. 4: Mirrors. 5: Quarter-wave plate. 6: Vapor cell. 7: Optical filter with 40% transmission at 852 nm. 8: Heat conducting silicone. 9: Optical filter with 1.2% transmission at 808 nm. (b) The whole setup is put in a nylon holder. Mirrors, PBS, and windows are glued in. The fibers are clamped by the ceramic ferrules, with nylon bolts from below. Lens holders are fitted tightly into theirs slots. (c) A protective cover is fastened on top of the holder with nylon bolts from the bottom. Lens positions can be adjusted by pushing through the holes from the outside.

The nylon enclosure measures $90 \times 33 \times 10$ mm^3 and is 3D printed using HP Multi Jet Fusion (MJF) technology. While stereolithographic (SLA) 3D printing produces very nice results, as demonstrated in Ref. [42], the material is not compatible with temperatures approaching 100 °C, like nylon, which is why the MJF method is used here.

By pushing through holes from the outside, the lens positions can be adjusted to optimize the beam direction and output fiber coupling. We achieve a fiber coupling close to 100%, reasonably stable during daily handling.

During the experiments described in this work, the four probes are strapped together by two thin sewing threads, in a configuration with probes 2 and 4 on top of probes 1 and 3, as shown in Fig. 12. When the spherical water sample is removed from the MRI scanner during a data acquisition

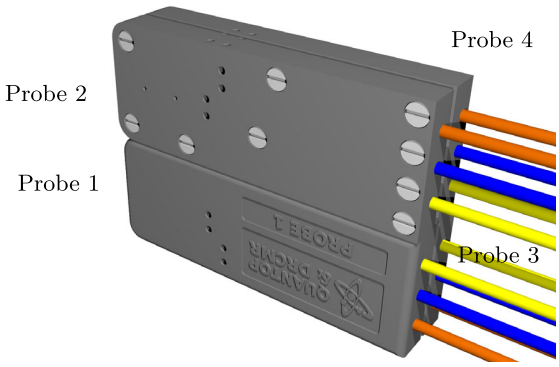

FIG. 12. The four probes in the configuration used inside the scanner. The probes are held together by two thin sewing threads (not shown in the image). The field direction is parallel to the fibers.

run, the probes are positioned, as well as possible, at the center of where the sample used to be, pointing along the field direction, suspended from a thin sewing thread. The sewing threads are assumed to have a negligible effect on the magnetic field.

It should be noted that small angular misalignments of the probes and imperfect polarizing optics will only lead to small reductions in the signal—not frequency shifts—since the frequency shifts are only sensitive to the magnitude of the magnetic field.

Probes 1 and 3 are heated with 600 mW of optical power, and probes 2 and 4 are heated with 500 mW. The reference probe is heated with 250 mW. After about an hour, the probe temperatures stabilize around 43 °C, and the reference temperature stabilizes around 35 °C. This corresponds to a cesium atomic density of about 26×10^{16} m^{-3} for the probes and 13×10^{16} m^{-3} for the reference. Compared to about 3×10^{16} m^{-3} at room temperature, this gives a significant increase in absorption depth and hence signal strength.

About 542 μW of optical probe power is sent to the probes, and about 175 μW is sent to the reference. Notice that for the probes, only a smaller fraction of the probe light is actually resonant, as the sidebands generated by the EOM are the ones used. At 3 T, third sidebands are used, and at 7 T, fifth sidebands are used. This means that only about 19% and 14% of the probe light is on resonance, respectively.

APPENDIX B: MAGNETIC FIELD SHIFT OF THE PROBES

The shielded proton gyromagnetic ratio is defined such that the field that is measured is the one in the vacuum left when the spherical water sample is removed. When the sphere is removed and replaced with the four probes and air, the magnetic field is changed slightly due to the change in magnetic susceptibility. This is taken into account by the factor ζ introduced in Eq. (13). We have measured the volume magnetic susceptibility χ for all the components of the probes using a method similar to that described in Ref. [43]: A sample of the component material is submerged in water, and the field distortion around the sample is mapped using the 7 T MRI scanner. From a fit, the difference in sample and water magnetic susceptibilities, $\chi - \chi_{H_2O}$, is determined. The sample magnetic susceptibility is then found using $\chi_{H_2O} = -9.0559(61)$ ppm [44]. For components easily isolated, the results are shown in Table V. We note that the values for $\chi - \chi_{H_2O}$ found for Schott Borofloat 33 and Schott N-BK7 agree with the values from Ref. [43] within about 5%. Hence, this is chosen as the level of uncertainty, implying that magnetic susceptibilities close to χ_{H_2O} are measured much more accurately than those far away. Notice how the optical filters are highly paramagnetic, especially the probe beam filter.

For the fiber cables (i.e., the outer jacket of the cable and everything inside it, including air) and the fittings (which keep the fiber cables and the fiber ferrules together), "effective" magnetic susceptibilities are determined for the compound components. The results are shown in Table VI. Since this is measured without disassembling the fiber cables, the method is less accurate. We find the uncertainty to be 25% by comparing the measurement on the zirconia ferrules in the assembled fiber cables to the measurement on pure zirconia. Detailed knowledge of these components is fortunately not important for the field shift at the position of the vapor cell.

For the vapor cell, a model is constructed using the value for quartz glass from Ref. [43] [$\chi = -11.30(1)$ ppm] and vacuum ($\chi = 0$). The field shift of this model is seen to match reasonably well with the measured field shift from a vapor cell. Our vapor cells are made from Momentive GE214 Fused Quartz (body) and Corning 7980 Fused Silica (windows) by Precision Glass Blowing.

The magnetic susceptibility of the surrounding air is taken to be $\chi_{Air} = 0.36$ ppm, as in Ref. [45].

The magnetic susceptibility of cesium is calculated from the data in Ref. [46] to be 5.1 ppm. Hence, the very small amounts of cesium sitting in the bottom of the vapor cell stem can safely be ignored. Similarly, the glue used to hold

TABLE V. Volume magnetic susceptibility measurements on parts consisting of only a single material. The method is estimated to be accurate to about 5% for the value of $\chi - \chi_{H_2O}$.

Material	Component	$\chi - \chi_{H_2O}$ (ppm)	χ (ppm)
Unknown	Heating beam filter	18.47(92)	9.41(92)
MJF Nylon PA12	3D print	0.1209(60)	−8.9350(86)
Nylon 66 UL94V-2	Bolts	−0.213(11)	−9.269(13)
Synthetic quartz	Quarter-wave plate	−4.34(22)	−13.39(22)
Schott Borofloat 33	Mirrors and windows	−2.13(11)	−11.19(11)
Schott N-BK7	Lenses	−3.31(17)	−12.37(17)
Schott N-SF1	PBS	−0.524(26)	−9.580(27)
Schott NG4	Probe beam filter	149.3(75)	140.2(75)
Silicone, RS 174-5694	Heat conductor	−1.273(64)	−10.329(64)
Zirconia	Fiber ferrules	−1.053(53)	−10.109(53)

TABLE VI. Volume magnetic susceptibility measurements on compound parts not easily separated in single materials. The method is estimated to be accurate to about 25% for the value of $\chi - \chi_{H_2O}$.

Component	$\chi - \chi_{H_2O}$ (ppm)	χ (ppm)
Fiber cable (heat)	1.38(34)	−7.68(34)
Fiber cable (in)	2.45(61)	−6.61(61)
Fiber cable (out)	1.12(28)	−7.93(28)
Fitting (heat)	4.6(12)	−4.4(12)
Fitting (in)	2.21(55)	−6.84(55)
Fitting (out)	4.6(11)	−4.5(11)

the optical elements in place, the index matching gel, and the thin optical coatings are assumed to be negligible.

Using all the above, a 3D susceptibility model of the probe is constructed, as seen in Fig. 13. Using the method described in Refs. [47,48], we then calculate the field shift caused by this distribution of magnetic susceptibility. This method takes into account the effect of the Lorentz sphere, i.e., the effect of the granular structure of matter [49,50]. Since we are concerned with the field shift in the vacuum inside the vapor cell, we find the "continuous-matter field shift" by adding $\frac{2}{3}\chi$ to the calculated field shift. Since the calculation is performed on the susceptibility relative to the surrounding air, we also add $\frac{2}{3}\chi_{Air}$ to account for the sphere of air that replaces the sphere of water. The resulting field shift map is shown in Fig. 14. It should be noted that including the Lorentz sphere also works since, in this case, there is no field shift from the sphere of air that surrounds the probe.

FIG. 13. Cross section of the 3D susceptibility model of the probe. The cross section is made through the center of the vapor cell. We cap the color scale at 20 ppm, even though the probe filter susceptibility is 140 ppm, to highlight the details of the entire structure.

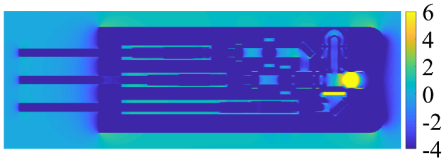

FIG. 14. Calculated field-shift map. The cross section is the same as in Fig. 13. The effect of the rest of the fibers, not included in this model, is verified through a similar simulation to have a negligible effect at the position of the vapor cell. We cap the color scale to match the distribution inside the vapor cell.

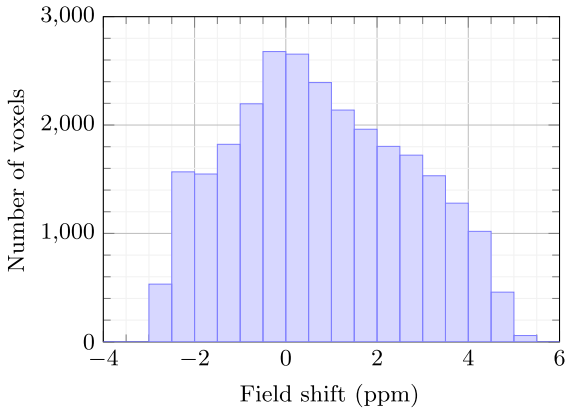

FIG. 15. Distribution of voxels in the beam path inside the vapor cell according to the simulated field shift. Notice how the highly paramagnetic optical filter next to the vapor cell creates a magnetic field gradient along the beam path.

Picking out the voxels that make up the probe beam path inside the vapor cell, we find a distribution of field shifts as seen in Fig. 15. By varying the voxel size, the surrounding zero padding, the magnetic susceptibilities of components close to the vapor cell, and the exact position of the highly paramagnetic probe filter, we find the mean value for the field shift in the beam path inside the vapor cell to be $1 + 0.49(50) \times 10^{-6}$. The uncertainty on this number also takes into account the variation over the radius of the beam since it is not clear if the center or the edge of the beam contributes the most to the measured signal. The main contribution to the uncertainty is related to the uncertainty on the probe filter susceptibility and its exact position. A similar calculation is performed on a model of all four probes strapped together, as seen in Fig. 12, to give

$$\zeta = 1 + 0.92(50) \times 10^{-6}. \tag{B1}$$

APPENDIX C: MAGNETIC FIELD DETERMINATION BY PROTON NMR SPECTROSCOPY

Accurate magnetic field determinations in the tesla range, uses that the shielded proton gyromagnetic ratio is known with very high accuracy [16,28,44] as

$$\gamma'_p(25\,°C) = 42.576\,384\,74(46)\ \text{MHz/T}. \tag{C1}$$

This value refers to hydrogen nuclei (protons) in a spherical sample of pure water at 25 °C. The water shielding factor depends slightly on the temperature t [44,51] as

$$\frac{\gamma'_p(t)}{\gamma'_p(25\,°C)} = 1\text{–}10.36(30) \times 10^{-9}\,°C^{-1}(t - 25\,°C). \tag{C2}$$

TABLE VII. Downmixing ν_0 and peak frequencies ν_m for the six data acquisition runs. Subscripts a and b refer to measurements before and after the optical measurements, respectively.

B	Configuration	ν_0 (Hz)	$\nu_{m,a}$ (Hz)	$\nu_{m,b}$ (Hz)
3 T	$--++$	127 778 089	4(36)	13(38)
3 T	$++--$	127 777 868	5(32)	34(41)
7 T	$++--$	298 037 729	3(60)	5(61)
7 T	$--++$	298 037 737	−13(42)	−14(65)
7 T	$--++^*$	298 037 744	−12(74)	−12(72)
7 T	$++--^*$	298 037 724	−8(62)	−4(61)

Using nuclear rf excitation and subsequent readout of the free induction decay (FID), the proton precession frequency ν_p is measured. The magnetic field can then be found as

$$B = \frac{\nu_p}{\gamma'_p(t)}. \tag{C3}$$

The magnetic field B is defined as the field in the vacuum left when the sphere of water is removed. Notice that the material of the container is not important as the field shift inside a spherical shell is zero [52].

For our case, where we use an MRI scanner, the acquired rf signal is first downmixed by a frequency ν_0, chosen by the scanner, close to the actual resonance frequency. The measured frequency of the FID is then ν_m, such that $\nu_p = \nu_0 + \nu_m$. We find ν_m as the peak value of the Fourier transform of the downmixed FID signal. The uncertainty is estimated by inspection of a field image of the spherical water sample produced by the scanner. For the 3 T scanner, the full width at 25% of the peak value is found to be a good estimate for the uncertainty. For the 7 T scanner, the full width at 5% of the peak value is used. For the six data acquisition runs, we note ν_0 and ν_m in Table VII. The proton precession frequencies in Table II follow. Notice that imperfections in the spherical shape—such as container deformations, residual air bubbles, and the small hole used for water filling—are taken into account by this uncertainty estimation. The sphere has a diameter of 100 mm and hence covers a much larger volume than the four vapor cells.

APPENDIX D: MEASURING OPTICAL FREQUENCY DIFFERENCES

Central to this work is the method to accurately measure a resonance frequency difference by sideband spectroscopy. By choosing an EOM modulation frequency ν_{EOM} equal to an integer fraction of the resonance frequency difference, the saturated absorption peaks as probed by the carrier or sidebands, can be brought to overlap. To do this in a systematic and unbiased way, a series of different frequencies, ν_{EOM}, are tried. In steps of 0.01 MHz, a range of 0.20 MHz is covered. For each ν_{EOM}, 100 laser frequency scans are averaged. As an example, we take the determination of the difference $\Delta\nu_+ - \Delta\nu_-$ in the last line in Table II, i.e., in the 7 T scanner, with probes 1 and 2 configured with σ_+ polarization and probes 3 and 4 with σ_- polarization. In Fig. 16, we show a laser frequency scan (average of 100) with $\nu_{EOM} = 19\,592.14$ MHz, such that the ± 5th sidebands probe the extreme $\sigma_\pm$ transitions. A fit of a second-degree polynomial background and a Lorentzian line shape is performed for each probe. The frequency axis is estimated in a prior scan across the 0 T spectrum from the reference probe. The exact scaling is not important. Changing ν_{EOM} in steps of 0.01 MHz up to 19 592.34 MHz, we obtain a series of fitted relative line centers as a function of $10 \times \nu_{EOM}$, as shown in Fig. 17. Straight lines are fit to the data, and the four intersections are found. The optical frequency difference is then found as their average to be $\Delta\nu_+ - \Delta\nu_- = 195\,922.427$ MHz. Similarly, the difference $\Delta\nu_+$ is found by sweeping ν_{EOM} across the frequency that overlaps the extreme σ_+ transition as probed by the fifth upper sideband, with the 0 T transition, as probed by the carrier. Here, only two intersections are found since there is only one reference probe. Finally, $-\Delta\nu_-$ is found by overlapping the extreme σ_- transition, as probed by the fifth lower sideband, with the 0 T transition, as probed by the carrier. In these two cases, the frequency difference is found as $5 \times \nu_{EOM}$. For the 3 T measurements, ± 3rd sidebands are used with EOM frequencies of about 14 GHz, and hence frequency differences are found as $6 \times \nu_{EOM}$ and $3 \times \nu_{EOM}$, correspondingly.

To estimate the uncertainty on the overlapping procedure, we note that the first measurement, $\Delta\nu_+ - \Delta\nu_-$, should equal the sum of the measurements $\Delta\nu_+$ and $-\Delta\nu_-$, so the difference between those two numbers represents an

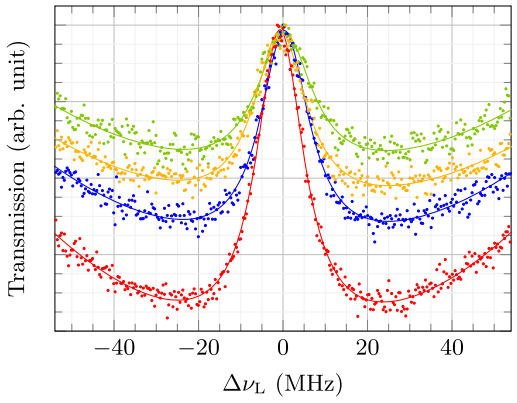

FIG. 16. Average of 100 laser frequency scans with $\nu_{EOM} = 19\,592.14$ MHz. The fifth upper sideband probes the extreme σ_+ transition in probes 1 and 2 (blue and green), and the fifth lower sideband probes the extreme σ_- transition in probes 3 and 4 (yellow and red).

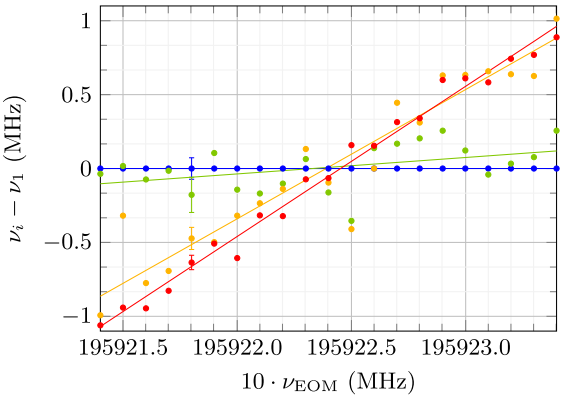

FIG. 17. Line center ν_i for probes $i = \{1, 2, 3, 4\}$ relative to ν_1 as a function of $10 \times \nu_{\mathrm{EOM}}$. Colors are as in Fig. 16. The leftmost data points correspond to the line centers found from the fits in Fig. 16. Error bars are found as 68% confidence intervals, i.e., 1 standard deviation, as detailed in Ref. [53]. To keep the figure clear and readable, error bars are shown only for a single representative line of data.

uncertainty on the overlapping procedure. We find the root mean square of the differences to be 0.034 MHz.

Apart from the overlapping procedure, there is also an uncertainty on how well the fitted line-shape center represents the actual resonance frequency. In particular, a significant "geometrical shift" has been observed, clearly correlating with the geometrical broadening (see, e.g., Ref. [54]) associated with the lenses not being well positioned such that the beam is not reflected exactly 180° backwards through the vapor cell. All lenses are adjusted as well as possible to reduce the geometrical broadening and shift. Configuring all the probes with σ_+ polarization, we see a variation of up to 0.054 MHz between the probes. Any shift common among probes 1–4 but differing from the reference probe is described by the constant γ_0 in Eq. (13).

We add the two above-described error sources to get 0.088 MHz, which is the uncertainty used for the optical frequency differences in Table II. Other considered error sources are discussed in Appendix E.

APPENDIX E: OPTICAL-RESONANCE-SHIFTING ERROR SOURCES

A number of error sources potentially contributing to a systematic shift of the optical resonance frequencies have been considered in this work. Most notably is the geometrical shift associated with lens positions and the related geometrical broadening of the line at 3 T and 7 T. We have not observed a similar shift at 0 T, making this a good candidate for explaining the measurement offset γ_0. With poor lens adjustment, we have observed linewidths up to 30 MHz and line-center shifts up to 0.4 MHz. By proper lens adjustment, linewidths of about 16 MHz are achieved. Apart from power broadening, this may also contain a residual geometrical broadening common among the probes. Hence, a related geometrical shift of about $\gamma_0 = 0.159$ MHz is very reasonable. An inability of the fit (a second-degree polynomial background and a Lorentzian line shape) to nicely find the line center in the asymmetric 0 T spectrum might also contribute to γ_0. However, with an estimated uncertainty of 100% in γ_0, these error sources are accounted for in our final result for γ_2. Note that the geometrical shift seems to be the same for the extreme σ_+ and σ_- transitions; hence, the probe configuration alternations $(--++ \leftrightarrow ++--)$ actually remove this error source in the γ_1 result and the derived Landé g-factor result. Unfortunately, the handling of the probes in between the different measurements might shift the lens positions slightly, so we cannot claim a complete immunity to this shift.

Since the probe and the reference cells are kept at different temperatures, one might also suspect that a pressure shift could contribute to γ_0. However, measurements at both 3 T and 7 T, with the probe cells at room temperature, show no significant shift of the line center compared to the measurements with the probe cells at 43 °C. Pressure shifts with buffer gasses are typically up to about 10 MHz/torr [55]. Since the pressure in our cells is about 10^{-5} torr (i.e., the cesium vapor pressure), we expect pressure shifts of only up to 0.0001 MHz if the results from buffer gasses can be applied to pure cesium.

A significant error source that has been considered is the unavoidable higher-order sidebands probing the more magnetic-field-sensitive transitions with the ground state $m_J = -\frac{1}{2}$ and the excited state $m'_J = +\frac{1}{2}$. In particular, at 7 T, the eighth lower sideband in the σ_- configured probes produces a weak peak that can, in fact, impact the line-center determination. In experiments, this manifests as a clear discrepancy between the first measurement $\Delta\nu_+ - \Delta\nu_-$ and the sum of the measurements $\Delta\nu_+$ and $-\Delta\nu_-$. For our measurements at 7 T, we have therefore turned the EOM drive power down a bit from where the optical power in the fifth sideband is optimized. Thus, the eighth sideband can be greatly reduced while the fifth is only slightly reduced. Still, this error source cannot be completely removed and is hence accounted for through the uncertainty in the peak overlapping procedure.

The light shift (ac Stark effect) from the sidebands, not on resonance but detuned by multiples of ν_{EOM}, will shift the resonant transition slightly. For our case of detunings that are large compared to the Doppler width, the light shift is well approximated by

$$\Delta\nu_{\mathrm{light}} = \frac{\Gamma^2 I/I_{\mathrm{sat}}}{4(2\pi)^2\delta}, \tag{E1}$$

where Γ is the decay rate of the excited state, I is the light intensity, I_{sat} is the saturation intensity, and δ is the detuning for the sideband under consideration [26,52,56]. This effect

will be strongest for the experiments at 3 T using the third sidebands. In this case, in the center of the beam, we have approximately $I/I_{\mathrm{sat}} = 10$ for the sideband *on* resonance. Considering that the two neighboring sidebands are approximately half the intensity, and using $\delta = 14$ GHz, this gives a light shift of about 0.002 MHz. Since the two nearest sidebands in fact shift in opposite directions, we find this effect to be negligible. In addition, we have experimentally investigated the probe power dependence of the line center: At both 3 T and 7 T, we have reduced the probe power by 50% without observing any significant change in the line-center determination. Since a light shift would be proportional to the probe power, we conclude that this error source is indeed negligible.

As shown in Ref. [57], the pressure of the probe light exerts a force on the atoms that breaks the symmetry of the velocity distribution. We have not considered this effect in detail but note that it might contribute to γ_0. In fact, it may actually contribute to what we here call a geometrical shift.

APPENDIX F: FUTURE HIGH-ACCURACY MEASUREMENTS

To improve on the experiments presented in this work, a number of steps can be taken:

(i) Increasing the magnetic field will be useful, in particular, for measuring the quadratic diamagnetic shift. MRI systems, NMR spectrometers, or custom-made systems may be employed. As shown here, it can be useful to include more than one magnetic field in a study when measuring the quadratic shift, whereas the linear shift can reliably be measured using only a single magnetic field.

(ii) Improving on the field homogeneity (shimming) will be necessary to gain the most from using higher magnetic fields.

(iii) Using higher EOM drive frequencies, such that lower-order sidebands are employed, could provide a better signal-to-noise ratio and remove the problem of higher-order sidebands probing higher-lying transitions.

(iv) Developing a more robust probe design—which can sustain higher cell temperatures, has fixed and well-overlapping beams, and does not include highly paramagnetic components that complicate magnetic-field-shift calculations—could also make future measurements more accurate and possibly reduce γ_0.

(v) Alternatively, one could employ a spherical vapor cell that simply replaces the spherical water container in the setup, similarly to the approach taken in the measurement of the shielded proton gyromagnetic ratio [16]. This would remove the error source introduced by the probe field shift.

APPENDIX G: HIGH-FIELD OPTICAL MAGNETOMETRY

Here, we consider two measurement methods to implement high-field optical magnetometry.

The first method involves measuring the frequency shift from the resonance at 0 T to the resonance in field B. This method uses a single reference probe and any number of probes in the magnetic field, depending on the spatial resolution needed for the application. The laser frequency can be stabilized using the reference, while EOM generated sidebands are used to track the resonances from the probes in the magnetic field. Assuming that σ_+ configured probes are used, the magnetic field is calculated from the frequency shift, using Eq. (13), as

$$B = \frac{-\gamma_1 + \sqrt{\gamma_1^2 - 4\gamma_2(\gamma_0 - \Delta\nu_+)}}{2\gamma_2\zeta}. \tag{G1}$$

Using the values for ζ, γ_0, γ_1, and γ_2 from this work and the last optical frequency shift measurement $\Delta\nu_+$ from Table II, we find

$$B = 7.000\,076(18)\ \mathrm{T}. \tag{G2}$$

That is, we obtain a measurement of the magnetic field with 2.6 ppm accuracy.

The second method involves measuring the frequency difference $\Delta\nu_+ - \Delta\nu_-$. This method has the advantage that it is not sensitive to the diamagnetic shift and the reference offset, and that it measures about twice the frequency shift compared to first method, i.e., half the relative uncertainty. For these reasons, it is more accurate. The disadvantage is that it requires two probes in the magnetic field and, as such, only works for highly homogeneous fields. The magnetic field is calculated, using Eq. (22), as

$$B = \frac{\Delta\nu_+ - \Delta\nu_-}{2\gamma_1\zeta}. \tag{G3}$$

Using the values for ζ and γ_1 from this work and the last optical frequency difference measurement $\Delta\nu_+ - \Delta\nu_-$ from Table II, we find

$$B = 7.000\,0727(46)\ \mathrm{T}. \tag{G4}$$

That is, we obtain a measurement of the magnetic field with 0.7 ppm accuracy.

APPENDIX H: EXPERIMENTAL OBSERVATION OF THE LINE SPLITTING

The transition from the Zeeman regime to the hyperfine Paschen-Back regime for $\sigma_\pm$ lines, as shown in Fig. 2, is experimentally verified by recording spectra at different magnetic field strengths from 0 T to 1.5 T in steps of 0.1 T, as shown in Fig. 18. For this process, we have used

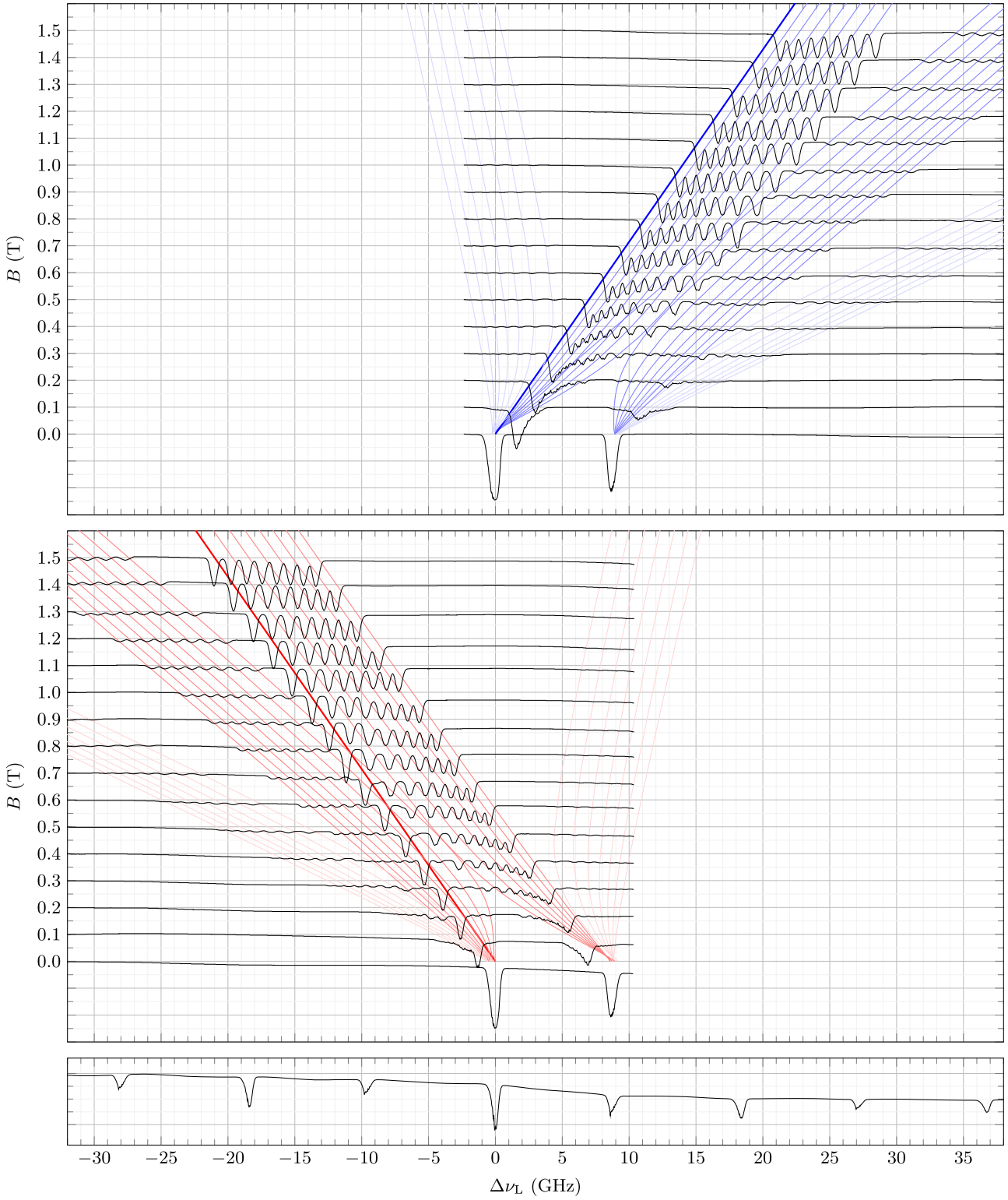

FIG. 18. Experimental verification of the line splitting using different probe positions outside the 7 T MRI scanner coil. In the upper plot σ_+ polarization is used, and in the middle plot σ_- polarization is used. In the lower plot, the reference probe at 0 T, having sidebands of 18.386 GHz, is used to determine the frequency axis, assuming a linear laser frequency scan $\Delta\nu_L$. The calculated lines are overlaid on top of the spectra. Notice that the axes are flipped, compared to Fig. 2. We see good agreement with the calculated lines.

different probe positions outside the 7 T MRI scanner coil. The magnetic field is 1.5 T near the coil opening and drops to 0.1 T about a meter away from the coil. Notice that the poor field homogeneity eliminates the saturated absorption peaks above 0.6 T.

Each transmission spectrum is displayed in arbitrary units on the B axis, according to the magnetic field at which it was obtained. The theoretical lines are overlaid and show good agreement. Notice that the axes are flipped compared to Fig. 2.

The frequency axis is determined with the reference probe at 0 T, with sidebands of 18.386 GHz, using knowledge of the hyperfine structure and assuming a linear frequency scan. The reference spectrum is shown in the bottom of the plot. For these measurements, the EOM shown in Fig. 5 is moved to the beam path going to the reference instead of probes 1–4. Since the laser frequency scan is limited to about 20 GHz, each spectrum is actually two scans stitched together (and the reference spectrum is made from four scans). As the magnetic fields are approximate, and the frequency axis is only approximately linear, these data are primarily meant to verify the pattern of the line splitting.

More rigorous studies at field strengths up to 0.845 T can be found in Refs. [58–60]. These studies also find good agreement between theory and data, and additionally analyze differences and changes in transition strengths. Because of the nonlinear nature of saturated absorption spectroscopy, the absorption depths in Fig. 18 do not accurately represent the relative transition strengths.

[1] D. Budker and M. Romalis, *Optical Magnetometry*, Nat. Phys. **3**, 227 (2007).

[2] G. Lembke, S. N. Erné, H. Nowak, B. Menhorn, A. Pasquarelli, and G. Bison, *Optical Multichannel Room Temperature Magnetic Field Imaging System for Clinical Application*, Biomed. Opt. Express **5**, 876 (2014).

[3] R. M. Hill, E. Boto, M. Rea, N. Holmes, J. Leggett, L. A. Coles, M. Papastavrou, S. K. Everton, B. A. E. Hunt, D. Sims *et al.*, *Multi-Channel Whole-Head OPM-MEG: Helmet Design and a Comparison with a Conventional System*, NeuroImage **219**, 116995 (2020).

[4] J. U. Sutter, O. Lewis, C. Robinson, A. McMahon, R. Boyce, R. Bragg, A. Macrae, J. Orton, V. Shah, S. J. Ingleby *et al.*, *Recording the Heart Beat of Cattle Using a Gradiometer System of Optically Pumped Magnetometers*, Comput. Electron. Agric. **177**, 105651 (2020).

[5] M. E. Limes, E. L. Foley, T. W. Kornack, S. Caliga, S. McBride, A. Braun, W. Lee, V. G. Lucivero, and M. V. Romalis, *Portable Magnetometry for Detection of Biomagnetism in Ambient Environments*, Phys. Rev. Appl. **14**, 011002(R) (2020).

[6] S. George, N. Bruyant, J. Béard, S. Scotto, E. Arimondo, R. Battesti, D. Ciampini, and C. Rizzo, *Pulsed High Magnetic Field Measurement with a Rubidium Vapor Sensor*, Rev. Sci. Instrum. **88**, 073102 (2017).

[7] D. Ciampini, R. Battesti, C. Rizzo, and E. Arimondo, *Optical Spectroscopy of a Microsized Rb Vapor Sample in Magnetic Fields up to 58 T*, Phys. Rev. A **96**, 052504 (2017).

[8] J. Keaveney, F. S. Ponciano-Ojeda, S. M. Rieche, M. J. Raine, D. P. Hampshire, and I. G. Hughes, *Quantitative Optical Spectroscopy of* ^{87}Rb *Vapour in the Voigt Geometry in DC Magnetic Fields up to 0.4 T*, J. Phys. B **52**, 055003 (2019).

[9] E. Klinger, H. Azizbekyan, A. Sargsyan, C. Leroy, D. Sarkisyan, and A. Papoyan, *Proof of the Feasibility of a Nanocell-Based Wide-Range Optical Magnetometer*, Appl. Opt. **59**, 2231 (2020).

[10] H. Hori, M. Miki, and M. Date, *Paschen-Back Effect of D-Lines in Sodium Under a High Magnetic Field*, J. Phys. Soc. Jpn. **51**, 1566 (1982).

[11] B. A. Olsen, B. Patton, Y.-Y. Jau, and W. Happer, *Optical Pumping and Spectroscopy of Cs Vapor at High Magnetic Field*, Phys. Rev. A **84**, 063410 (2011).

[12] L. Weller, K. S. Kleinbach, M. A. Zentile, S. Knappe, C. S. Adams, and I. G. Hughes, *Absolute Absorption and Dispersion of a Rubidium Vapour in the Hyperfine Paschen-Back Regime*, J. Phys. B **45**, 215005 (2012).

[13] A. Sargsyan, A. Tonoyan, G. Hakhumyan, C. Leroy, Y. Pashayan-Leroy, and D. Sarkisyan, *Atomic Transitions of Rb,* D_2 *Line in Strong Magnetic Fields: Hyperfine Paschen–Back Regime*, Opt. Commun. **334**, 208 (2015).

[14] A. Sargsyan, E. Klinger, G. Hakhumyan, A. Tonoyan, A. Papoyan, C. Leroy, and D. Sarkisyan, *Decoupling of Hyperfine Structure of Cs* D_1 *Line in Strong Magnetic Field Studied by Selective Reflection from a Nanocell*, J. Opt. Soc. Am. B **34**, 776 (2017).

[15] J. Keaveney, C. S. Adams, and I. G. Hughes, *ElecSus: Extension to Arbitrary Geometry Magneto-Optics*, Comput. Phys. Commun. **224**, 311 (2018).

[16] W. D. Phillips, W. E. Cooke, and D. Kleppner, *Magnetic Moment of the Proton in* H_2O *in Bohr Magnetons*, Metrologia **13**, 179 (1977).

[17] W. B. Garn, R. S. Caird, D. B. Thomson, and C. M. Fowler, *Technique for Measuring Megagauss Magnetic Fields Using Zeeman Effect*, Rev. Sci. Instrum. **37**, 762 (1966).

[18] J. T. Banasek, J. T. Engelbrecht, S. A. Pikuz, T. A. Shelkovenko, and D. A. Hammer, *Measuring 10–20 T Magnetic Fields in Single Wire Explosions Using Zeeman Splitting*, Rev. Sci. Instrum. **87**, 103506 (2016).

[19] J. T. Banasek, J. T. Engelbrecht, S. A. Pikuz, T. A. Shelkovenko, and D. A. Hammer, *Measuring 20–100 T B-Fields Using Zeeman Splitting of Sodium Emission Lines on a 500 kA Pulsed Power Machine*, Rev. Sci. Instrum. **87**, 11D407 (2016).

[20] M. R. Gomez, S. B. Hansen, K. J. Peterson, D. E. Bliss, A. L. Carlson, D. C. Lamppa, D. G. Schroen, and G. A. Rochau, *Magnetic Field Measurements via Visible Spectroscopy on the Z Machine*, Rev. Sci. Instrum. **85**, 11E609 (2014).

[21] J. M. Borrero and K. Ichimoto, *Magnetic Structure of Sunspots*, Living Rev. Solar Phys. **8**, 4 (2011).

[22] J. C. del Toro Iniesta, *On the Discovery of the Zeeman Effect on the Sun and in the Laboratory*, Vistas Astron. **40**, 241 (1996).

[23] R. Battesti, J. Beard, S. Böser, N. Bruyant, D. Budker, S. A. Crooker, E. J. Daw, V. V. Flambaum, T. Inada, I. G. Irastorza *et al.*, *High Magnetic Fields for Fundamental Physics*, Phys. Rep. **765–766**, 1 (2018).

[24] O. Schmidt, K. M. Knaak, R. Wynands, and D. Meschede, *Cesium Saturation Spectroscopy Revisited: How to Reverse Peaks and Observe Narrow Resonances*, Appl. Phys. B **59**, 167 (1994).

[25] E. Arimondo, M. Inguscio, and P. Violino, *Experimental Determinations of the Hyperfine Structure in the Alkali Atoms*, Rev. Mod. Phys. **49**, 31 (1977).

[26] D. Steck, *Cesium D Line Data*, https://steck.us/alkalidata/cesiumnumbers.pdf (2019), retrieved July 27, 2022.

[27] V. Gerginov, A. Derevianko, and C. E. Tanner, *Observation of the Nuclear Magnetic Octupole Moment of* ^{133}Cs, Phys. Rev. Lett. **91**, 072501 (2003).

[28] E. Tiesinga, P. J. Mohr, D. B. Newell, and B. N. Taylor, *CODATA Recommended Values of the Fundamental Physical Constants: 2018*, Rev. Mod. Phys. **93**, 025010 (2021).

[29] E. Arimondo, D. Ciampini, and C. Rizzo, *Chapter One—Spectroscopy of Natural and Artificial Atoms in Magnetic Fields*, Adv. At. Mol. Opt. Phys. **65**, 1 (2016).

[30] H. A. Bethe and E. E. Salpeter, *Quantum Mechanics of One- and Two-Electron Atoms* (Springer-Verlag, Berlin, 1957), pp. 209, 214.

[31] G. K. Woodgate, *Elementary Atomic Structure* (Oxford University Press, New York, 1980), pp. 149–150.

[32] P. van der Straten and H. Metcalf, *Atoms and Molecules Interacting with Light* (Cambridge University Press, Cambridge, England, 2016), pp. 181–182, 213.

[33] R. H. Garstang, *Atoms in High Magnetic Fields (White Dwarfs)*, Rep. Prog. Phys. **40**, 105 (1977).

[34] W. Hüttner, P. Otto, and M. Gamperling, *Second-Order Zeeman Effect in the* 5^2S-3^2S *and* 4^2D-3^2S *Two-Photon Transitions of Atomic Sodium*, Phys. Rev. A **54**, 1318 (1996).

[35] P. Otto, M. Gamperling, M. Hofacker, T. Meyer, V. Pagliari, A. Stifter, M. Krauss, and W. Hüttner, *Level Magnetizabilities of the Alkaline Metal Atoms*, Chem. Phys. **282**, 289 (2002).

[36] C.-J. Lorenzen and K. Niemax, *Precise Quantum Defects of nS, nP and nD Levels in Cs I*, Z. Phys. A **315**, 127 (1984).

[37] J. S. Tiedeman and H. G. Robinson, *Determination of* $g_J(^1H, 1^2S_{\frac{1}{2}})/g_s(e)$*: Test of Mass-Independent Corrections*, Phys. Rev. Lett. **39**, 602 (1977).

[38] J. Abele, M. Baumann, and W. Hartmann, g_J*-Factors and Magnetic HFS Interaction Constants in the* $6^2P_{3/2}$- *and* $8^2P_{3/2}$*-States of* ^{133}Cs, Phys. Lett. A **51**, 169 (1975).

[39] G. H. Gossel, V. A. Dzuba, and V. V. Flambaum, *Calculation of Strongly Forbidden M1 Transitions and g-factor Anomalies in Atoms Considered for Parity-Nonconservation Measurements*, Phys. Rev. A **88**, 034501 (2013).

[40] H. Stærkind, *Data Underlying: Precision Measurement of the Excited State Lande g-Factor and Diamagnetic Shift of the Cesium D2 Line*, 10.5281/zenodo.7189170 (2023).

[41] C. Barmet, N. D. Zanche, and K. P. Pruessmann, *Spatiotemporal Magnetic Field Monitoring for MR*, Magn. Reson. Med. **60**, 187 (2008).

[42] S. H. Madkhaly, L. A. Coles, C. Morley, C. D. Colquhoun, T. M. Fromhold, N. Cooper, and L. Hackermüller, *Performance-Optimized Components for Quantum Technologies via Additive Manufacturing*, PRX Quantum **2**, 030326 (2021).

[43] M. C. Wapler, J. Leupold, I. Dragonu, D. von Elverfeld, M. Zaitsev, and U. Wallrabe, *Magnetic Properties of Materials for MR Engineering, Micro-MR and Beyond*, J. Magn. Reson. **242**, 233 (2014).

[44] P. J. Mohr and B. N. Taylor, *CODATA Recommended Values of the Fundamental Physical Constants: 1998*, Rev. Mod. Phys. **72**, 351 (2000).

[45] J. F. Schenck, *The Role of Magnetic Susceptibility in Magnetic Resonance Imaging: MRI Magnetic Compatibility of the First and Second Kinds*, Med. Phys. **23**, 815 (1996).

[46] W. M. Haynes, *CRC Handbook of Chemistry and Physics*, 97th ed. (CRC Press, Boca Raton, 2016), Chap. 4, pp. 124, 126–127.

[47] J. G. Bouwman and C. J. G. Bakker, *Alias Subtraction More Efficient than Conventional Zero-Padding in the Fourier-Based Calculation of the Susceptibility Induced Perturbation of the Magnetic Field in MR*, Magn. Reson. Med. **68**, 621 (2012).

[48] J. G. Bouwman, *Forward Field-Shift Calculation for MRI*, https://www.mathworks.com/matlabcentral/fileexchange/37278-forward-field-shift-calculation-for-mri (2014), retrieved May 30, 2022.

[49] K. M. Koch, X. Papademetris, D. L. Rothman, and R. A. de Graaf, *Rapid Calculations of Susceptibility-Induced Magnetostatic Field Perturbations for in vivo Magnetic Resonance*, Phys. Med. Biol. **51**, 6381 (2006).

[50] R. W. Brown, Y.-C. N. Cheng, E. M. Haacke, M. R. Thompson, and R. Venkatesan, *Magnetic Properties of Tissues*, in *Magnetic Resonance Imaging* (John Wiley & Sons, New York, 2014), Chap. 25, pp. 739–777.

[51] B. W. Petley and R. W. Donaldson, *The Temperature Dependence of the Diamagnetic Shielding Correction for Proton NMR in Water*, Metrologia **20**, 81 (1984).

[52] C. J. Foot, *Atomic Physics* (Oxford University Press, New York, 2012), pp. 98, 142, and 144.

[53] *MATLAB, Curve Fitting Toolbox User's Guide*, https://se.mathworks.com/help/pdf_doc/curvefit/curvefit.pdf (2022), retrieved July 27, 2022.

[54] S. A. Fedorov, G. A. Vishnyakova, E. S. Kalganova, D. D. Sukachev, A. A. Golovizin, D. O. Tregubov, K. Y. Khabarova, A. V. Akimov, N. N. Kolachevsky, and V. N. Sorokin, *Improved Measurement of the Hyperfine Structure of the Laser Cooling Level* $4f^{12}(^3H_6)5d_{5/2}6s^2(J = 9/2)$ *in* $^{169}_{69}$Tm, Appl. Phys. B **121**, 275 (2015).

[55] G. A. Pitz, C. D. Fox, and G. P. Perram, *Pressure Broadening and Shift of the Cesium* D_2 *Transition by the Noble Gases and* N_2, H_2, *HD,* D_2, CH_4, C_2H_6, CF_4, *and* ^{3}He *with Comparison to the* D_1 *Transition*, Phys. Rev. A **82**, 042502 (2010).

[56] L. Young, W. T. Hill, S. J. Sibener, S. D. Price, C. E. Tanner, C. E. Wieman, and S. R. Leone, *Precision Lifetime Measurements of Cs 6p* $^2P_{1/2}$ *and 6p* $^2P_{3/2}$ *Levels by Single-Photon Counting*, Phys. Rev. A **50**, 2174 (1994).

[57] R. Grimm and J. Mlynek, *The Effect of Resonant Light Pressure in Saturation Spectroscopy*, Appl. Phys. B **49**, 179 (1989).

[58] A. Sargsyan, A. Tonoyan, G. Hakhumyan, A. Papoyan, E. Mariotti, and D. Sarkisyan, *Giant Modification of Atomic Transition Probabilities Induced by a Magnetic Field: Forbidden Transitions Become Predominant*, Laser Phys. Lett. **11**, 055701 (2014).

[59] A. Sargsyan, B. Glushko, and D. Sarkisyan, *Micron-Thick Spectroscopic Cells for Studying the Paschen–Back Regime on the Hyperfine Structure of Cesium Atoms*, J. Exp. Theor. Phys. **120**, 579 (2015).

[60] A. Sargsyan, A. Amiryan, A. Tonoyan, E. Klinger, and D. Sarkisyan, *Coherent Optical Processes on Cs* D_2 *Line Magnetically Induced Transitions*, Phys. Lett. A **434**, 128043 (2022).

6 Second Paper: "High-Field Optical Cesium Magnetometer for Magnetic Resonance Imaging"

This paper is still unpublished as of this writing. It has been submitted with the suggested popular summary:

"High magnetic fields are today a crucial element in many branches of science and technology. When measuring magnetic fields of several teslas, four conventional techniques can be employed, each with their characteristic pros and cons. The choice of the sensor depends on the application. Some applications, such as fusion reactors, particle accelerators, and MRI scanners, are pushing the limits of the conventional high-field magnetometry techniques, and in some cases the ideal sensor simply does not exist.

We have developed a completely new kind of optical quantum magnetometer, challenging the decades long status quo in high-field magnetometry. The technology is based on tracking a magnetic-field dependent optical resonance in cesium atoms. That is, a particular frequency of infrared light, absorbed by an atomic cesium gas, which changes in response to different magnetic field strengths. Even though this is the very first demonstration of the technology, we demonstrate an accuracy

rivaling the established paradigms, and powerful features including high bandwidth and low electromagnetic interference.

We show that the sensor can be used to clearly detect imperfections in a 7 tesla MRI scanner coil system, highlighting the potential use in MRI image improvement. We note that the sensor also seems like an attractive tool for use in fusion reactors and particle accelerators. Future work will improve on the current prototype and investigate, in the first place, the appealing applications in MRI."

High-Field Optical Cesium Magnetometer for Magnetic Resonance Imaging

Hans Stærkind [1,2,*] Kasper Jensen [1,3] Jörg H. Müller [1]
Vincent O. Boer [2] Eugene S. Polzik [1] and Esben T. Petersen [2,4]

[1] *Niels Bohr Institute, University of Copenhagen, Blegdamsvej 17, 2100 Copenhagen, Denmark*
[2] *Danish Research Centre for Magnetic Resonance, Centre for Functional and Diagnostic Imaging and Research, Copenhagen University Hospital - Amager and Hvidovre, Kettegård Allé 30, 2650 Hvidovre, Denmark*
[3] *School of Physics and Astronomy, University of Nottingham, University Park, Nottingham NG7 2RD, England, United Kingdom*
[4] *Section for Magnetic Resonance, DTU-Health Tech, Technical University of Denmark, Oersteds Plads, Building 349, 1st floor, 2800 Kgs Lyngby, Denmark*

(Dated: September 26, 2023)

We present a novel high-field optical quantum magnetometer based on saturated absorption spectroscopy on the extreme angular-momentum states of the cesium D_2 line. With key features including continuous readout, high sampling rate, and sensitivity and accuracy in the ppm-range, it represents a competitive alternative to conventional techniques for measuring magnetic fields of several teslas. The prototype has four small separate field probes, and all support electronics and optics are fitted into a single 19-inch rack to make it compact, mobile, and robust. The field probes are fiber coupled and made from non-metallic components, allowing them to be easily and safely positioned inside a 7 T MRI scanner. We demonstrate the capabilities of this magnetometer by measuring two different MRI sequences, and we show how it can be used to reveal imperfections in the gradient coil system, to highlight the potential applications in medical MRI. We propose the term EXAAQ (EXtreme Angular-momentum Absorption-spectroscopy Quantum) magnetometry, for this novel method.

I. INTRODUCTION

High magnetic fields play a critical role in many areas of science and technology. These include fundamental physics [1], materials science [2, 3], mass spectrometry [4, 5], particle accelerators [6, 7], nuclear fusion [8, 9], magnetic levitation [10–12], chemistry [13, 14] and medical imaging [15, 16].

When measuring high magnetic fields, of more than 1 T, four different conventional techniques can be employed, each with their own advantages and disadvantages [17–19]. *Nuclear magnetic resonance (NMR) magnetometers*, using protons, deuterons, helions, or heavier nuclei, measure the scalar magnetic field magnitude and are superior in terms of accuracy and sensitivity, but typically function in a pulsed way and require high field homogeneity [20–23]. *Hall probes* provide continuous measurements of a vector component of the magnetic field, with high spatial resolution, but with lower sensitivity [24]. *Fluxmeters* are very sensitive, but they are relative devices that can only measure changes in magnetic fields along a specific direction and will drift when operated continuously [25–27]. *Magneto-optical Faraday rotation magnetometers* provide fast optical measurements of a vector component of the magnetic field, but with poor sensitivity [28, 29].

Optical magnetometry based on measuring the Zeeman shift of alkali D lines provides a fifth approach [30–33], but the real potential of this method has still not been demonstrated, and no practical applications have been explored yet. In this work we build upon the recent fundamental advances described in [34], to realize a novel prototype optical magnetometer that gives a fast and continuous measurement of the scalar magnetic field magnitude, with a high accuracy and sensitivity. The optical probes provide easy and interference-free operation, with minimal electromagnetic disturbances in the measured volume. Overall, this provides a compelling new technique for measuring high magnetic fields that may prove advantageous compared to conventional methods for certain applications, and even enable new ones. Like NMR magnetometers, this optical magnetometer is a quantum sensor that achieves absolute accuracy by exploiting the fact that all atoms of a given species are perfectly identical. This gives a high robustness against component ageing, and ambient fluctuations.

The method is based on fast tracking of a magnetic-field-dependent near-infrared transition in cesium, combining sideband spectroscopy, saturated absorption spectroscopy, and frequency modulation (FM) spectroscopy. A similar approach has originally been proposed in [35]. Here we present the first ever physical realization of such a device.

We have developed the prototype specifically to monitor the magnetic field inside a magnetic resonance imaging (MRI) scanner. As described in [36], accurate magnetic field data can be used in the MRI image reconstruction to improve image quality, with potential impact in both medical research and clinical diagnostics. To facilitate the development and testing of the proto-

* hans.staerkind@nbi.ku.dk

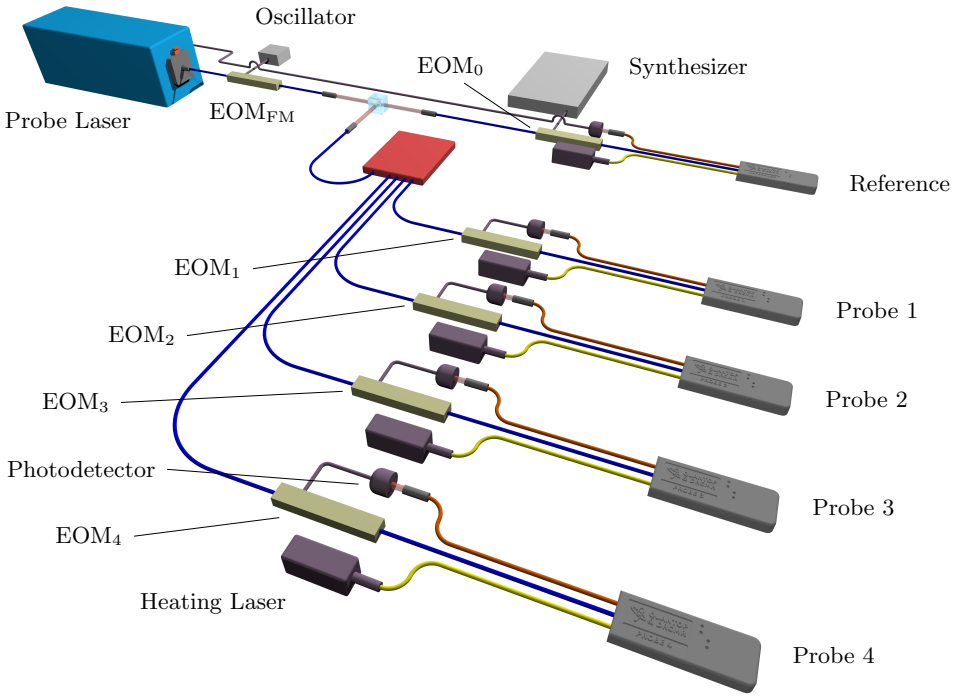

FIG. 1. Optical setup. Probe laser light is modulated by $\mathrm{EOM_{FM}}$, split by a free-space beam splitter, and then further split by a 1x4 fiber splitter, for a total of five different paths. Each path is again modulated by an EOM, before the probe light is sent to the reference probe at 0 T and probes 1–4 in the MRI scanner. Colored cables represent optical fibers, and black cables represent the analog feedbacks realizing the accurate measurement scheme.

type in a hospital setting, it has been made to fit into a 19-inch rack, making it compact, mobile, robust, and easy to quickly turn on and operate. This has been necessary since the extreme magnetic-field conditions inside an MRI scanner are not easily reproduced in a typical lab environment. The prototype is characterized and tested in a Philips Achieva 7 T MRI scanner. We benchmark the performance in terms of sensitivity and bandwidth, and show measurements of an echo-planar imaging (EPI) sequence and a spiral imaging sequence. These measurements lead to an investigation of clearly detectable nonlinearities and instabilities in the gradient coil system, indicating that the prototype already performs at a level where it can serve as a useful tool for investigating the performance of the MRI scanner. Finally we discuss the absolute accuracy of the method.

With this EXAAQ (EXtreme Angular-momentum Absorption-spectroscopy Quantum) device being the very first of its kind, there are numerous opportunities to further improve its reliability, sensitivity, and accuracy. While we will continue to develop and improve the prototype towards applications in MRI, we note that a modified design may find applications in other fields. This could include: magnetic diagnostics in steady state fusion experiments, where the drift of fluxmeters or radiation damage to Hall probes becomes a problem [37, 38]; accurate control of dipole magnets in particle accelerators, through continuous optical monitoring as originally proposed in [35]; or quench detection in (high-temperature) superconducting magnets as an alternative to "quench antennas" or Hall probe arrays [39].

II. METHOD

A. The optical transition

The magnetometer works by continuously tracking the frequency shift of the cesium-133 D_2 line. Specifically it measures the shift $\Delta\nu_+$, of the σ_+ transition between the extreme angular-momentum states, shown in [34] to have a magnetic field dependence of

$$\Delta\nu_+ = \gamma_1 B + \gamma_2 B^2. \tag{1}$$

Here $\gamma_1 = 13.994\,301(11)$ GHz/T is the linear magnetic frequency shift of the transition, $\gamma_2 = 0.4644(35)\,\mathrm{MHz/T^2}$ is the quadratic diamagnetic shift of the transition, and B is the magnitude of the magnetic field. This expression is modified to

$$\Delta\nu_+ = \gamma_0 + \gamma_1\zeta B + \gamma_2\zeta^2 B^2, \tag{2}$$

such that B is defined as in the absence of the probe, by taking into account the probe induced field shift

$\zeta = 1 + 0.49(50) \times 10^{-6}$. A small frequency measurement offset γ_0, depending on the measurement method, is also included in Eq. (2).

With the linear magnetic frequency shift of about 14 GHz/T dominating Eq. (2), we have a frequency shift of about 98 GHz in the 7 T MRI scanner, where we test the magnetometer.

B. Setup

A schematic view of the optical setup is shown in Fig. 1. The probe laser is a Toptica DL Pro, 852 nm, external cavity diode laser (ECDL). The probe laser light is first modulated at $\nu_{\mathrm{FM}} = 5.32\mathrm{MHz}$ by an electro-optical modulator (EOM), which we label $\mathrm{EOM_{FM}}$. This modulation is necessary for performing FM spectroscopy as described in section II D. The laser beam is then split in two paths, and one path is further split into four, for a total of five different paths. In each path the probe light is again modulated by an EOM to generate strong sidebands for sideband spectroscopy as detailed in section II C. In each path the light is then sent to a 3D-printed probe, containing all the optics for performing saturated absorption spectroscopy [40] on a laser-heated spectroscopy cell. An exploded view of the probe assembly is shown in Fig. 2. Apart from the input fiber for the probe light, the probes

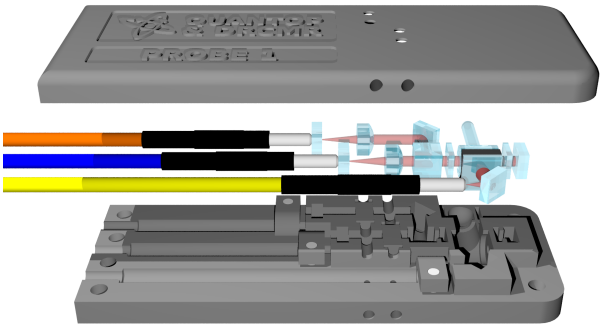

FIG. 2. Exploded view of the optical probe assembly. Probe light comes from the blue fiber, and exits through the orange fiber. High-power laser light from the yellow fiber heats the cesium vapor cell, to increase the cesium atomic density. The assembled probes dimensions are $90 \times 33 \times 10\,\mathrm{mm}^3$.

also have an input fiber for the heating laser beam, and an output fiber for returning the probe light to a photodetector. The fibers are 19 m long allowing the rack to be placed at a safe distance from the measurement points.

The probes are labeled "probes 1–4", and "reference" as seen in Fig. 1. Probes 1–4 are used to measure at four different positions inside the MRI scanner, and the reference probe is placed in a magnetic shield in the rack. Probes 1–4 are all configured with σ_+ polarized probing light, whereas the reference uses linearly polarized light to prevent the transition frequency from shifting in small residual field fluctuations inside the magnetic shield. For details on the optical probe design see [34].

Each of probes 1–4 are heated with 1.2 W of optical power to a temperature of about 44 °C, and uses about 180 µW of probing light. The reference is heated with 250 mW to a temperature of about 35 °C, and uses about 220 µW of probing light.

C. Frequency shift measurement

With the reference in the magnetic shield at 0 T, and the four probes in the MRI scanner at 7 T, we initialize the magnetometer using a two-step procedure.

In the first step the probe laser frequency is stabilized 97.5 GHz above the 0 T transition. This is achieved by driving the modulator in the reference path, $\mathrm{EOM_0}$, with a frequency $\nu_0 = 19.5$ GHz and power optimized for the fifth optical sidebands. The laser frequency is adjusted such that the lower fifth sideband is resonant with the 0 T transition, and the laser is then stabilized at this frequency by an electronic feedback to the laser current controller. Feedback methods are described in section II D.

In the second step the modulator EOM_i, in each of the four probe paths $i = \{1, 2, 3, 4\}$, is used to modulate the probe light with a frequency of about $\nu_i = 0.5$ GHz and power optimized for the first sidebands. The modulation frequency is fine-tuned such that the first upper sideband is resonant with the 7 T transition, and it is then stabilized using an electronic feedback to the voltage controlled oscillator (VCO) driving EOM_i. Now the total frequency shift from Eq. (2) can be found as

$$\Delta\nu_+ = 5 \cdot \nu_0 + \nu_i, \tag{3}$$

as shown in Fig. 3. A measurement of ν_i then corresponds directly to a magnetic field measurement through Eqs. (2) and (3).

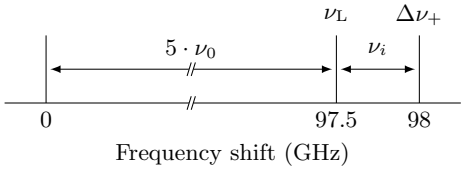

FIG. 3. The sideband spectroscopy frequency shift measurement scheme illustrated. The probe laser frequency ν_{L} is stabilized 97.5 GHz above the 0 T transition by spectroscopy with the lower fifth sideband of $\nu_0 = 19.5$ GHz using the reference probe. For each of the probes $i = \{1, 2, 3, 4\}$, a first upper sideband of about 0.5 GHz follows the 7 T transition. The total frequency shift, $\Delta\nu_+$, is then found as $5 \cdot \nu_0 + \nu_i$.

The feedback will, once initialized, make sure that the modulation frequency ν_i follows changes in the resonance frequency, corresponding to changes in the magnetic field,

such that Eq. (3) remains valid at all times, except for a small possible error due to the finite speed of the feedback. Each of the four probes in the MRI scanner has its own feedback, so that an independent measurement is made by each probe.

The VCOs used to drive $\mathrm{EOM}_{1\text{–}4}$ can produce frequencies ν_i, in the range from 320 to 760 MHz, giving the magnetometer a dynamic range of about ± 15 mT. With the probes at a distance of 15 cm from the MRI magnet isocenter, this allows for measurements of magnetic field gradients up to 100 mT/m, which is more than most MRI gradient coil systems can produce. It should be noted that the system can easily be reconfigured to measure around a completely different field strength, e.g. for 3 T or 1.5 T MRI scanners, by simply changing ν_0.

D. Feedback

A saturated absorption spectroscopy signal is symmetric around the resonance frequency, and as such is not directly useful in a feedback. To make a feedback, an asymmetric error signal must be generated from the probe laser light, such that positive and negative frequency detunings are easily distinguished. This is achieved using FM spectroscopy [41]. In FM spectroscopy the probing light is modulated at a frequency similar to the linewidth of the transition. The sidebands and carrier pick up different phase shifts, and interfere to give a light intensity that oscillates at the modulation frequency with phase and amplitude depending on the sign and magnitude of the detuning. The probe laser light is modulated at $\nu_{\mathrm{FM}} = 5.32$ MHz, using $\mathrm{EOM}_{\mathrm{FM}}$, since this frequency is similar to the transition linewidth of 5.2 MHz [42, 43], and also matches the free spectral range of the fiber etalons, such that their contribution to the error signal is suppressed.

Each photodetector is designed as a parallel RLC circuit with a resonance of ν_{FM} and a Q-factor of about 15, to reduce sensitivity outside the relevant narrow frequency band. The signal from the photodetector is sent to a lock-in amplifier, consisting of an analog mixer and a 1.9 MHz low pass filter (LPF), to produce the error signal e_i. The error signal is a voltage which is positive for negative detunings, and negative for positive detunings. The error signal is sent to an integrator, which controls the VCO with a voltage U_i, to produce a frequency ν_i, which is sent to EOM_i. This is all shown in Fig. 4.

As an example, we examine what happens when the magnetic field suddenly increases at the position of probe i, resulting in a negative detuning of the first upper EOM_i generated sideband. This will give a positive e_i, which will be integrated to give a rising U_i, increasing ν_i until the negative detuning is fully compensated, and e_i is again zero. This corresponds to the first upper EOM_i generated sideband again being on resonance with the atomic transition, and Eq. (3) again being valid.

The laser frequency stabilization using the reference probe at 0 T and a fixed ν_0 is similar, except that there is no VCO. In this case the integrator directly controls the laser current, compensating, e.g., mechanical disturbances and temperature fluctuations, to keep the laser frequency constant at all times.

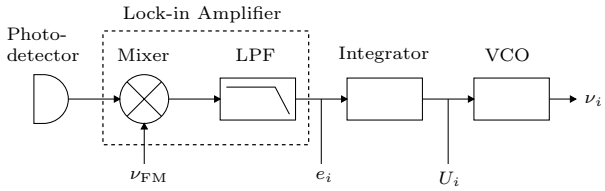

FIG. 4. The analog feedback used to control the frequencies of $\mathrm{EOM}_{1\text{–}4}$. The signal from the frequency-selective photodetector is passed through a lock-in amplifier, to generate the error signal e_i. This is integrated by an analog op-amp integrator, to produce a voltage U_i, controlling a VCO, producing a frequency ν_i, which is sent to EOM_i.

Eq. (4) can be generalized to situations where the field is rapidly changing, and the first upper sideband is not exactly on resonance. In this case we have

$$\Delta\nu_+ = 5 \cdot \nu_0 + \nu_i - e_i/s_i, \tag{4}$$

where s_i is the slope of the error signal as a function of detuning.

For the measurements presented in the following, ν_i is found from U_i, using a voltage-to-frequency mapping of the VCOs. The VCOs behave as low pass filters with a time constant of about 4 µs, corresponding to a bandwidth of about 40 kHz. These numbers also include response times of photodetectors and lock-in amplifiers.

III. RESULTS

A. 19-inch rack integration

To make a compact device that can be operated in a hospital setting, the setup is divided in several modules and mounted in a 19-inch rack. This also makes it easy to move around and close off, when not in use. To make it robust, all optical parts of the setup are directly connected by fibers; except for the beam splitting after $\mathrm{EOM}_{\mathrm{FM}}$, which is realized with free-space optics, to allow for optical power adjustments. The device is shown in Fig. 5.

During measurements, the device is placed in the control room of the MRI scanner, the probes enter the radio frequency (rf) shielded scanner room through a waveguide, and are placed in the bore of the scanner in a 3D printed plastic grid, with a precision of about 1 mm.

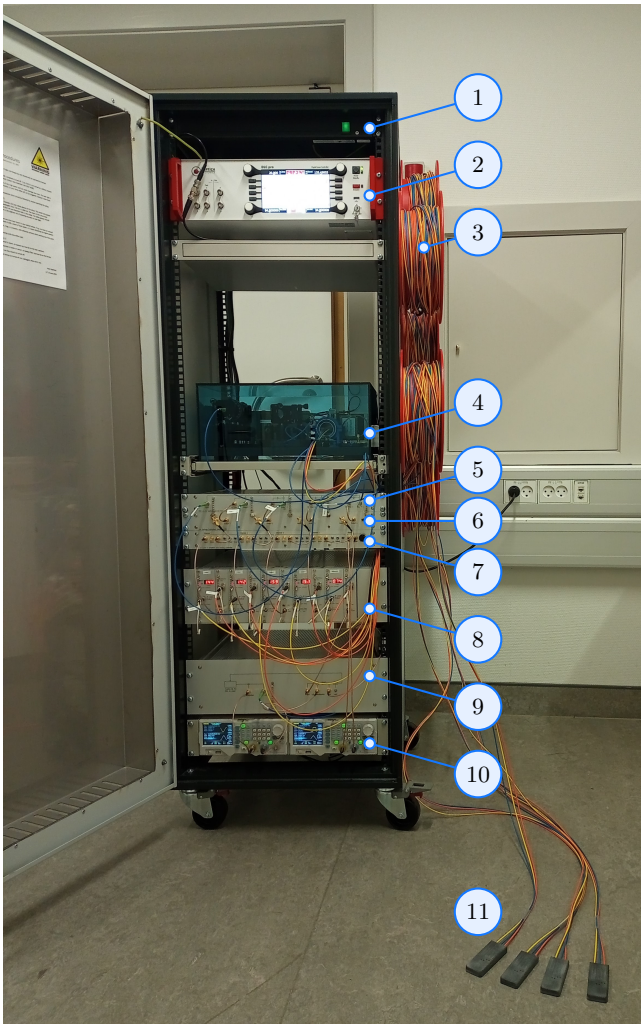

FIG. 5. EXAAQ magnetometer prototype. 1: On/off switch. 2: Toptica DLC Pro laser controller. 3: Cable reels with 19 m of fiber. 4: Optical breadboard with free-space beam splitting, synthesizer and amplifier for ν_0, EOM_0, and magnetic shield with reference. 5: 1x4 fiber splitter, amplifiers for $\nu_{1\text{–}4}$, and $\mathrm{EOM}_{1\text{–}4}$. 6: VCOs. 7: Lock-in amplifiers and integrators for probes 1–4. 8: Subrack with photodetectors and heating lasers. 9: Probe laser, $\mathrm{EOM}_{\mathrm{FM}}$, and lock-in amplifier and integrator for reference. 10: Oscillators for ν_{FM} and VCO voltage scanning. 11: Probes 1–4.

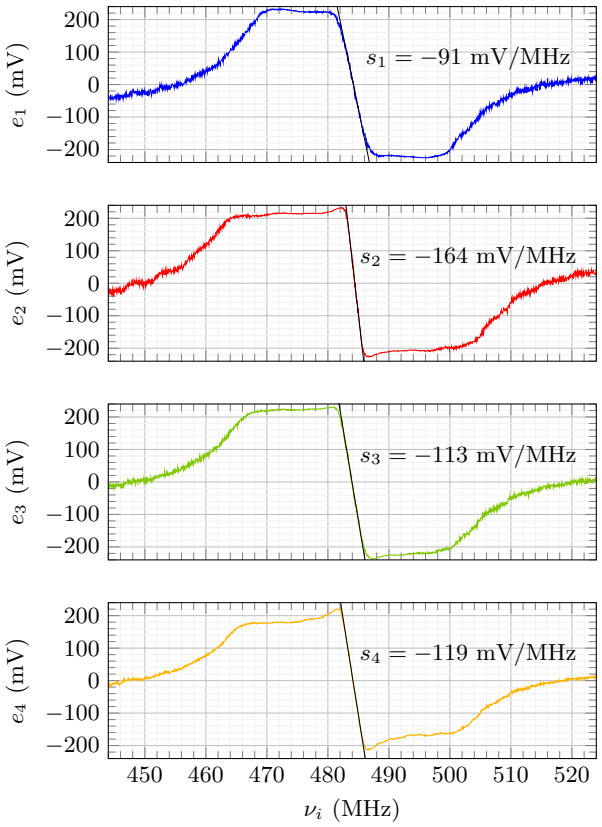

FIG. 6. Error signals e_i, recorded as a function of ν_i. This range of frequencies is produced by sweeping U_i about 2 V. A fit to the linear region around resonance, $e_i = 0$, returns the slopes s_i.

B. Calibration and sensitivity characterization

With the laser frequency stabilized, and the probes in the MRI scanner bore, the error signal slopes s_i, from Eq. (4), are determined. This is done by sweeping the VCO control voltage U_i, and thereby the frequency ν_i, while recording the error signal e_i. A straight line is fitted to the linear region around resonance, as shown in Fig. 6, to find the slopes s_i.

Once the probe feedbacks are initialized, the VCO frequencies ν_i are continuously regulated so that Eq. (4) remains valid as long as the error signals e_i stay within the approximately linear region of about ± 1.5 MHz.

To calibrate the probes in absolute terms, we first measure the magnetic field in the MRI scanner by NMR magnetometry. Placing a spherical sample of ultrapure water in the scanner and measuring a free induction decay following nuclear excitation, we find the magnetic field in the center of the scanner to be 7.000 066 T [34, 45]. We then measure $\Delta\nu_+$ as defined in Eq. (4), with each of the four probes for 1 second. We assume that the high magnetic field generated by the superconducting MRI coil is completely unchanged during all measurements. Using Eq. (2) we then calculate a γ_0 for probes 1–4 of 0.07, 0.19, -0.26, and -0.19 MHz, respectively. Using these values we measure example magnetic field traces as shown in Fig. 7. Here a sampling rate of 40 kHz is used, corresponding to a highest detectable (Nyquist) frequency of 20 kHz. Noise common among the probes is likely due to imperfections in the frequency stabilization of the probe laser.

Over a 1 second measurement we measure traces with standard deviations of 5.0, 4.3, 4.3, and 3.9 µT, respectively. This constitutes a sub-ppm resolution of the magnetometer. We calculate the power spectral density

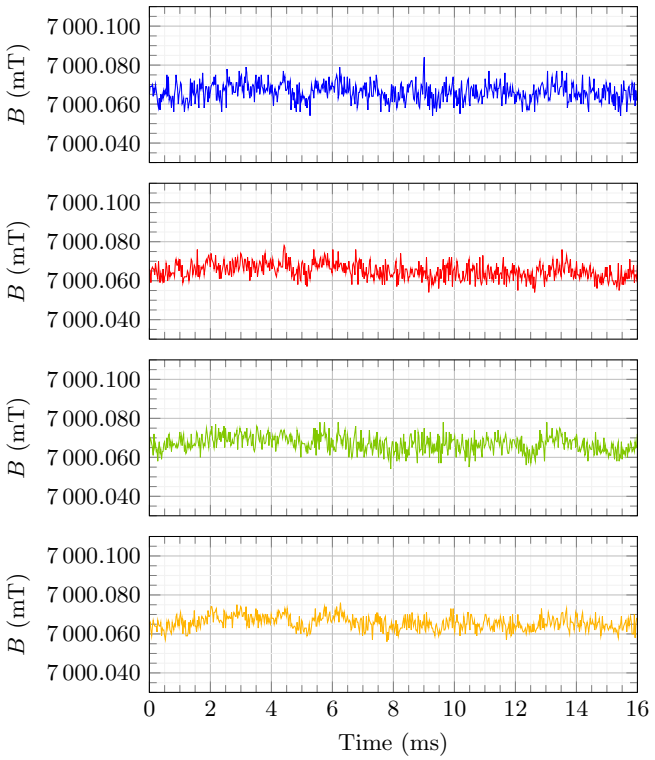

FIG. 7. Example measurements, in the magnetic field of the MRI scanner. The sampling rate is 40 kHz. The field is assumed to be a perfect 7 000.066 mT. Colors blue, red, green, and yellow corresponds to probes 1–4, respectively. Probe 4 is the one that has the least noise, with a standard deviation of 3.9 µT, over a 1 second measurement. Noise common among the probes is attributed to imperfect frequency stabilization of the probe laser.

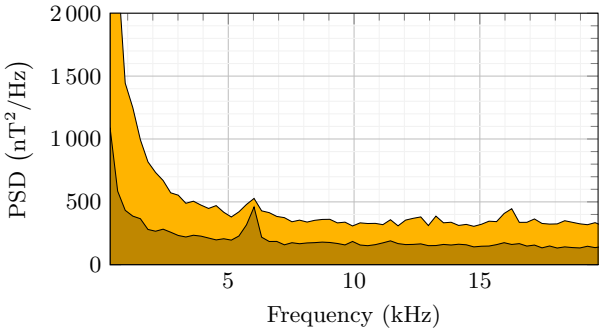

FIG. 8. The PSD of a measurement with probe 4. The shaded lower area shows the noise of the data acquisition system.

(PSD) as shown in Fig. 8 for the measurement with probe 4, which is the one that performs the best, and note that the noise is worst below 3 kHz. The sensitivity can be calculated as the square root of the PSD, and has a root mean square value of 28 nT/$\sqrt{\text{Hz}}$ in the 0–20 kHz band. It is worth noting that the noise of the data acquisition system used for measuring U_i, also shown in Fig. 8, corresponds to a standard deviation of 2.5 µT, so this is currently a limiting factor for the sensitivity. Over a 20 minutes period we observe drifts of 23, 17, 34, and 24 µT, respectively, i.e. a long term stability of a few ppm.

C. MRI sequence measurements

We demonstrate the functioning of the prototype by measuring the field in four different positions inside the MRI scanner while scanning. During an MRI scan three orthogonal gradient coils are playing a sequence of carefully controlled magnetic field gradients. Here we investigate typical 2D MRI sequences: First a slice selecting gradient in one direction is played during nuclear rf excitation. This is followed by a series of gradients in the orthogonal plane, producing changing spatial nuclear spin phase rolls in the excited slice. These changing phase rolls determine the trajectory though k-space during inductive readout of the nuclear rf signal. During the final image reconstruction the acquired k-space image is Fourier transformed to give the actual image [44].

We define the coordinate system (x, y, z) of the MRI scanner with x-axis along the down/up direction, y-axis along the left/right direction, and z-axis along the field direction. The origin $(0, 0, 0)$ corresponds to the isocenter of the MRI scanner. The probes 1–4 are placed in positions $(15\,\text{cm}, 0, 0)$, $(0, 15\,\text{cm}, 0)$, $(0, 0, 15\,\text{cm})$, and $(0, 0, 0)$, respectively. In this way probes 1 and 2 measure the (x, y)-gradients defining the k-space trajectory, probe 3 measure the slice selecting z-gradient and 4 should ideally measure a constant field.

To demonstrate that the technique works well, even for rapidly changing fields, an EPI sequence with maximum gradient strength (39.87 mT/m) and maximum slew rate (198.38 mT/m/ms) is played on the MRI scanner while measuring with the four probes. The measured e_i/s_i and ν_i, and the magnetic fields B, calculated using Eqs. (2) and (4), are shown in Fig. 9. Importantly, it is seen here that the error signals stay within the approximately linear region, demonstrating that even for the fastest gradient switching, that the MRI scanner can produce, the method still works.

The trajectory though k-space is given by the integral of the gradients, so the EPI sequence covers k-space through a zigzag line-by-line trajectory. Different sequences use (among other things) different k-space trajectories to adjust e.g. tissue contrast, field-of-view, or scan duration. In Fig. 10 we show a recording of a spiral imaging sequence, which covers k-space in an outwards spiralling trajectory, by playing out-of-phase oscillating x- and y-gradients with increasing amplitude.

These two examples clearly illustrate that the prototype works well and represents a valuable tool for the MRI scientist who needs a direct measurement of the magnetic field inside the scanner.

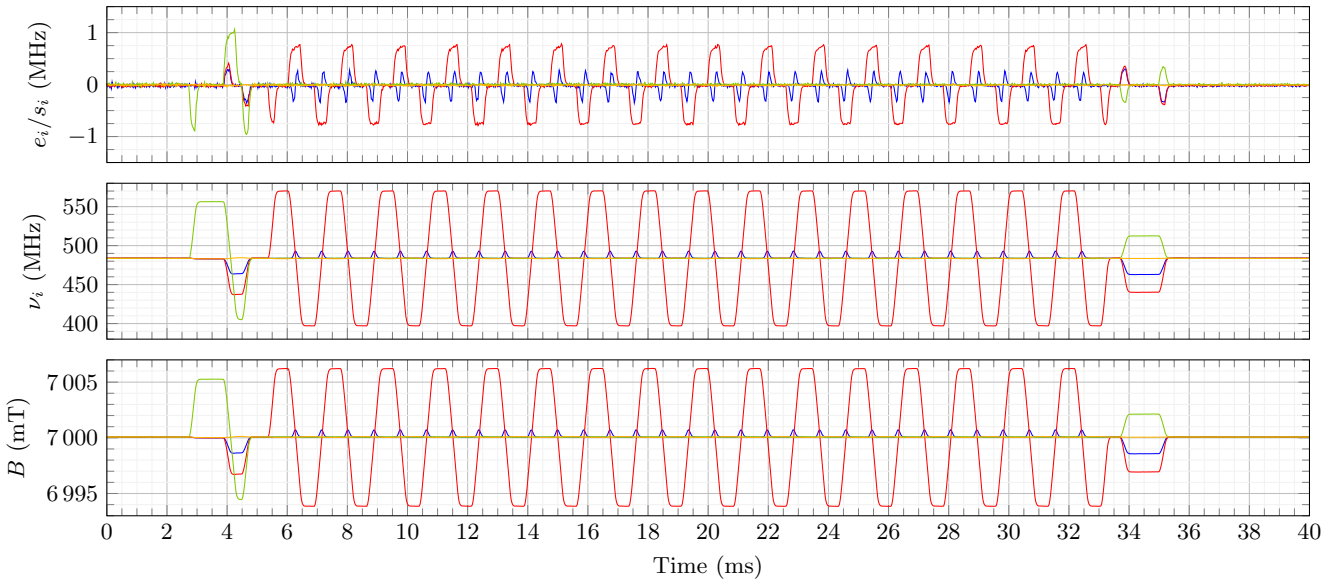

FIG. 9. Magnetic field measurements during an EPI sequence with probes 1–4, in colors blue, red, green, and yellow, respectively. In the upper plot are shown the differences between the first upper sidebands and the atomic resonances. In the middle plot are shown the VCO frequencies. In the lower plot are shown the magnetic fields calculated using Eqs. (2) and (4). The reader familiar with MRI sequence development will recognize slice selection, prewinder, k-space coverage, and spoiler [44].

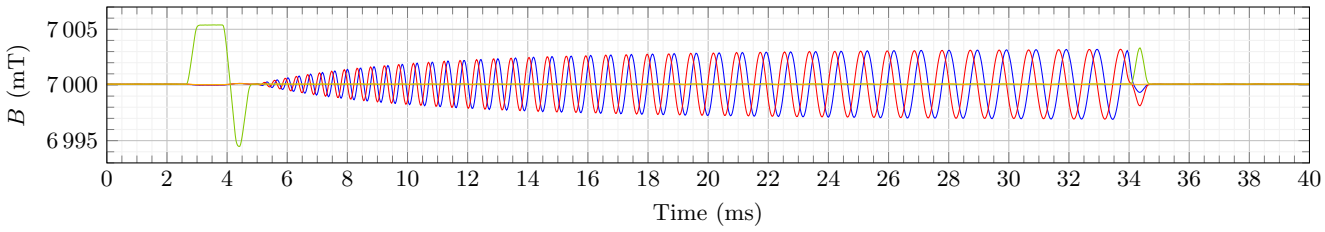

FIG. 10. Magnetic field measurements during a spiral imaging sequence with probes 1–4, in colors blue, red, green, and yellow, respectively.

D. Gradient imperfection detection

Since the k-space trajectory is determined by the field gradients, inaccurate knowledge of the gradients will result in an inaccurate k-space image. Errors in the k-space image will, in turn, translate into artifacts or blurring in the Fourier transformed actual anatomical image. For this reason accurate measurements of the magnetic field gradients during an MRI sequence, can be used for k-space trajectory corrections, which ultimately can lead to improved MRI image quality.

Many different factors may contribute to deviations from the desired magnetic field during a sequence: Crosstalk among the coils and other nearby conducting material — i.e. eddy currents, imperfect design of the coil system and the associated current controllers, heating of the coils during extended operation, etc.

Two observations in the obtained MRI sequence data warrant further investigation: For probe 2 in the EPI sequence measurement, we calculate a maximum gradient strength which is about 200 µT higher than expected. For probe 2 in the spiral sequence measurement, decaying oscillations, with amplitudes up to about 10 µT, are observed immediately after the sequence has finished, where the field should ideally be completely stable. These observations are not visible in the zoomed out views of Figs. 9 and 10. To further investigate and clearly display these disagreements we reposition probes 1–4 to positions $(0, -15\,\mathrm{cm}, 0)$, $(0, -7.5\,\mathrm{cm}, 0)$, $(0, +7.5\,\mathrm{cm}, 0)$, and $(0, +15\,\mathrm{cm}, 0)$, respectively, and play the two sequences again.

With the new probe positions we first have a closer look at the two first maximum gradient pulses in the EPI sequence in Fig. 11. In Fig. 12 we plot the magnetic field values at the first gradient plateau for the four probes along with the field of an ideal 39.87 mT/m gradient. We also plot the residuals between the data and the idealization, and what is seen is a clear nonlinearity of the magnetic field generated by the y-gradient coil. To have nonlinearities like this is expected, and the order of

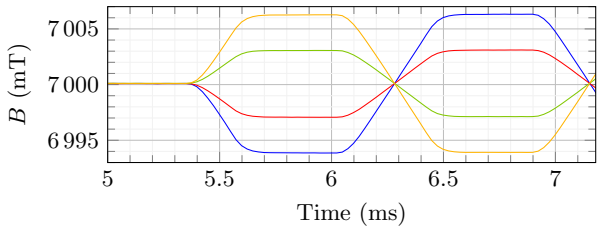

FIG. 11. A small section of the EPI sequence shown in Fig. 9, recorded with the probes distributed along the y-axis.

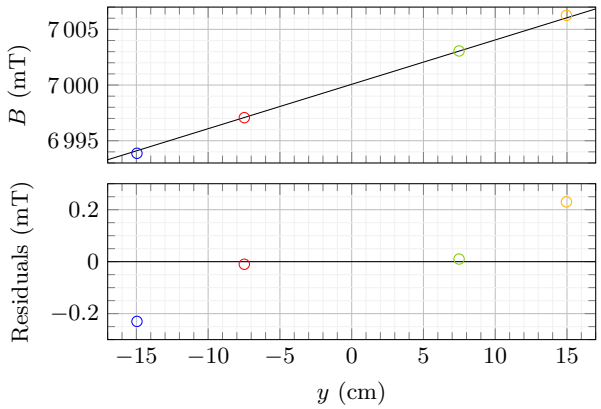

FIG. 12. Nonlinearity in the magnetic field of the y-gradient coil. In the upper plot the magnetic field values of the first gradient plateau in Fig. 11 are shown, along with an ideal 39.87 mT/m gradient. In the lower plot the residuals between the measured field and the ideal gradient are shown. At ±15 cm we see deviations of about 4 %.

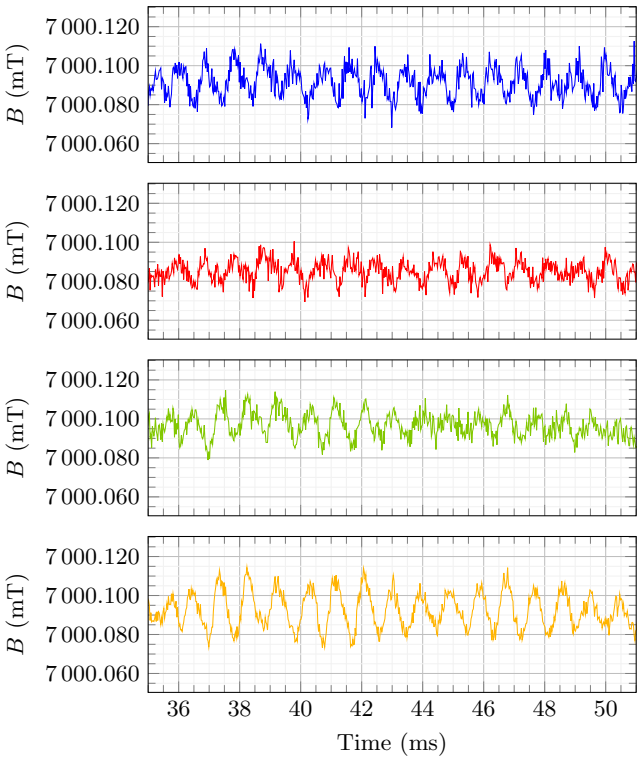

FIG. 13. Measurement of the first 16 ms after the spiral sequence shown in Fig. 10, recorded with the probes distributed along the y-axis. Blue, red, green, and yellow traces corresponds to positions −15, −7.5, +7.5, and +15 cm respectively. Oscillating eddy currents are clearly seen. Notice how the measurement has drifted about 20–30 µT, since the calibration done 15 minutes earlier.

magnitude — about 4% at 15 cm from the isocenter — is comparable to what is e.g. found in [46].

For the spiral sequence we start by looking at the field during the first 16 ms after the sequence in Fig. 13. Clear oscillations are seen. Highest amplitudes are seen for probes 1 and 4, which are the farthest away from the isocenter, and opposite amplitudes are seen for probes 1 and 2 compared to probes 3 and 4. This indicates an oscillating gradient along the y-axis. We calculate this magnetic field gradient using the measurements of probes 1 and 4, as shown in Fig. 14. A spectral analysis of this signal, also displayed in Fig. 14, shows how the signal clearly contains a strong component of about 1.071 kHz and a weaker component of about 1.263 kHz. These same two frequencies are found in the eddy current compensation (ecc) system of the MRI scanner. So what we see here are the remaining oscillations that the ecc system has not managed to fully compensate. Such oscillating instabilities have their origin in mechanical vibrations of the MRI scanner, excited by the strong forces from the switching gradient coils. In [47] they are described as “vibrational eddy currents”.

IV. DISCUSSION

A. Accuracy

If we assume an error-free determination of γ_0 and ν_+, then we can find B from Eq. (2) with an accuracy of 13 µT at 7 T. This is the scientific limit given by the best available data for the optical transition, and it is completely dominated by the uncertainty in γ_2.

A virtually error-free determination of γ_0 and ν_+ is however not realized, as drifts up to 0.48 MHz are observed, corresponding to about 10% of the natural linewidth of the transition. This translates to a measurement drift of 34 µT, i.e. an accuracy about 5 ppm. The initially determined γ_0 for the four probes similarly have a spread of 0.45 MHz, confirming that this is the level of accuracy achievable with the current hardware.

One possible explanation for such measurement drifts is temperature changes of the VCOs. The temperature dependence of the VCOs is reported to be up to 0.14 MHz/°C, which means that several degrees of temperature changes would significantly change the measurement. After being switched on, the rack is allowed at

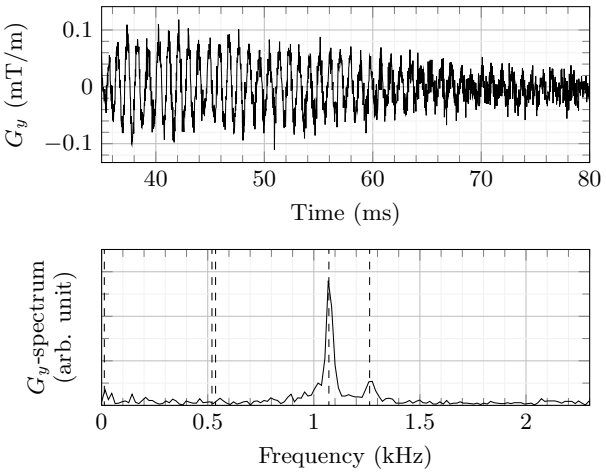

FIG. 14. Magnetic field gradient along the y-axis calculated using the measurements by probes 1 and 4, shown partly in Fig. 13. In the upper plot is shown the time domain signal starting directly after the spiral sequence has finished, and ending 45 ms later when the decaying oscillations are no longer visible. In the lower plot is shown the corresponding spectrum. The dashed lines shows the known oscillations that the ecc system tries to compensate.

least an hour to warm up, and settle on a temperature before measurements, for this reason.

A second explanation for drifts is associated with the laser-frequency stabilization. In the absorption spectrum, the saturation peak of the reference is located at a sloped background due to the other Doppler-broadened nearby hyperfine transitions. This means that the zero-crossing of the (FM spectroscopy) error signal is shifted to a higher frequency. This also means that the zero-crossing depends on the optical probe power, so small power fluctuations from e.g. fiber couplings will cause fluctuations in the laser frequency. The laser frequency is locked slightly above the zero-crossing, for this reason, but the effect cannot be completely eliminated, for larger power fluctuations.

A third explanation is that etalon fringes created by reflective surfaces in the optical setup, cause slow spurious signals when the path lengths are changing due to e.g. small temperature fluctuations.

A fourth explanation is simply that the data acquisition system has drifting offsets for the voltage measurements.

Finally it should be noted that when we consider the full dynamic range of the magnetometer extra care must be taken, since carrier and higher order sidebands in probes 1–4 will probe the Doppler background, and nearby hyperfine transitions, to give small spurious signals. Similarly, light shifts from carrier and higher order sidebands might give systematic errors across the full dynamic range. This could impact the conclusions drawn from Fig. 12. To check that this is not the case, recordings where made with reduced gradient amplitudes of 75%, 50%, and 25%, which all showed similar relative nonlinearities. Future work should aim at characterizing and compensating such infidelities, to give a reliable measurement across the entire dynamic range. Alternatively, modulation frequencies ν_i of about 10 GHz (and correspondingly lower ν_0) could be employed: this would greatly reduce light shifts, and eliminate spurious signals from carrier and higher order sidebands, since the group of hyperfine transitions spans about 9 GHz [34].

All the above aside it should be noted that assigning an absolute accuracy to a prototype sensor, is a rather speculative task. The probe lock-in oscillator phase needs to be set upon each power up, and fiber couplings need regular readjustment for consistent performance. Ultimately, several highly stable plug and play devices should be manufactured and calibrated at a certified metrology lab, before a meaningful absolute accuracy can be claimed.

B. Comparison with NMR probes

The impressive line of research and innovation that started with [20, 36, 48–50] uses NMR probes for k-space trajectory correction, and MRI magnet characterization. This has evolved into a mature solution now deployed in different branches of MRI research [51–53].

This technology has the advantage of very high sensitivity and accuracy, but suffers from issues related to rf interference and short measurement pulses that are even shorter in strong gradient fields. Also NMR probes are electronically tuned for a specific field strength, and can therefore not be used for, e.g., both a 7 T scanner and a 3 T scanner.

Optical probes as described in this work, doesn't suffer from any of these problems, and could — when further developed — provide a much more convenient solution for k-space trajectory correction in MRI. The disadvantages of the optical approach is currently the lower sensitivity and accuracy, which needs to be improved.

C. Sensitivity and bandwidth limits

With the data acquisition system currently limiting the sensitivity of the magnetometer, it is clear that there is room for improvement. Future work should seek to approach and investigate the fundamental limits of this technology. Ultimately the quantum shot noise of the probing light will be an inevitable barrier. Modifications to the optical setup could perhaps bypass even this limit by using squeezed probe light [54]. After all, the task is to determine the center frequency of the optical transition, which has a natural linewidth of 5.2 MHz [42, 43]. The 3.9 µT resolution achieved in this work corresponds to an optical frequency resolution of 0.055 MHz, i.e. about 1% of the natural linewidth.

In the measurements presented here we have used a sampling rate of 40 kHz, which is slow enough that we

don't need to worry about the response time of the VCOs, and synchronization of recorded error signals and VCO voltages. We note that the upper bandwidth limit for this method will be the FM modulation frequency, which must be similar to the linewidth of the transition. This is equivalent to recognizing that measuring a magnetic-field change much faster than the 30 ns decay time [42] of the atomic transition is not possible.

V. CONCLUSION

We have presented a novel quantum sensor — the EXAAQ magnetometer. The prototype is a fairly robust and compact device, despite being the very first demonstration of this technology. We have found the resolution of the sensor to be sub-ppm, and the accuracy to be about 5 ppm. We note that this accuracy is already much better than the best commercially available Hall probes [17, 24], which are limited to around 100 ppm. We have identified a number of simple limitations in the setup, leaving straightforward opportunities for future improvements.

This type of magnetometer can be configured to work at different field strengths and the number of probes can be chosen as necessary. It can readily be used for any high-field measurement application where low interference, high sensitivity and accuracy, and high bandwidth is of importance.

We have tested the sensor in a 7 T MRI scanner and found that it already works well enough to be used as a nice tool for probing the MRI scanner. We have only shown measurements of short sequences, to make details visible, but we emphasize that a key feature of the technology is that it can measure uninterrupted, e.g. during entire MRI sequences of many minutes. While the imperfections of the MRI scanner revealed in this work are no surprise, and could also have been uncovered using calibration sequences of the MRI scanner, or external NMR probes, it should be appreciated that they have been found using a completely novel approach.

The fact that vibrational eddy currents can clearly be resolved with the prototype, highlights the potential for this technology. An updated calibration of the ecc system would likely reduce the eddy currents, but it would only be a matter of time before this calibration again would be outdated. It is also possible that eddy current characteristics depend on the temperature of the gradient coil system, and hence change during several hours of operation. With a permanently installed optical magnetic-field-monitoring system such time-consuming calibrations could in the future be unnecessary, and optimal performance of the MRI scanner would always be ensured.

VI. OUTLOOK

In the continuation of this work we will work to improve the prototype towards an even more mature device, with less drift and high fidelity across the entire dynamic range. A number of steps can be taken to improve the current design. To deal with the temperature-dependent VCOs, different solutions could be employed: temperature stabilizing the VCOs; measuring the output frequencies instead of the control voltages; or replacing the VCOs with digital synthesizers. The last two options would also remove the problem of the noisy data acquisition system, as the measured/programmed frequency would be used directly.

While on the one hand working to improve the prototype, we will also start exploring k-space trajectory correction using the measured field data. A number of technical challenges must be solved in this regard: The sampling rate should ideally be increased to a couple of hundreds of kilohertz, accurate spatial localization of the probes should be realized, and measurements should be precisely synchronized with the MRI acquisition [20, 36].

For applications beyond MRI we note that reducing the probe size should be possible, since no particular attention has been paid to miniaturization, beyond what was necessary for installation in the MRI scanner bore. Expanding the dynamic range to several teslas could be realized using modulation frequencies ν_i in the microwave range. For applications where only a very narrow dynamic range is necessary, the probe feedback can be omitted — equivalent to setting $\nu_i = 0$ — to increase the sensitivity and accuracy, and reducing complexity. It should be noted that measurements below 0.5 T could be challenging due to the high density of different transitions [34]. Optical pumping on the D_1 line could be a solution. Also, π-transitions could cause spurious signals below 1 T, for imperfect circular probe polarization, or probes not perfectly aligned with the field direction.

The data sets and scripts for the analysis and calculations underlying this work are openly available from [55].

ACKNOWLEDGMENTS

We would like to thank Rikke H. Lütge and Axel Boisen for their contributions to the electronics development, Jürgen Appel for useful suggestions on the measurement strategy, and Michal Povazan, Kristin Engel, and Paul Sanders for assisting with the MRI system. This project has received funding from the Danish Quantum Innovation Center (Qubiz)/Innovation Fund Denmark, the European Union's Horizon 2020 research and innovation programme under Grant Agreements No. 820393 and No. 787520, and Villum Fonden under a Villum Investigator Grant, Grant No. 25880. The 7 T scanner was donated by the John and Birthe Meyer Foundation and The Danish Agency for Science, Technology

and Innovation (Grant No. 0601-01370B).

[1] R. Battesti, J. Beard, S. Böser, N. Bruyant, D. Budker, S. A. Crooker, E. J. Daw, V. V. Flambaum, T. Inada, I. G. Irastorza, *et al.*, *High Magnetic Fields for Fundamental Physics*, Physics Reports **765-766**, 1 (2018).

[2] S. Roy, *Chapter 21 - Materials in a High Magnetic Field*, in *Materials Under Extreme Conditions*, edited by A. Tyagi and S. Banerjee (Elsevier, 2017) pp. 755–789.

[3] J. M. Caridad, S. R. Power, M. R. Lotz, A. A. Shylau, J. D. Thomsen, L. Gammelgaard, T. J. Booth, A.-P. Jauho, and P. Bøggild, *Conductance quantization suppression in the quantum Hall regime*, Nature Communications **9**, 659 (2018).

[4] A. G. Marshall, C. L. Hendrickson, and G. S. Jackson, *Fourier transform ion cyclotron resonance mass spectrometry: A primer*, Mass Spectrometry Reviews **17**, 1 (1998).

[5] M. V. Gorshkov, L. Paša Tolić, H. R. Udseth, G. A. Anderson, B. M. Huang, J. E. Bruce, D. C. Prior, S. A. Hofstadler, L. Tang, L.-Z. Chen, *et al.*, *Electrospray Ionization–Fourier Transform Ion Cyclotron Resonance Mass Spectrometry at 11.5 Tesla: Instrument Design and Initial Results*, Journal of the American Society for Mass Spectrometry **9**, 692 (1998).

[6] L. Bottura, G. de Rijk, L. Rossi, and E. Todesco, *Advanced Accelerator Magnets for Upgrading the LHC*, IEEE Transactions on Applied Superconductivity **22**, 4002008 (2012).

[7] L. Bottura, S. A. Gourlay, A. Yamamoto, and A. V. Zlobin, *Superconducting Magnets for Particle Accelerators*, IEEE Transactions on Nuclear Science **63**, 751 (2016).

[8] F. Savary, A. Bonito-Oliva, R. Gallix, J. Knaster, N. Koizumi, N. Mitchell, H. Nakajima, K. Okuno, and C. Sborchia, *Status Report on the Toroidal Field Coils for the ITER Project*, IEEE Transactions on Applied Superconductivity **20**, 381 (2010).

[9] Y. Zhai, D. van der Laan, P. Connolly, and C. Kessel, *Conceptual design of HTS magnets for fusion nuclear science facility*, Fusion Engineering and Design **168**, 112611 (2021).

[10] M. V. Berry and A. K. Geim, *Of flying frogs and levitrons*, European Journal of Physics **18**, 307 (1997).

[11] J. Wang, S. Wang, Y. Zeng, H. Huang, F. Luo, Z. Xu, Q. Tang, G. Lin, C. Zhang, Z. Ren, *et al.*, *The first man-loading high temperature superconducting Maglev test vehicle in the world*, Physica C: Superconductivity **378-381**, 809 (2002).

[12] U. Floegel-Delor, P. Schirrmeister, T. Riedel, R. Koenig, V. Kantarbar, M. Liebmann, and F. N. Werfel, *Mobile HTS Bulk Devices as Enabling Ton-Force Technology for Maglev Trains*, IEEE Transactions on Applied Superconductivity **29**, 1 (2019).

[13] J. H. F. Bothwell and J. L. Griffin, *An introduction to biological nuclear magnetic resonance spectroscopy*, Biological Reviews **86**, 493 (2011).

[14] P. Wikus, W. Frantz, R. Kümmerle, and P. Vonlanthen, *Commercial gigahertz-class NMR magnets*, Superconductor Science and Technology **35**, 033001 (2022).

[15] M. G. Harisinghani, A. O'Shea, and R. Weissleder, *Advances in clinical MRI technology*, Science Translational Medicine **11**, eaba2591 (2019).

[16] Y. Lvovsky, E. W. Stautner, and T. Zhang, *Novel technologies and configurations of superconducting magnets for MRI*, Superconductor Science and Technology **26**, 093001 (2013).

[17] P. Keller, *Technologies for Precision Magnetic Field Mapping*, https://www.metrolab.com/resources/downloads/, retrieved August 18, 2023.

[18] L. Bottura, *Field Measurement Methods*, https://cas.web.cern.ch/sites/default/files/lectures/bruges-2009/bottura-1.pdf (2009), retrieved September 3, 2023.

[19] J. Lenz and S. Edelstein, *Magnetic sensors and their applications*, IEEE Sensors Journal **6**, 631 (2006).

[20] N. De Zanche, C. Barmet, J. A. Nordmeyer-Massner, and K. P. Pruessmann, *NMR Probes for Measuring Magnetic Fields and Field Dynamics in MR Systems*, Magnetic Resonance in Medicine **60**, 176 (2008).

[21] Metrolab, *PT2026 Key Specifications*, https://www.metrolab.com/wp-content/uploads/2021/06/PT2026-Key-specifications-v1.2.pdf (), retrieved September 3, 2023.

[22] A. Nikiel, P. Blümler, W. Heil, M. Hehn, S. Karpuk, A. Maul, E. Otten, L. M. Schreiber, and M. Terekhov, *Ultrasensitive 3He Magnetometer for Measurements of High Magnetic Fields*, The European Physical Journal D **68**, 330 (2014).

[23] C. Barmet, B. J. Wilm, M. Pavan, G. Katsikatsos, J. Keupp, G. Mens, and K. Pruessmann, *Concurrent Higher-Order Field Monitoring for Routine Head MRI: An Integrated Heteronuclear Setup*, Proc. Intl. Soc. Mag. Reson. Med. 18 , 216 (2010).

[24] Senis, *3MH6-E TESLAMETER*, https://www.senis.swiss/wp-content/uploads/2023/04/DS.200.3MH6-E-TESLAMETER_Rev2.2.pdf, retrieved September 4, 2023.

[25] J. O. Pedersen, C. G. Hanson, R. Xue, and L. G. Hanson, *Inductive Measurement and Encoding of k-space Trajectories in MR Raw Data*, Magnetic Resonance Materials in Physics, Biology and Medicine **32**, 655 (2019).

[26] M. Adaikkan, Y. Ma, U. Walach, M. Bochard, F. Bechtold, G. Vayakis, M. Walsh, M. P. C. Lino, and G. Counsell, *Producing High Quality LTCC Sensors for ITER In-Vessel Magnetic Diagnostics*, Fusion Engineering and Design **184**, 113316 (2022).

[27] Metrolab, *FDI2056 The First Off-The-Shelf Instrument to Quantify Magnetic Field Transients*, https://www.metrolab.com/wp-content/uploads/2019/06/FDI2056_V4.pdf (), retrieved September 4, 2023.

[28] D. Nakamura, H. Sawabe, Y. H. Matsuda, and S. Takeyama, *Precise Measurement of a Magnetic Field Generated by the Electromagnetic Flux Compression Technique*, Review of Scientific Instruments **84**, 044702 (2013).

[29] S. Tsuji-lio, T. Akiyama, E. Sato, T. Nozawa, H. Tsutsui, R. Shimada, M. Takahashi, and K. Terai, *Fiberoptic Heterodyne Magnetic Field Sensor for Long-Pulsed Fusion Devices*, Review of Scientific Instruments **72**, 413 (2001).

[30] S. George, N. Bruyant, J. Béard, S. Scotto, E. Arimondo, R. Battesti, D. Ciampini, and C. Rizzo, *Pulsed High Magnetic Field Measurement with a Rubidium Vapor Sensor*, Rev. Sci. Instrum. **88**, 073102 (2017).

[31] D. Ciampini, R. Battesti, C. Rizzo, and E. Arimondo, *Optical Spectroscopy of a Microsized Rb Vapor Sample in Magnetic Fields up to 58 T*, Phys. Rev. A **96**, 052504 (2017).

[32] J. Keaveney, F. S. Ponciano-Ojeda, S. M. Rieche, M. J. Raine, D. P. Hampshire, and I. G. Hughes, *Quantitative Optical Spectroscopy of* ^{87}*Rb Vapour in the Voigt Geometry in DC Magnetic Fields up to 0.4 T*, J. Phys. B: At. Mol. Opt. Phys **52**, 055003 (2019).

[33] E. Klinger, H. Azizbekyan, A. Sargsyan, C. Leroy, D. Sarkisyan, and A. Papoyan, *Proof of the Feasibility of a Nanocell-Based Wide-Range Optical Magnetometer*, Appl. Opt. **59**, 2231 (2020).

[34] H. Stærkind, K. Jensen, J. H. Müller, V. O. Boer, E. T. Petersen, and E. S. Polzik, *Precision Measurement of the Excited State Landé g-factor and Diamagnetic Shift of the Cesium* D_2 *Line*, Phys. Rev. X **13**, 021036 (2023).

[35] M. Bräuer and M. Budde, *Vorrichtung und Verfahren zur Magnetfeldmessung und -regelung - DE102012202237B4* (2012).

[36] C. Barmet, N. D. Zanche, and K. P. Pruessmann, *Spatiotemporal Magnetic Field Monitoring for MR*, Magnetic Resonance in Medicine **60**, 187 (2008).

[37] E. J. Strait, E. D. Fredrickson, J.-M. Moret, and M. Takechi, *Chapter 2: Magnetic Diagnostics*, Fusion Science and Technology **53**, 304 (2008).

[38] A. Quercia, A. Pironti, I. Bolshakova, R. Holyaka, I. Duran, A. Murari, and J. Contributors, *Long Term Operation of the Radiation-Hard Hall Probes System and the Path Toward a High Performance Hybrid Magnetic Field Sensor*, Nuclear Fusion **62**, 106032 (2022).

[39] M. Marchevsky, *Quench Detection and Protection for High-Temperature Superconductor Accelerator Magnets*, Instruments **5**, 27 (2021).

[40] O. Schmidt, K.-M. Knaak, R. Wynands, and D. Meschede, *Cesium Saturation Spectroscopy Revisited: How to Reverse Peaks and Observe Narrow Resonances*, Applied Physics B **59**, 167 (1994).

[41] G. C. Bjorklund, M. D. Levenson, W. Lenth, and C. Ortiz, *Frequency Modulation (FM) Spectroscopy*, Applied Physics B **32**, 145 (1983).

[42] L. Young, W. T. Hill, S. J. Sibener, S. D. Price, C. E. Tanner, C. E. Wieman, and S. R. Leone, *Precision Lifetime Measurements of Cs 6p* $^2P_{1/2}$ *and 6p* $^2P_{3/2}$ *Levels by Single-Photon Counting*, Phys. Rev. A **50**, 2174 (1994).

[43] D. Steck, *Cesium D Line Data*, `https://steck.us/alkalidata/cesiumnumbers.pdf` (2023), retrieved September 5, 2023.

[44] M. A. Bernstein, K. F. King, and X. J. Zhou, *Handbook of MRI Pulse Sequences* (Elsevier Academic Press, 2004).

[45] E. Tiesinga, P. J. Mohr, D. B. Newell, and B. N. Taylor, *CODATA Recommended Values of the Fundamental Physical Constants: 2018*, Rev. Mod. Phys. **93**, 025010 (2021).

[46] M. Markl, R. Bammer, M. Alley, C. Elkins, M. Draney, A. Barnett, M. Moseley, G. Glover, and N. Pelc, *Generalized Reconstruction of Phase Contrast MRI: Analysis and Correction of the Effect of Gradient Field Distortions*, Magnetic Resonance in Medicine **50**, 791 (2003).

[47] S. A. Winkler, F. Schmitt, H. Landes, J. de Bever, T. Wade, A. Alejski, and B. K. Rutt, *Gradient and Shim Technologies for Ultra High Field MRI*, NeuroImage **168**, 59 (2018).

[48] C. Barmet, N. De Zanche, B. J. Wilm, and K. P. Pruessmann, *A Transmit/Receive System for Magnetic Field Monitoring of In Vivo MRI*, Magnetic Resonance in Medicine **62**, 269 (2009).

[49] B. J. Wilm, C. Barmet, M. Pavan, and K. P. Pruessmann, *Higher Order Reconstruction for MRI in the Presence of Spatiotemporal Field Perturbations*, Magnetic Resonance in Medicine **65**, 1690 (2011).

[50] S. J. Vannesjo, B. J. Wilm, Y. Duerst, S. Gross, D. O. Brunner, B. E. Dietrich, T. Schmid, C. Barmet, and K. P. Pruessmann, *Retrospective Correction of Physiological Field Fluctuations in High-field Brain MRI Using Concurrent Field Monitoring*, Magnetic Resonance in Medicine **73**, 1833 (2015).

[51] E. Versteeg, D. W. J. Klomp, and J. C. W. Siero, *Accelerating Brain Imaging Using a Silent Spatial Encoding Axis*, Magnetic Resonance in Medicine **88**, 1785 (2022).

[52] N. Boulant, L. Quettier, G. Aubert, A. Amadon, J. Belorgey, C. Berriaud, C. Bonnelye, P. Bredy, E. Chazel, G. Dilasser, *et al.*, *Commissioning of the Iseult CEA 11.7 T Whole-body MRI: Current Status, Gradient-magnet Interaction Tests and First Imaging Experience*, Magnetic Resonance Materials in Physics, Biology and Medicine **36**, 175 (2023).

[53] S. Feizollah and C. L. Tardif, *High-resolution Diffusion-weighted Imaging at 7 Tesla: Single-shot Readout Trajectories and Their Impact on Signal-to-noise Ratio, Spatial Resolution and Accuracy*, NeuroImage **274**, 120159 (2023).

[54] E. S. Polzik, J. Carri, and H. J. Kimble, *Spectroscopy with Squeezed Light*, Phys. Rev. Lett. **68**, 3020 (1992).

[55] H. Stærkind, *Data underlying: High-Field Optical Cesium Magnetometer for Magnetic Resonance Imaging*, `https://doi.org/10.5281/zenodo.8366717` (2023).

7 Construction of the Prototype

A major focus, and a prerequisite for working with the magnetometer in a hospital setting, has been the construction of a robust and compact prototype. The prototype is shown in Fig. 5 of Ref. [2] (page 80 in this thesis). In Fig. 7.1 we show a zoomed-in view of this figure, highlighting the integrated modules that we have made ourselves. The probe-EOM module, the probe-VCO module, and the probe-feedback module are 1-rack-unit chassis. The five photodetectors and the five heating lasers are Eurocard-size PCBs mounted in a 3-rack-units subrack. The probe-laser module is a 3-rack-units chassis. For all the modules we have designed front panels with user-friendly and descriptive engravings and mounting holes for interface components.

One of the five heating lasers is shown in Fig. 7.2. The front panel has an optical output, an on/off switch, a display showing the laser diode current, a trimming potentiometer to adjust the current, and a connector for electrical control of the current (not in use). The heating lasers are powered by ± 5 V power supplies installed in the subrack.

One of the five photodetectors is shown in Fig. 7.3. The front panel has an optical input, a trimming potentiometer to adjust the output gain, and a connector for the rf signal output. The detectors are powered by ± 15 V power supplies installed in the subrack.

The probe-feedback module is shown in Fig. 7.4. The front panel has, for each of the four probes, an rf input (for the photodetector signal), an error-signal output, a control voltage output, a switch for enabling the feedback, a switch for enabling a control-voltage offset, and a switch for enabling a control voltage scan. In addition to this, there is a common rf

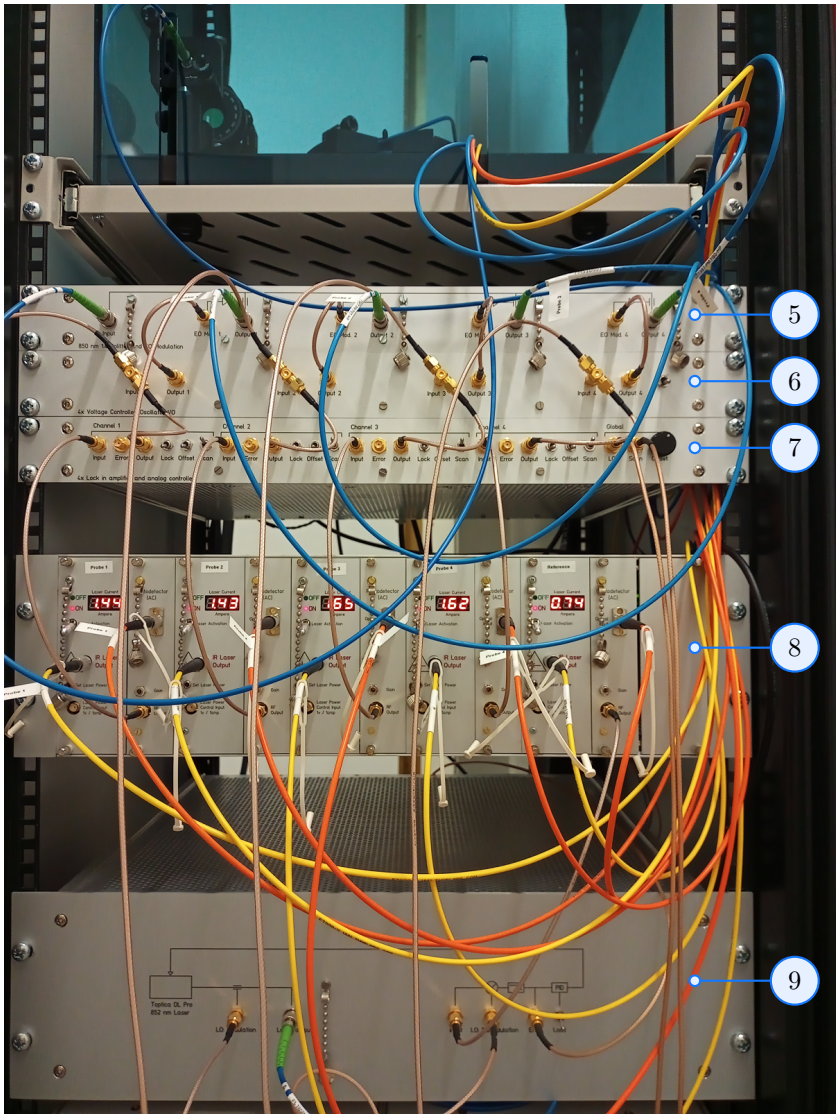

Figure 7.1: EXAAQ magnetometer prototype integrated modules. Labels are chosen to be consistent with Fig. 5 of Ref. [2] (page 80 in this thesis). 5: Probe-EOM module. 6: Probe-VCO module. 7: Probe-feedback module. 8: Subrack with photodetectors and heating lasers. 9: Probe-laser module.

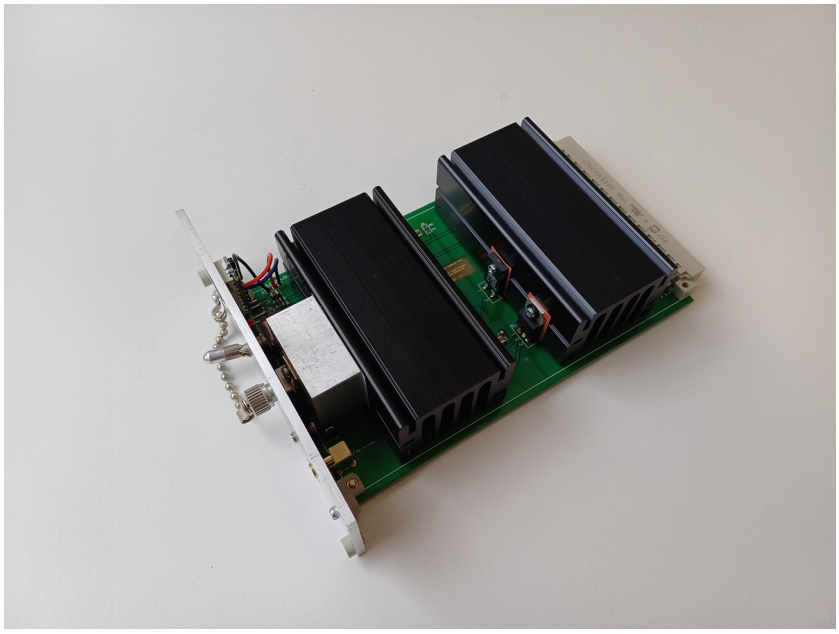

Figure 7.2: Heating laser.

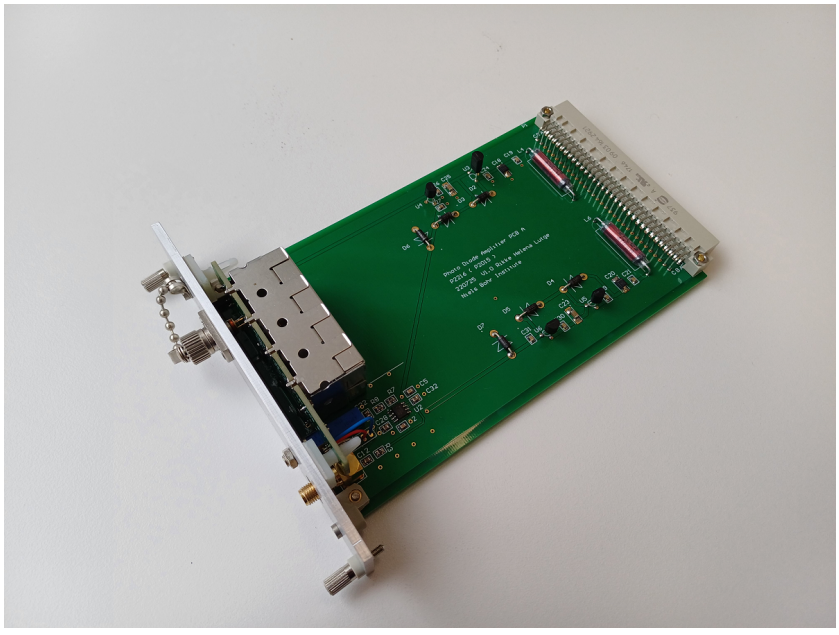

Figure 7.3: Photodetector.

input for the lock-in amplifiers, a common input for the control voltage scan, and a potentiometer for a common control-voltage offset. It contains four analog lock-in amplifiers, four op-amp summation amplifiers, and four op-amp integrators. The lock-in amplifiers are passive, and the op-amp circuits are powered by ±15 V power supplies, also mounted in the chassis.

The probe-VCO module is shown in Fig. 7.5. The front panel has four control-voltage inputs, four rf outputs, and an on/off switch. It contains four VCOs, outputing about 9 dBm of power, each with a 3 dB fixed attenuator reducing the output power to about 6 dBm. The VCOs are powered by a 5 V power supply, also mounted in the chassis.

The probe-EOM module is shown in Fig. 7.6. The front panel has one optical probe-light input, four optical outputs — one for each probe, and four rf inputs for the EOM drive signals. It contains a 1x4 fiber splitter, which distributes probe light to the four probe EOMs. The input rf signals of about 6 dBm are attenuated by 15 dB fixed attenuators and amplified by 26 dB amplifiers, for a final 17 dBm EOM drive power. This rf power optimizes the optical power for the first sidebands. The four amplifiers are mounted on heatsinks, and holes are cut in the chassis to allow air to flow. The amplifiers are powered by a 15 V power supply, also mounted in the chassis.

The probe-laser module is shown in Fig. 7.7. The front panel has, on the left side, an optical output and an rf input for driving $\mathrm{EOM_{FM}}$. On the right side are an rf input (for the photodetector signal), an rf input for the lock-in amplifier, an error-signal output, and a switch for enabling the reference feedback. It contains the probe laser, $\mathrm{EOM_{FM}}$, a lock-in amplifier, and an integrator. The integrator is powered with wires from the probe-feedback chassis.

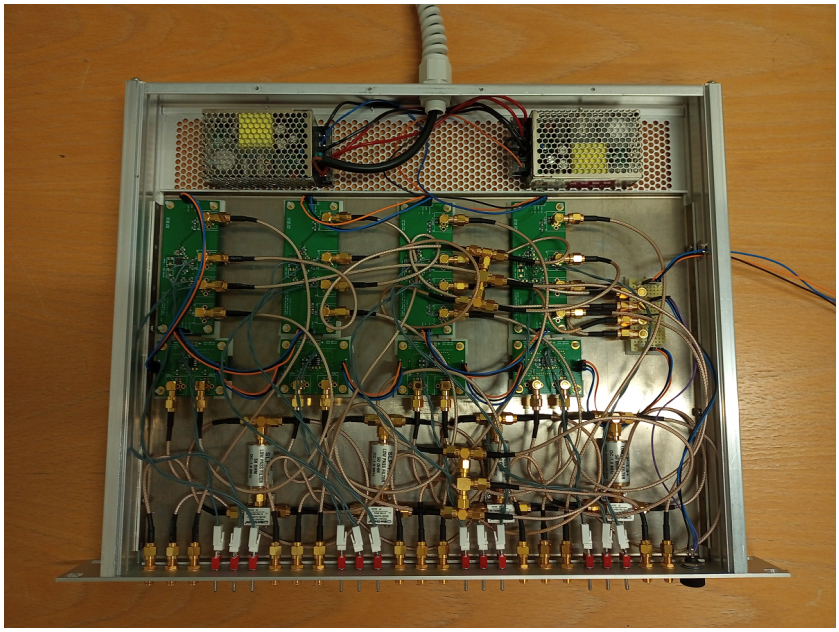

Figure 7.4: Probe-feedback module: Four lock-in amplifiers, four summation amplifiers, four integrators, and two power supplies.

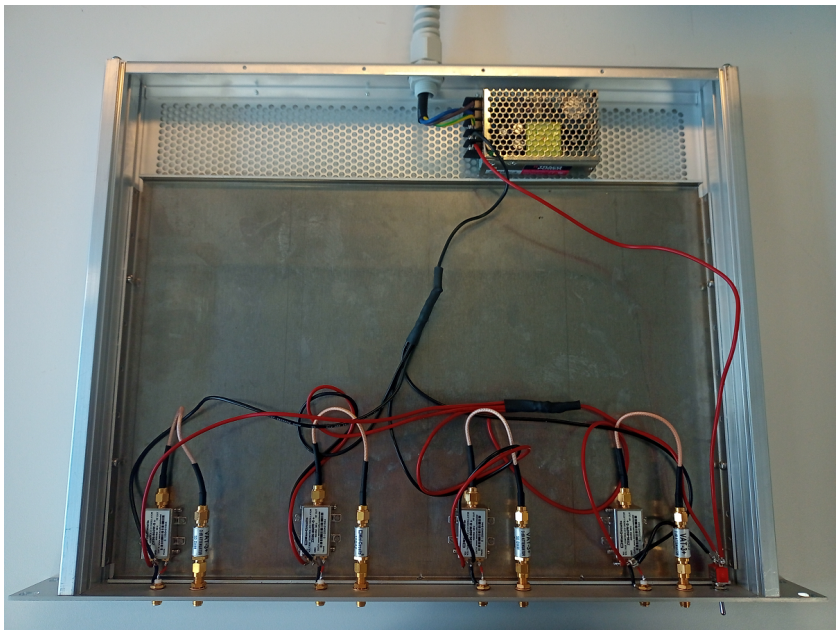

Figure 7.5: Probe-VCO module: Four VCOs, four fixed attenuators, and a power supply.

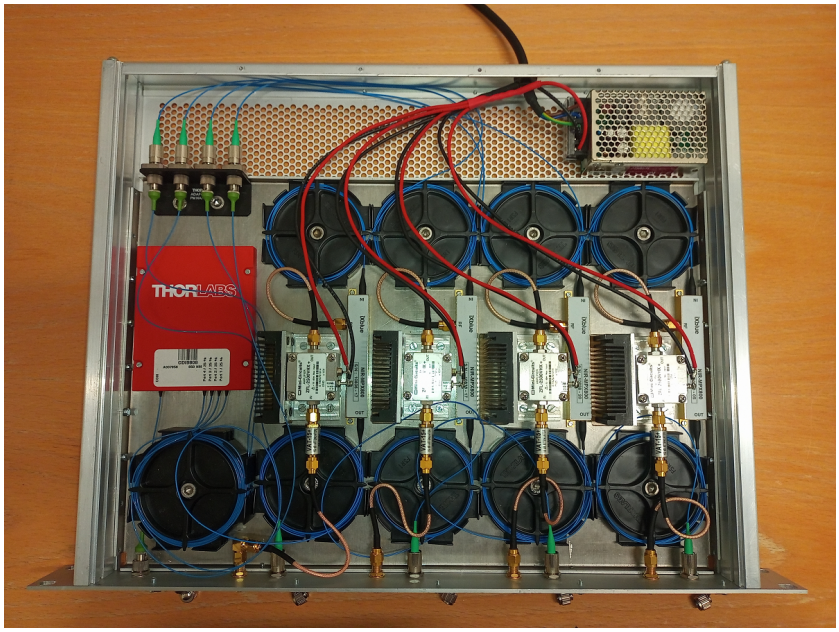

Figure 7.6: Probe-EOM module: 1x4 fiber splitter, four fixed attenuators, four amplifiers, four EOMs, and a power supply.

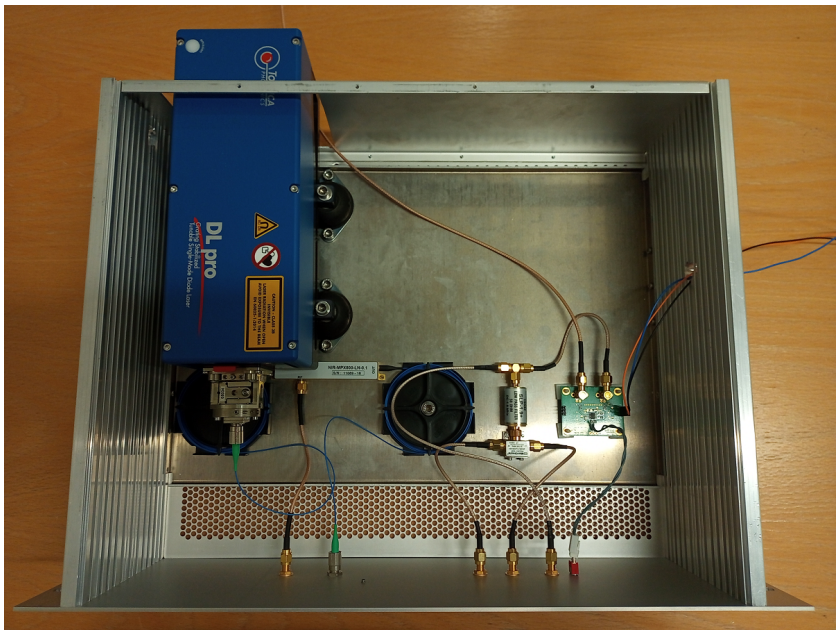

Figure 7.7: Probe-laser module: Probe laser, $\mathrm{EOM_{FM}}$, lock-in amplifier, and integrator.

8 The Sub-Tesla Regime

The use of EXAAQ magnetometry below 1 T, will have to deal with spurious signals as mentioned in Section VI of Ref. [2] (page 85 in this thesis). In Fig. 8.1 we show the transition from the Zeeman regime to the Paschen-Back regime, with both σ_+ and π-transitions displayed on top of the experimental data already presented as Fig. 18 in Ref. [1] (page 70 in this thesis). We see that only above 1 T is the extreme transition free from interference from π-transitions. So, for measurements below 1 T we will see spurious signals, if the probe is not perfectly aligned with the field direction. We also have weak σ_- transitions at approximately the same frequencies as the rightmost seven π-transitions in Fig. 8.1. These could similarly cause spurious signals, if the probe light is (very) imperfectly σ_+-polarized. For this reason, it is fair to say that EXAAQ magnetometry does not work as well below 1 T, as it does above.

With good field alignment of the probe and good σ_+-polarization, measurements below 1 T could work reasonably well. Below 0.5 T we see that the Doppler background of the neighbouring hyperfine transition significantly overlaps with the extreme transition. This will similarly disturb the measurement. This could be accounted for through a mapping of the effect, possibly extending the working range down towards 0.1 T.

It should be noted that the accuracy and sensitivity, is primarily given by the linewidth, and as such is not a relative number. So, where a 4 µT sensitivity is less than 1 ppm at 7 T, it will be 4 ppm at 1 T. I.e. the relative performance will depend on the field strength.

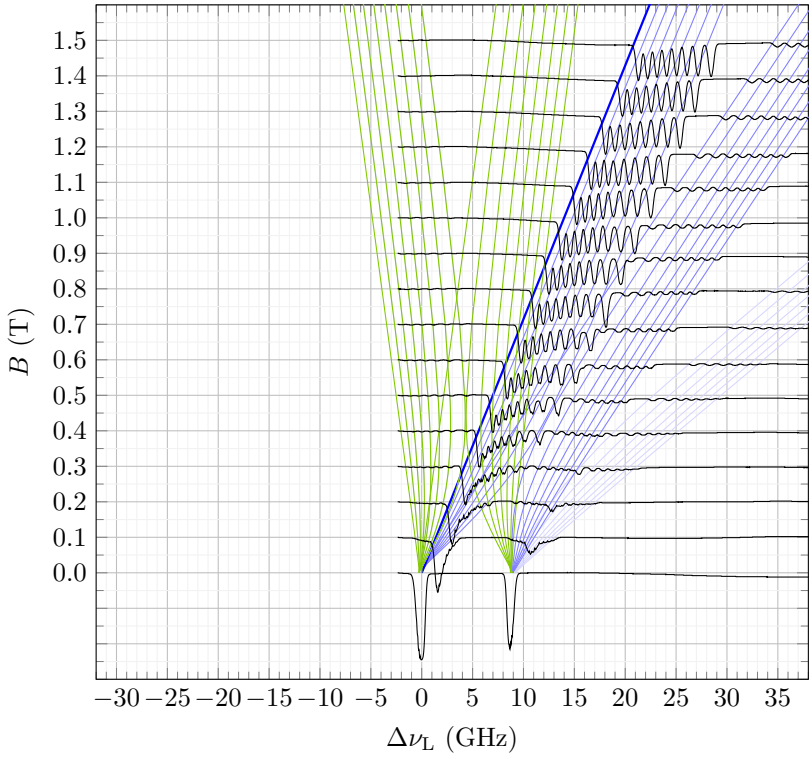

Figure 8.1: A reproduction of Fig. 18 from Ref. [1] (page 70 in this thesis) with π-transitions in green, along with the σ_+ transitions in blue, also shown originally. We see that only above 1 T is the extreme angular-momentum transition nicely isolated.

9 Conclusion and Outlook

In this work I have presented a new optical method for measuring high magnetic fields: the EXAAQ magnetometry technique. The theoretical background has been described, i.e. that the extreme σ_+-transition has a simple quadratic dependence on the magnetic field. An experiment to determine this field dependence has been carried out and presented. A prototype of this technology has been constructed, described, and characterized — and measurements on a 7 T MRI scanner have been performed. These experiments have demonstrated that EXAAQ magnetometry can provide sensitivity and accuracy in the ppm-range, and also that this is enough to detect instabilities in the 7 T scanner.

In many ways the EXAAQ magnetometer compares favorably to conventional solutions for measuring fields of several teslas: The fiber-optic cables and probes are completely non-metallic, the sensitivity and accuracy is high, it works well in magnetic-field gradients, and the sampling rate is fast. These promising features, along with the potentially meaningful application in MRI, make further investigations seem very much worthwhile.

Future work should first and foremost aim to demonstrate an improved stability and sensitivity of the EXAAQ technique. Image improvements seem to be within reach, as it seems feasible to drive the measurement errors below the detected scanner instabilities in the near future. This will be the tipping point, where a reconstruction based on the measured k-space trajectory will be better than a reconstruction based on the nominal trajectory. It should be noted that optimizing the normalized signal, as is done in Section 3.4, makes sense in the

case where spurious signals, from e.g. etalon fringes, are the dominating noise source, since these errors will scale proportionally with the probing power. For other noise sources, which are independent of the probing power, or are sub-linear in the probing power, the normalized signal may not be the best quantity to optimize. Also, varying other parameters, such as probe-filter transmission, FM-modulation frequency and amplitude, detector gain and Q-factor, etc. should be considered. Ultimately, the optimization problem that must be solved to find the best performance of an EXAAQ magnetometer is a pretty complicated one. For the results presented in Ref. [2], the chosen parameters are largely based on quick tests, qualified guesses, availability of components, and stability of operation. Thus, contributing to the conclusion that there is room for improvement in future designs.

MRI is itself an involved subject, and the brief introduction given in Section 1.2, does not do justice to its complexity. So, when an improved EXAAQ system has been demonstrated there will be a lot of work in figuring out the way to best use this new technology. For which MRI methods and sequences can advantages be demonstrated? Do the advantages justify the complexity and the extra costs? Should new sequences be developed? Is reduced scan time or improved image quality a goal? Could the demands for the gradient coil system be reduced, to make it (significantly) cheaper? How can the mechanical integration of the probes be implemented, such that not too much extra time needs to be spent on installation for each new scan? With the Skope system now deployed in different branches of the MRI research community as a well-known solution, other people are already looking into these questions, albeit with a different system. The results coming out of this work will also be able to guide future MRI research based on EXAAQ magnetometry. At some point a direct comparison of the EXAAQ method and the Skope NMR method would be obvious.

Currently, there is a rather large focus on the commercialization of quantum technologies — politically, from investors, and at the universities — and it is in fact natural to consider a commercialization of

this technology. Perhaps the best and fastest way to explore the possible applications in MRI, is indeed to make the technology available to the MRI research community as a mature commercial solution. Not an end-user-ready MRI solution, but rather a magnetometry solution. The development of a more widely accessible solution, not just for the technically skilled MRI researchers, but also for those of e.g. medical training, would then be a next step. The ultimate goal will of course be to go beyond MRI research, and all the way to the clinic, where faster, better, or cheaper diagnostics would truly benefit people and society.

The strongest operational MRI system in the world is currently the 11.7 T Iseult CEA whole-body scanner in France [46]. As of this writing the first in vivo studies are being carried out, but images have not yet been released [47]. The construction of a 14 T system has recently been agreed upon and will be built in the Netherlands [48, 49]. We note that the current magnetometer prototype should in fact be able to work readily at 14 T. As long as any future magnet development is accompanied by corresponding rf and EOM hardware development the presented implementation of EXAAQ magnetometry will remain feasible. In general, it does not seem like 7 T or higher-field MRI systems will become standard in the near future, and scanner magnets of more than 10 T will likely remain exotic medical research instruments for the next couple of decades [50].

The development of new technology tends to follow unpredictable paths, and we can only guess what will happen in the future. It is easy to come up with reasons why something will not work, will not be useful, or will not be worth it. But if we never try, then we will never know.

10 Acknowledgements

The last six years have been a journey, that I would never have dreamed of. Even though I have worked a lot on my own, I would never have been able to do this alone, and I am very grateful to many people.

Thank you, Eugene, Esben, Vincent, and Kasper, for making this whole project come together. For guiding me and gently pushing me in the right direction, while also trusting me to make my own decisions, work in my own way, and at my own pace. Thank you, Jörg, for being a mentor in experimental atomic physics, always available for technical discussions and sharing your insights.

Eugene — thank you for your support and encouragement during the years. For creating an amazing and creative research environment. For your warm leadership, and for always being available for a talk.

Thank you, Susanne, for being my partner through all this. For helping me make smart decisions. For helping me breathe in stressful situations and see the bigger picture. For celebrating victories with me — and for reminding me to relax and enjoy the two wonderful kids that we got on the way.

Thank you, Mom and Dad, for making me who I am today, and for still cheering me on. For sparking my interest in research, science and technology. For showing me that if you want something done really well, the best way is sometimes to get your hands dirty and do it yourself. Thank you, Søren, for being there all along the way, having fun with me, and challenging me in everything from sports to strategic games, and dressing well.

Thank you, to all the amazing teachers that I have had since high school, during my physics studies at NBI, and my MRI studies at DTU. It has all been world-class! Thank you, to all my current and former

colleagues at NBI and DRCMR, for interesting and helpful discussions and great company every day when I come to work. Thank you, Rebecca, for also carefully reading and commenting on both papers.

Esben — despite fighting a terminal disease, you were always smiling and encouraging me. Your optimism and enthusiasm for our work were my main motivation to keep going — whenever I got something to work, you were the one I was looking forward to telling the most. I will always remember your positive attitude, and I will continue to let it be an inspiration for me in the future!

Bibliography

[1] H. Stærkind, K. Jensen, J. H. Müller, V. O. Boer, E. T. Petersen, and E. S. Polzik. *Precision Measurement of the Excited State Landé g-factor and Diamagnetic Shift of the Cesium* D_2 *Line*. *Phys. Rev. X*, 13:021036, 2023. doi:10.1103/PhysRevX.13.021036.

[2] H. Stærkind, K. Jensen, J. H. Müller, V. O. Boer, E. S. Polzik, and E. T. Petersen. *High-Field Optical Cesium Magnetometer for Magnetic Resonance Imaging*. *arXiv (2309.12006)*, 2023. doi:10.48550/arXiv.2309.12006.

[3] H. Stærkind. *Data underlying: Precision Measurement of the Excited State Lande g-factor and Diamagnetic Shift of the Cesium D2 Line*, 2023. doi:10.5281/zenodo.7189170.

[4] H. Stærkind. *Data underlying: High-Field Optical Cesium Magnetometer for Magnetic Resonance Imaging*, 2023. doi:10.5281/zenodo.8366717.

[5] L. G. Hanson. *Introduction to Magnetic Resonance Imaging Techniques*. https://eprints.drcmr.dk/37/1/MRI_English_a4.pdf, 2009. Retrieved September 26, 2023.

[6] D. G. Nishimura. *Principles of Magnetic Resonance Imaging*. Lulu.com, 2016.

[7] M. A. Bernstein, K. F. King, and X. J. Zhou. *Handbook of MRI Pulse Sequences*. Elsevier Academic Press, 2004.

[8] P. Mansfield and B. Chapman. *Active Magnetic Screening of Coils for Static and Time-Dependent Magnetic Field Generation in NMR Imaging. Journal of Physics E: Scientific Instruments*, 19:540, 1986. doi:10.1088/0022-3735/19/7/008.

[9] P. Jehenson, M. Westphal, and N. Schuff. *Analytical Method for the Compensation of Eddy-Current Effects Induced by Pulsed Magnetic Field Gradients in NMR Systems. Journal of Magnetic Resonance (1969)*, 90:264–278, 1990. doi:10.1016/0022-2364(90)90133-T.

[10] J. J. Van Vaals and A. H. Bergman. *Optimization of Eddy-Current Compensation. Journal of Magnetic Resonance (1969)*, 90:52–70, 1990. doi:10.1016/0022-2364(90)90365-G.

[11] C. Barmet, N. De Zanche, and K. P. Prüssmann. *Spatiotemporal Magnetic Field Monitoring for MR. Magnetic Resonance in Medicine*, 60:187–197, 2008. doi:10.1002/mrm.21603.

[12] N. De Zanche, C. Barmet, J. A. Nordmeyer-Massner, and K. P. Prüssmann. *NMR Probes for Measuring Magnetic Fields and Field Dynamics in MR Systems. Magnetic Resonance in Medicine*, 60:176–186, 2008. doi:10.1002/mrm.21624.

[13] B. J. Wilm, C. Barmet, M. Pavan, and K. P. Prüssmann. *Higher Order Reconstruction for MRI in the Presence of Spatiotemporal Field Perturbations. Magnetic Resonance in Medicine*, 65:1690–1701, 2011. doi:10.1002/mrm.22767.

[14] J. Ruiz-Cabello, B. P. Barnett, P. A. Bottomley, and J. W. M. Bulte. *Fluorine (19F) MRS and MRI in Biomedicine. NMR in Biomedicine*, 24:114–129, 2011. doi:10.1002/nbm.1570.

[15] Skope. *About Us*. https://skope.swiss/about-us/. Visited September 26, 2023.

[16] S. J. Vannesjo, B. J. Wilm, Y. Duerst, S. Gross, D. O. Brunner, B. E. Dietrich, T. Schmid, C. Barmet, and K. P. Prüssmann. *Retrospective Correction of Physiological Field Fluctuations in High-field*

Brain MRI Using Concurrent Field Monitoring. Magnetic Resonance in Medicine, 73:1833–1843, 2015. doi:10.1002/mrm.25303.

[17] B. J. Wilm, C. Barmet, S. Gross, L. Kasper, S. J. Vannesjo, M. Haeberlin, B. E. Dietrich, D. O. Brunner, T. Schmid, and K. P. Prüssmann. *Single-Shot Spiral Imaging Enabled by an Expanded Encoding Model: Demonstration in Diffusion MRI. Magnetic Resonance in Medicine*, 77:83–91, 2017. doi:10.1002/mrm.26493.

[18] K. M. Gilbert, P. I. Dubovan, J. S. Gati, R. S. Menon, and C. A. Baron. *Integration of an RF Coil and Commercial Field Camera for Ultrahigh-Field MRI. Magnetic Resonance in Medicine*, 87:2551–2565, 2022. doi:10.1002/mrm.29130.

[19] P. Zeeman. *The Effect of Magnetisation on the Nature of Light Emitted by a Substance. Nature*, 55:347–347, 1897. doi:10.1038/055347a0.

[20] C. J. Foot. *Atomic physics*. Oxford University Press, 2012.

[21] J. C. del Toro Iniesta. *On the Discovery of the Zeeman Effect on the Sun and in the Laboratory. Vistas in Astronomy*, 40:241 – 256, 1996. doi:10.1016/0083-6656(96)00005-0.

[22] E. Arimondo, M. Inguscio, and P. Violino. *Experimental Determinations of the Hyperfine Structure in the Alkali Atoms. Rev. Mod. Phys.*, 49:31–75, 1977. doi:10.1103/RevModPhys.49.31.

[23] E. Arimondo, D. Ciampini, and C. Rizzo. *Chapter One - Spectroscopy of Natural and Artificial Atoms in Magnetic Fields. Advances In Atomic, Molecular, and Optical Physics*, 65:1 – 66, 2016. doi:10.1016/bs.aamop.2016.02.001.

[24] D. Griffiths and D. F. Schroeter. *Introduction to Quantum Mechanics*. Cambridge University Press, 2018.

[25] W. B. Garn, R. S. Caird, D. B. Thomson, and C. M. Fowler. *Technique for Measuring Megagauss Magnetic Fields Using Zee-*

man Effect. Rev. Sci. Instrum., 37:762–767, 1966. doi:10.1063/1.1720316.

[26] M. R. Gomez, S. B. Hansen, K. J. Peterson, D. E. Bliss, A. L. Carlson, D. C. Lamppa, D. G. Schroen, and G. A. Rochau. *Magnetic Field Measurements via Visible Spectroscopy on the Z Machine. Rev. Sci. Instrum.*, 85:11E609, 2014. doi:10.1063/1.4891304.

[27] J. T. Banasek, J. T. Engelbrecht, S. A. Pikuz, T. A. Shelkovenko, and D. A. Hammer. *Measuring 10-20 T Magnetic Fields in Single Wire Explosions Using Zeeman Splitting. Rev. Sci. Instrum.*, 87(10):103506, 2016. doi:10.1063/1.4965836.

[28] J. T. Banasek, J. T. Engelbrecht, S. A. Pikuz, T. A. Shelkovenko, and D. A. Hammer. *Measuring 20-100 T B-Fields Using Zeeman Splitting of Sodium Emission Lines on a 500 kA Pulsed Power Machine. Rev. Sci. Instrum.*, 87:11D407, 2016. doi:10.1063/1.4958912.

[29] J. Keaveney, F. S. Ponciano-Ojeda, S. M. Rieche, M. J. Raine, D. P. Hampshire, and I. G. Hughes. *Quantitative Optical Spectroscopy of ^{87}Rb Vapour in the Voigt Geometry in DC Magnetic Fields up to 0.4 T. J. Phys. B: At. Mol. Opt. Phys*, 52:055003, 2019. doi:10.1088/1361-6455/ab0186.

[30] E. Klinger, H. Azizbekyan, A. Sargsyan, C. Leroy, D. Sarkisyan, and A. Papoyan. *Proof of the Feasibility of a Nanocell-Based Wide-Range Optical Magnetometer. Appl. Opt.*, 59:2231–2237, 2020. doi:10.1364/AO.373949.

[31] F. S. Ponciano-Ojeda, F. D. Logue, and I. G. Hughes. *Absorption Spectroscopy and Stokes Polarimetry in a 87Rb Vapour in the Voigt Geometry with a 1.5 T External Magnetic Field. Journal of Physics B: Atomic, Molecular and Optical Physics*, 54:015401, 2020. doi:10.1088/1361-6455/abc7ff.

[32] S. George, N. Bruyant, J. Béard, S. Scotto, E. Arimondo, R. Battesti, D. Ciampini, and C. Rizzo. *Pulsed High Magnetic Field*

Measurement with a Rubidium Vapor Sensor. *Rev. Sci. Instrum.*, 88:073102, 2017. doi:10.1063/1.4993760.

[33] D. Ciampini, R. Battesti, C. Rizzo, and E. Arimondo. *Optical Spectroscopy of a Microsized Rb Vapor Sample in Magnetic Fields up to 58 T*. *Phys. Rev. A*, 96:052504, 2017. doi:10.1103/PhysRevA.96.052504.

[34] D. Steck. *Cesium D Line Data*. https://steck.us/alkalidata/cesiumnumbers.pdf, 2023. Retrieved September 29, 2023.

[35] J. Abele, M. Baumann, and W. Hartmann. *g_J-Factors and Magnetic HFS Interaction Constants in the $6^2P_{3/2}$- and $8^2P_{3/2}$-states of ^{133}Cs*. *Physics Letters A*, 51:169–170, 1975. doi:10.1016/0375-9601(75)90216-9.

[36] H. Bucka. *Introductory Paper On Hanle Effect, Level Crossing And Double Resonance Experiments*. *Journal de Physique Colloques*, 30:C1–3–C1–9, 1969. doi:10.1051/jphyscol:1969101.

[37] M. Allegrini, E. Arimondo, and L. A. Orozco. *Survey of Hyperfine Structure Measurements in Alkali Atoms*. *Journal of Physical and Chemical Reference Data*, 51:043102, 2022. doi:10.1063/5.0098061.

[38] O. Schmidt, K.-M. Knaak, R. Wynands, and D. Meschede. *Cesium Saturation Spectroscopy Revisited: How to Reverse Peaks and Observe Narrow Resonances*. *Applied Physics B*, 59:167–178, 1994. doi:10.1007/BF01081167.

[39] E. Hecht. *Optics*. Pearson Education Inc., publishing as Addison Wesley, 2002.

[40] D. V. Schroeder. *Thermal Physics*. Addison Wesley Longman, 2000.

[41] M. C. Wapler, J. Leupold, I. Dragonu, D. von Elverfeld, M. Zaitsev, and U. Wallrabe. *Magnetic Properties of Materials for MR Engi-*

neering, Micro-MR and Beyond. Journal of Magnetic Resonance, 242:233–242, 2014. doi:10.1016/j.jmr.2014.02.005.

[42] J. G. Bouwman and C. J. G. Bakker. *Alias Subtraction more Efficient than Conventional Zero-Padding in the Fourier-Based Calculation of the Susceptibility Induced Perturbation of the Magnetic Field in MR. Magnetic Resonance in Medicine*, 68:621–630, 2012. doi:10.1002/mrm.24343.

[43] J. G. Bouwman. *Forward Field-Shift Calculation for MRI.* https://www.mathworks.com/matlabcentral/fileexchange/37278-forward-field-shift-calculation-for-mri, 2014. Retrieved May 30, 2022.

[44] Thorlabs. *Proposed Approach for Driving EO Phase Modulators.* https://www.thorlabs.com/images/TabImages/EO_Phase_Modulator_RF_Source_Option.pdf. Retrieved October 11, 2023.

[45] iXblue. *DRIVER DR-AN-20-HO 20 GHz Analog High Output Voltage Driver.* https://www.ixblue.com/wp-content/uploads/2022/02/DR-AN-20-HO.pdf. Retrieved October 11, 2023.

[46] N. Boulant, L. Quettier, G. Aubert, A. Amadon, J. Belorgey, C. Berriaud, C. Bonnelye, P. Bredy, E. Chazel, G. Dilasser, et al. *Commissioning of the Iseult CEA 11.7 T Whole-body MRI: Current Status, Gradient-magnet Interaction Tests and First Imaging Experience. Magnetic Resonance Materials in Physics, Biology and Medicine*, 36:175–189, 2023. doi:10.1007/s10334-023-01063-5.

[47] D. Le Bihan. *Exploring the Human Brain with Ultra-high Field MRI: Perspectives from the Iseult Project (4PL-1)*, 2023. MT-28 International Conference on Magnet Technology.

[48] S. Bates, S. O. Dumoulin, P. J. M. Folkers, E. Formisano, R. Goebel, A. Haghnejad, R. C. Helmich, D. Klomp, A. G. van der Kolk, Y. Li, et al. *A Vision of 14 T MR for Fundamental and Clinical Science.*

Magnetic Resonance Materials in Physics, Biology and Medicine, 36:211–225, 2023. doi:10.1007/s10334-023-01081-3.

[49] Radboud University. *Strongest MRI Scanner in the World Will be Built in the Netherlands*. https://www.ru.nl/en/research/research-news/strongest-mri-scanner-in-the-world-will-be-built-in-the-netherlands. Retrieved October 16, 2023.

[50] M. Parizh. *Short Courses MRI*, 2023. MT-28 International Conference on Magnet Technology.